

# Characterization of Microemulsions using Small Angle Scattering Techniques

Dissertation

zur Erlangung des akademischen Grades

doctor rerum naturalium (Dr. rer. nat.)

vorgelegt der

Mathematisch-Naturwissenschaftlich-Technischen Fakultät

(mathematisch-naturwissenschaftlicher Bereich)

der Martin-Luther-Universität Halle-Wittenberg

von Herrn Anuj Shukla

geb. am 10. März 1973 in Sitapur (Indien)

Gutachter:

1. Prof. Dr. Heinrich Graener
2. Prof. Dr. Reinhard Neubert
3. Dr. habil. Wolf-Dieter Hergeth

Halle (Saale), den 12.05.2003

**urn:nbn:de:gbv:3-000005108**

[<http://nbn-resolving.de/urn/resolver.pl?urn=nbn%3Ade%3Agbv%3A3-000005108>]

## Contents

<b>1.</b>	<b>Introduction</b>	<b>1</b>
1.1.	What is a microemulsion (ME)?	3
1.2.	What does a ME droplet look like?	4
1.3.	What is dynamic behavior of ME droplet?	5
1.4.	Design of MEs	5
1.5.	Applications of MEs	5
<b>2.</b>	<b>Small Angle Scattering Techniques</b>	<b>6</b>
2.1.	Comparison of Scattering Techniques and the Length Scales which they Probe	6
2.2.	Light Scattering	9
2.3.	Small Angle Neutron Scattering (SANS)	11
<b>3.</b>	<b>Theoretical Background</b>	<b>12</b>
3.1.	Static Light Scattering (SLS) from Interacting ME Droplets	12
3.2.	Dynamic Light Scattering (DLS)	17
	3.2.1. Monodisperse, Non-Interacting ME Droplets	18
	3.2.2. Polydisperse, Interacting ME Droplets	19
3.3.	Volume Fraction Dependence of Diffusion Coefficient	23
3.4.	SANS from Interacting ME Droplets	25
3.5.	The Form Factor	27
3.6.	The Structure Factor & Pair Distribution Function	29

---

3.7.	Interdroplet Interaction	31
<b>4.</b>	<b>Data Acquisition and Treatment</b>	<b>33</b>
4.1.	Data Acquisition: Static and Dynamic Light Scattering	33
4.2.	Data Treatment: SLS	35
4.3.	Data Treatment: DLS	36
4.4.	Data Acquisition and Treatment: SANS	41
<b>5.</b>	<b>Results And Discussion</b>	<b>46</b>
5.1.	Water – AOT – n- Alkanes MEs	46
5.1.1.	Layered Sphere Model	47
5.1.2.	Droplet Size and Polydispersity	51
5.1.2.1.	Refractive Index Increment	52
5.1.2.2.	DLS Results	53
5.1.2.3.	SLS Results	55
5.1.3.	Interdroplet Interactions and Droplet size	58
5.1.3.1.	SANS and CONTIN Results	58
5.1.3.2.	SLS Results	59
5.1.3.3.	DLS Results	61
5.1.4.	Shape Fluctuations of ME Droplets with Increasing Temperature	70
5.2.	Characterization of Pharmaceutical MEs	73
5.2.1.	Interdroplet Interaction and Droplet Size of O/W - MEs of Pharmaceutical Interest	73
5.2.1.1.	DLS Results	74

---

5.2.1.2. Effect of Proposed Interdroplet Interaction on the Stability of O/W - MEs	76
5.2.2. Behavior of Each Constituent Solubilized in MEs of Pharmaceutical Interest	79
5.2.2.1. O/W MEs of Pharmaceutical Interest	80
5.2.2.1.1. MEs with Different Ratios of Water/PG	81
5.2.2.1.2. MEs with Different Amounts of Oil	81
5.2.2.1.3. Effect of Drug Incorporation	82
5.2.2.1.4. MEs with Different Kinds of Oils	83
5.2.2.1.4.1. DLS Results	83
5.2.2.1.4.2. SANS Results	84
5.2.2.1.5. Effect of Temperature on ME Droplet	87
5.2.2.2. W/O – MEs of Pharmaceutical Interest	88
5.2.2.2.1. Different Ratios of Span <sup>®</sup> 20/ Tween <sup>®</sup> 80	89
5.2.2.2.2. MEs with Different Ratios of Water/DMSO	91
5.2.2.2.3. MEs with Different amounts of Surfactant	91
5.2.2.2.4. MEs with Different Kinds of Oils	92
5.2.2.2.5. Effect of Temperature on ME Droplets	93
5.3. Characterization of MEs having Local Anaesthetics as Dispersed Phase	94
5.3.1. Interdroplet Interaction	95
5.3.2. Different Amount of colloidal Phase	96
5.3.3. Effect of pH	96
<b>6. Summary and Conclusions / Zusammenfassung und Schlussfolgerungen</b>	<b>97</b>
6.1. Model ternary water/AOT/ <i>n</i> -alkanes MEs	97

---

6.2. MEs of pharmaceutical interest	99
<b>Suggestions for Future Studies</b>	<b>I</b>
<b>Appendix A</b>	<b>II</b>
<b>Appendix B</b>	<b>VII</b>
<b>Appendix C</b>	<b>IX</b>
<b>Appendix D</b>	<b>XII</b>
<b>List of References</b>	<b>XVI</b>

## List of Abbreviations

AOT	Sodium bis(2-ethylhexyl) sulfosuccinate (Aerosol <sup>®</sup> - OT)
AOT-MEs	Water/AOT/ <i>n</i> -alkanes Systems
DLS	Dynamic Light Scattering
DMSO	Dimethyl sulfoxide
EMLA	Eutectic Mixture of Local Anaesthetics
EO	Ethylene Oxide
Eutanol	2-Octyl-1-dodecanol
HLB	Hydrophilic-Lipophilic-Balance
HNC	Hypernetted-Chain
HS	Hard Sphere
IPM	Isopropyl myristate
IPP	Isopropyl palmitate
ME	Microemulsion
NMR	Nuclear Magnetic Resonance
OA	Oleic acid
O/W	Oil-in-Water
PO	Propylene Oxide
Poloxamer 331	Polyoxyethylene – Polyoxypropylene – Block co-polymer
PG	Propylene Glycol
PY	Percus-Yevick
SANS	Small Angle Neutron Scattering
SAS	Small Angle Scattering
SLD	Scattering Length Density
SLS	Static Light Scattering
Span <sup>®</sup> 20	Sorbitan monolaurate
Tagat <sup>®</sup> O2	Polyoxyethylene glycerol monooleate
Tween <sup>®</sup> 80	Polyoxyethylene sorbitan mono-oleate
W/O	Water-in- Oil

# 1 Introduction

The ever-increasing demands on the performance of pharmaceutical formulations with respect to, e.g., greater dosage levels, greater bioavailability, storage stability, fewer side effects and controlled release constitute the main motivation for drug delivery research. Surfactants play a key role in many of the novel drug delivery systems developed, and wide range of surfactant-containing systems, including emulsions, liposomes, liquid crystalline phases and microemulsions (MEs), are being extensively investigated in relation to drug delivery.<sup>1,2</sup> In the last few decades advances in physics and pharmacy have gone hand in hand in this research. The most fundamental discoveries in physics have rapidly been exploited by the medical community to devise new techniques for characterizing and enhancing the quality of drug delivery systems. And physicists are increasingly listening to the demands of the medical profession when defining the direction of new research. The best known example of the link between physics and medicine is the use of scattering techniques to diagnose, treat disease and characterize the physico-chemical properties of drug and drug delivery systems. This thesis and associated publications<sup>3,4,5,6,7,8</sup> are attempt to study the drug delivery systems (MEs) with two basic objectives: (I) to determine the effect of each constituent solubilize in ME on droplet size and stability, (II) to examine the physical basis of the interactions between the ME droplets.

MEs are systems consisting of water, oil and amphiphile(s) that constitute a single optically isotropic and thermodynamically stable liquid solution. Since the day when scattering properties of MEs were first investigated by Hoar and Schulman,<sup>9</sup> scientists have been fascinated with the physical and chemical properties of these systems. Usually, these systems are studied with scattering techniques (Light, Neutron, X-ray), nuclear magnetic resonance (NMR) and electrokinetic chromatography,<sup>10,11</sup> for the understanding their physico-chemical properties. In this thesis, we have explored in some depth the use of scattering techniques, static light scattering (SLS), dynamic light scattering (DLS) and small-angle neutron scattering (SANS) for the investigation of MEs. These scattering techniques are briefly introduced in Chapter 2. Although all these techniques are well-founded, some fundamental difficulties principally arise because in many MEs both the droplet size and the extent of interaction between the droplets vary simultaneously as a function of volume fraction and consequently the usual technique of extrapolating to zero concentration, and hence assuming ideality, can not be used. The combination of SLS, DLS and SANS is used for this type of problem, in that SLS and SANS can provide time-average structural information and DLS dynamic information about the motion of the droplets in interacting systems. The theory necessary for the evaluation of the obtained results are provided in Chapter 3. The description of apparatus used for data acquisition are presented in Chapter 4.

An efficient use of MEs in many scientific and industrial applications is directly related to the understanding of their microstructure. This thesis extends the knowledge of the microstructure

of model anionic surfactant system, water/sodium bis(2-ethylhexyl) sulfosuccinate (AOT)/*n*-alkane (AOT-ME) as well as ME systems of pharmaceutical interests. In the first part of the Chapter 5, diffusion dynamics and interdroplet interaction of AOT-MEs in the large concentration range are studied for the first time, along with the droplet size growth, shape and size fluctuation of ME droplets using contrast variation experiments. Chain length of the *n*-alkane has been varied in order to show the dependence of above mentioned features of systems on the chain length. Several authors<sup>12,13</sup> have reported the use of water/AOT/*n*-alkane system in combination with nonionic surfactant sorbitan monooleate (Span<sup>®</sup> 20, Arlacel 20) as topical drug delivery vehicles, free of the irritancy effects normally associated with medium chain length alcohols. Although water/AOT/*n*-alkane systems have been widely studied as model systems, these systems consist normal alkanes as oils, which are not edible, making them of less practical use in delivery systems. In the second part of the Chapter 5, W/O and O/W - MEs comprising pharmaceutical acceptable substances are characterized. These pharmaceutical MEs are formulated without using cosurfactant (medium chain alcohols). The inclusion of short or medium chain alcohols as cosurfactants limits the potential use of the ME due to their high toxic and irritant properties.<sup>14,15</sup> Since it is known that a single surfactant alone is generally not optimum, mixtures of pharmaceutical acceptable surfactants such as Tween (polyoxyethylene sorbitol) and Span (Sorbitol ester) or Tween (polyoxyethylene sorbitol) and Block co-polymers (Poloxamers) are used to get an improvement in ME properties similar to those obtained by the addition of a cosurfactant. The larger head group of Tween pushes it out into the aqueous phase more, allowing the surfactant molecules to pack more tightly and tail to interact strongly. With block copolymers of ethylene oxide-propylene oxide type, such as the Poloxamers, the hydrated polyoxyethylene chains extend into the continuous phase to provide steric stabilization and the hydrophobic propylene oxide portion is anchored onto the droplet surface to form a strong protecting layer against coalescence. MEs consisting the pharmaceutical acceptable oils such as isopropyl palmitate (IPP), isopropyl myristate (IPM), eutanol, oleic acid and triglycerides (Miglyol) are characterized. Microemulsions using DMSO instead of water as hydrophilic dispersed phase in W/O MEs are also characterized because DMSO can penetrate the skin quickly and deeply without damaging it. This property would enable DMSO to act as a new drug delivery system that would lower the risk of infection occurring whenever skin is penetrated. In the third part of the Chapter 5, colloidal vehicle systems (MEs) comprising biologically active substances such as local anaesthetics as dispersed, colloidal phase are investigated. In this thesis, first attempt is made to compile all the factors contributing to the stability of above mentioned MEs of pharmaceutical interest. The treatment for stability accounts for the calculation of droplet size and estimation of interdroplet interaction. A droplet size distribution in pharmaceutical ME is important from both stability and biopharmaceutical consideration. The larger droplet size, the greater the tendency to coalesce and further increase the droplet size. Thus, fine particles generally promote better stability. From the biological point of view, fine emulsification enhances gastrointestinal absorption and this is also desirable with oral formulations of nutrient oils or with drugs dissolved in them. The Chapter 6 deals with our findings and conclusions. Further we briefly discuss about an outlook on the future work. In this introduction, we review a few basic concepts regarding these systems.

## 1.1 What is a ME?

Amphiphilic molecules are composed of two different parts: hydrophobic tail and hydrophilic head. An example of an amphiphilic molecule is shown in Figure 1.1C. The tail is composed of one or more hydrocarbon chains, usually with 6 to 20 carbon atoms, the head is composed of chemical groups of high affinity to water.<sup>16</sup> Such a composition of amphiphilic molecules results in many amazing properties of systems containing these molecules. Adding an appropriate amount of amphiphile to a mixture of oil and water, two liquids which are immiscible under normal conditions, cause complete mixing of these liquids. The amount of amphiphile necessary to cause mixing depends on the strength of amphiphile. The longer the hydrocarbon chain the stronger the amphiphile is. The strength of amphiphile depends in similar way on the number of hydrophilic groups in the amphiphilic molecule. Complete mixing is enabled by lowering the oil-water surface tension by amphiphile. That is why the amphiphilic molecules are also called surfactants: surface active agents. The surfactant assembles at the interface, forming a monolayer, in such a way that the hydrophilic part of the amphiphile is located in water and hydrophobic part in oil.

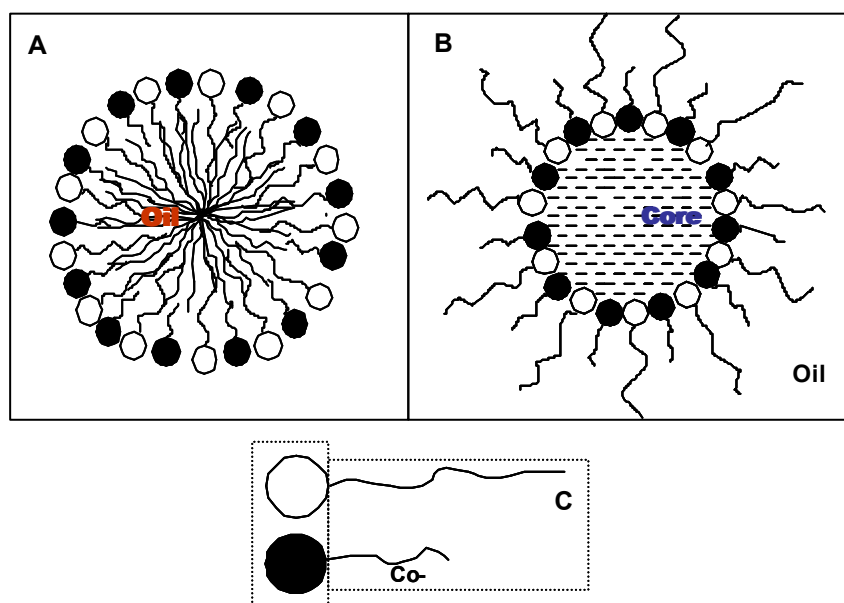


**Figure 1.1** Diagrammatic representation of (A) O/W - ME droplet (B) W/O - ME droplet (C) surfactant and co-surfactant.

The surfactant monolayer separates coherent regions of oil and water and reduces interfacial tension between two regions. Usually the monolayer width is small compared to the size of oil and water regions, unless the concentration of surfactant is very high. In such a situation the formation of water and oil droplets dispersed in the surfactant solution is possible. Surfactants

dissolved in water can form micelles of different shape: spherical or cylindrical. They can also assemble into spherical bilayers (vesicles) grouping the hydrophobic part of the surfactant inside the bilayer. The aggregate of surfactants containing a small amount of bound water usually called reverse micelle. The micellar or reverse micellar core constitutes nonpolar or polar micro-environment which can accommodate oil or water. The solubilize oil or water molecules can either be located among (the hydrocarbon tails-oil solubilize or the hydrophilic head group-water solubilize) the surfactant molecules or form, in addition, a core inside the aggregate. The first case is usually referred to as solubilization and the second as microemulsification. Term “Swollen micelles” corresponds to first case (containing only solubilized oil or water associated with the surfactant molecules) where as term “MEs” correspond to second case (containing solubilized oil or water bound to surfactant molecules as well as containing "free" oil or water in the interior of the droplet). Many investigators have perceived a difference between “MEs” and “swollen micelles”. In this study the term “ME” will be used to describe both systems. This is in agreement with the definition proposed by Danielson and Lindman,<sup>17</sup> who considered a ME to be “a system of water with or without electrolyte, oil and surfactants which are single isotropic and thermodynamically stable solutions.”

## 1.2 What does a ME droplet look like?

The solubilization of one phase into another in a ME system is affected by a balance of attractive and repulsive forces. As MEs are thermodynamically stable, the droplets will not coalesce and precipitate over time. A condensed film with very strong lateral forces and good elasticity will provide an excellent barrier to collision coalescence. With the exception of double alkyl chain surfactants and a few nonionic surfactants, it is generally not possible to form condensed films with the use of a single surfactant. Thus most MEs are made from the mixture of a surfactant and a cosurfactant. This cosurfactant is usually a short chain alcohol, ranging from two carbons (ethanol) to four carbon atoms (butanol), though alcohols up to decanol have been studied by some investigators. The simplest representation of the structure of MEs in the droplet form in which ME droplets are surrounded by the interfacial film consisting of both surfactant and cosurfactant molecules, as illustrated in Figure 1.1. The orientation of the amphiphiles at the interface, differs in O/W and W/O - MEs. As shown in Figure 1.1, the hydrophobic portions of these molecules will reside in the dispersed oil droplets of O/W systems, with the hydrophilic groups protruding in the continuous phase, while the opposite situation will be true of W/O - MEs.

### 1.3 What is dynamic behavior of ME droplet?

Droplets of ME are affected by thermal motion of the solution and will collide with each other. Collisions between droplets occur, while most will repel, some will coalesce and then spontaneously break apart again. Such encounters result in short lived clusters that may exchange solubilized material before dissociating into separate droplet causing collective and self diffusion of droplets. Since some fractions of ME droplet collisions result in coalescence, yet the mean droplet size in the ME remains constant over time, there must be a driving force to break up these aggregates again. Positive interfacial tension is the driving force for decreasing interfacial area of a given droplet, so there must be some "negative" interfacial tension present to force an increase in interfacial area and the resulting break up of ME droplets that are too large. At the optimum droplet size, the forces are balanced and the interfacial tension must approach zero. Therefore, ME droplet can be considered as a dynamic entity, a tiny droplet surrounded by a monolayer or an aggregate of surfactant or mixture of two surfactants, sometimes combining with its neighbors, and subsequently breaking apart, sometimes exposing the water phase to the oil phase.

### 1.4 Design of MEs

There have been several studies of the effect of surfactant molecular structure on ME formation. Israelachvili<sup>18</sup> described a *surfactant packing parameter* ( $v_s/a_sL$ , where  $v_s$  is the surfactant molecular volume,  $L$  is the length of the hydrophobic part of surfactant, and  $a_s$  is the cross-sectional area occupied by the hydrophilic group at the interface), which predicts the shape of the aggregates formed spontaneously. O/W MEs will be formed when  $v_s/a_sL < 1$ , W/O MEs will be formed when  $v_s/a_sL > 1$  and lamellar phases when  $v_s/a_sL \sim 1$ .

### 1.5 Applications of MEs

The ability of MEs to confer macroscopic homogeneity on immiscible substances, high thermodynamic stability, and solubilize materials of differing polarity has led to their wide use in industry: pharmaceutical, textile cleaning, food, cosmetic, and oil.<sup>19,20,21</sup> In addition to their traditional roles in aforesaid industries, MEs offer several potential advantages as drug delivery systems.<sup>22</sup> Poorly water soluble drugs in pharmaceutical dosage form a challenge, due to the severe restriction on the choice of solvents suitable for oral, topical or parental use. Finely dispersed oil droplets of O/W - MEs offer a potential solvent for such drugs. W/O - MEs are suitable to facilitate the transport of hydrophilic compounds through the penetration barrier, stratum corneum. MEs also seem to be reasonable means to remove soil containing high amounts of mineral oil from surfaces because of their extremely low interfacial tension and their high solubilization power.<sup>23</sup> MEs also used for microreactor in biotechnology.<sup>24</sup>

## 2 Small Angle Scattering (SAS) Techniques

*Small angle scattering (SAS)* is the collective name given to the techniques of *small angle neutron (SANS)*, *X-ray (SAXS)* and *light (LS, includes both Static SLS and Dynamic DLS)* scattering. In each of these techniques radiation is elastically scattered by a sample and the resulting scattering pattern is analyzed to provide information about the size, shape and orientation of some components of the sample (see Figure 2.1).

The type of sample that can be studied by SAS, the sample environment that can be applied, the actual length scales that can be probed and the information that can ultimately be obtained, all depend on the nature of the radiation employed. For example, LS can not be used to study optically opaque samples and SAXS can not (easily) be employed to study thick samples or samples requiring complex containers, while SANS (and SAXS) probe different length scales to LS. Thus to a large extent these techniques are complementary. However, they also share several similarities. Perhaps the most important of these is the fact that, with minor adjustments to account for the different types of radiation, the same basic equations and "laws" (for example, those due to Guinier, Zimm, Kratky and Porod) can be used to analyze data from any of the three techniques. Colloidal systems include materials of very different nature- generally speaking, colloidal systems consist of two or more components, and one can identify individual particles dispersed in a homogeneous medium, called "solvent" the particle and the solvent can be complex or formed of different components, like for example in the case of MEs where three to five different molecules can be present. The physics of these systems is very diverse but, in all cases, a detailed description of the structure is necessary. SAS technique has been proven to be a unique and powerful tool for elucidating the structure, interaction, and phase transitions in micellar and ME systems.<sup>25,26</sup>

### 2.1 Comparison of Scattering Techniques and the Length Scales which they Probe

Schematic representation of a scattering experiment is shown in Figure 2.1. A basic quantity in a scattering experiment (see Figure 2.1) is the scattering vector  $\vec{q} = \vec{q}_s - \vec{q}_0$ , which represents the difference between the wave vectors of the scattered and incident radiations. In the scattering experiment from an isotropic medium containing heavy particles, one measures predominantly the elastic and quasielastic scattering for which  $|\vec{q}_s| = |\vec{q}_0| = 2\pi n / \lambda_0$ . Consequently, the modulus of  $\vec{q}$ , related to the scattering angle  $\theta$ , index of the refraction  $n$

and the vacuum wavelength  $\lambda_0$  of the incident light is given by  $|\vec{q}| = \left( \frac{4\pi n}{\lambda_0} \right) \sin \frac{\theta}{2}$ . For light,  $n=1.33$  in water, but for X-rays and neutrons  $n$  is very close to unity.

LS using the photon correlation spectroscopy technique has been used to study the hydrodynamic properties of association colloids. This technique relies on the measurement of the diffusion (apparent, collective and self diffusion) coefficients. One can extract the information about aggregate size, inter-particle interaction<sup>27</sup>.

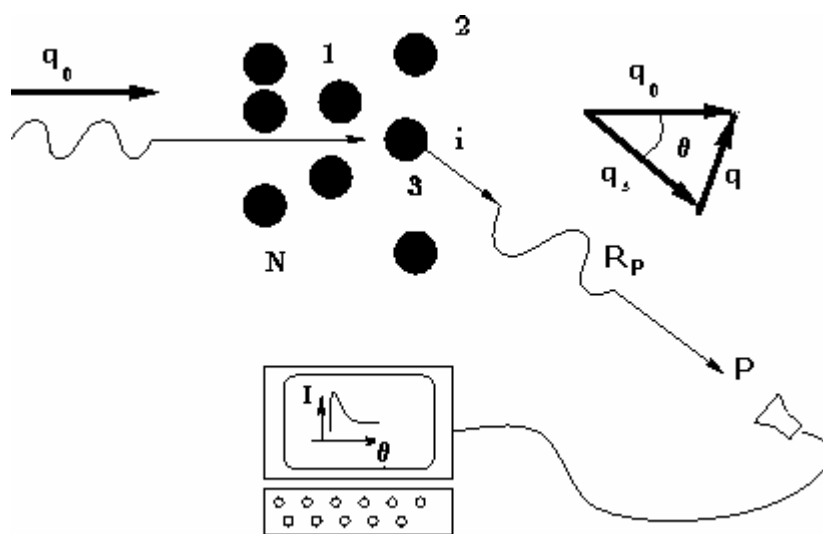


**Figure 2.1** Schematic representation of a scattering experiment. The incident beam propagates along the wave vector  $q_0$  and scattered beam along the wave vector  $q_s$ . The scattering angle  $\theta$  is the angle between  $q_0$  and  $q_s$ . The distance  $R_p$  is taken to be much larger than the linear size of the scattering volume.

Neutron and X-ray scattering are a valuable research tools as it allows to study the microscopic structure of colloidal, polymer and surfactant systems to be studied. It provides information on the shape and size of the small-scale structures often found within such systems.<sup>26</sup> Neutron beam can be produced to cover a range of wavelengths; 0.01 - 3 nm. This range is comparable to that which may be obtained with X-rays (for example, the Cu- $K_{\alpha}$  line at 0.15 nm) but is orders of magnitude smaller than that of visible light (400 - 700 nm). The most fundamental difference between neutron and electromagnetic radiation is the mechanism by which the incident radiation interacts with the matter. Light and X-rays are both scattered by the electrons surrounding atomic nuclei, but neutrons are scattered by the nucleus itself. This single fact has several important consequences. In the case of electromagnetic radiation, energy  $E$ , and wavelength  $\lambda$ , are related through Planck's equation,  $E = hc/\lambda$ , but because the neutron has a finite mass ( $m = 1.674 \times 10^{-27}$  kg), it is necessary to consider its kinetic energy given by  $E = \frac{h^2}{2m\lambda^2} = \frac{mv^2}{2}$ . Thus, a neutron with a wavelength of 0.15 nm has energy of

$5.83 \times 10^{-21}$  J or, in more practical units, 36.4 meV. By contrast, the energy of a 0.15 nm X-ray photon is  $\sim 8.2$  keV, more than 200,000 times greater than the energy of the neutron. Thus neutrons have particular advantage over X-rays in the study of sensitive samples, such as biological material, since X-ray causes serious molecular degradation due to radiative heating.

The usefulness of SAS to colloid and polymer science becomes clear when one considers the length scales involved; bond lengths are typically around 0.1 nm, the radius of gyration of a polymer in solution is usually 1 - 10 nm, a microemulsion droplets may be 10 - 100 nm in diameter, while latex particles and emulsion droplets are often 100 - 1000 nm in diameter. In order to get information about the structure and size distribution, the wavelength of the radiation  $\lambda$ , used in the scattering experiment should match the size range of the interest. A fundamental theorem in the theory of the scattering wave by an extended object relates the  $r$ -space density distribution of the scattering object to the  $q$ -space scattered intensity distribution in terms of a Fourier transform. It follows from this theorem that the characteristic size in the  $r$ -space,  $R$  is reciprocally related to the characteristic width of the intensity distribution in  $q$ -space. Therefore, to characterize aggregates of the size  $R$ , one needs to do a scattering experiment in which  $\vec{q}$  spans a range about an order of magnitude on each side of the value

$q_0 = \frac{2\mathbf{p}}{R}$ . The Figure 2.2 below shows a comparison of scattering techniques and the length

scales  $R \sim \frac{2\mathbf{p}}{q}$  which they probe. DLS has a greater range than other scattering techniques

because it is concerned with the distance ( $2\mathbf{p}/q$ ) that a particle diffuses in a correlation time.

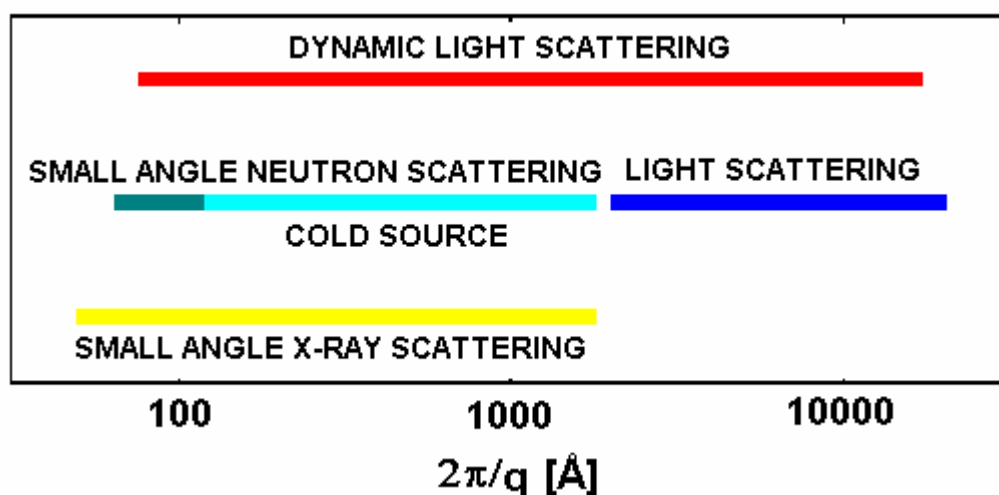


**Figure 2.2** Length scales measured by different scattering techniques.

Detailed review of LS and SANS methods has been presented in the following sections.

## 2.2 Light Scattering

The interaction of the light with matter can be used to obtain important information about structure and dynamics of matter. Study of this interaction is possible by light scattering experiments.

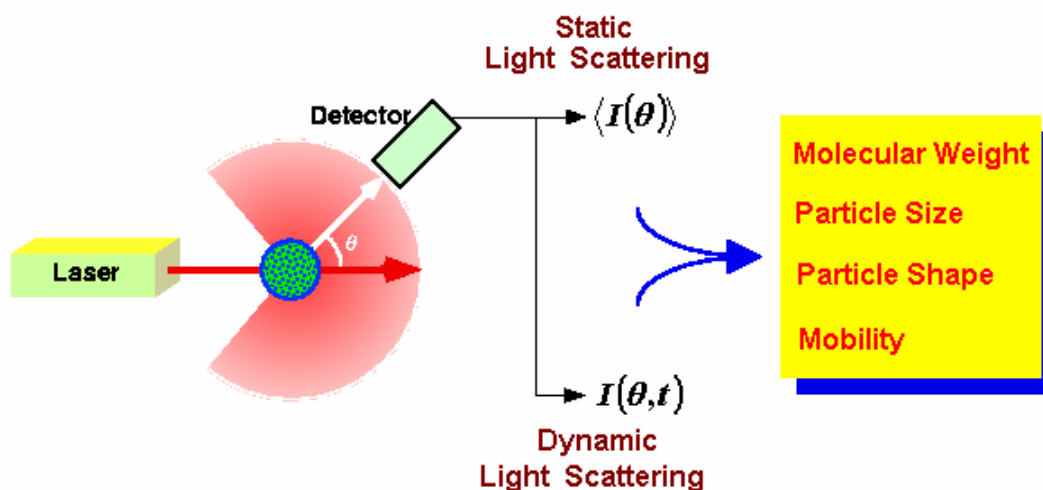


Figure 2.3 Typical light scattering experiment.

There are two ways to glean information from a light scattering experiment. The first method, called **Dynamic Light Scattering (DLS)**, is to monitor fluctuations in scattered light  $I(t)$  as a function of time. The second method, called **Static Light Scattering (SLS)**, is to observe interparticle interference patterns of scattered light by measuring the intensity  $I(\mathbf{q})$  as a function of angle. A typical *Light Scattering* experiment is shown in the above picture (Figure 2.3). When light is shined on matter it will scatter and the scattered light gives us information about molecular structure and motion in the material. In general, interaction of electromagnetic radiation with a molecule leads either to absorption, forms the basis of the *spectroscopy* or *scattering* the radiation. Visible light is extensively used as a nonperturbative direct probe of the state and the dynamics of small particles in solution. The light traversing a medium is scattered into directions other than that of the reflected and refracted beam due to spatial inhomogeneity of the dielectric constant  $\epsilon$ . For microemulsions the most relevant inhomogeneities are those produced by the ME droplets with respect to solvent. The weaker scattering due to spontaneous thermal fluctuations of  $\epsilon$  in the solvent can usually be neglected or properly subtracted. In this section, I will review briefly the physical aspects of light scattering experiments.

The physical origin of light scattering can be simply understood by considering the particle as an elementary dipole which is forced to oscillate at the frequency of the incident field and, in turn, radiates. The scattering process is taken to be linear, that is the scattered field  $\mathbf{E}_s$  is

proportional to the incident field  $E_0$ , and only single-scattering events are considered (no multiple scattering). Almost all of the scattered light has the same wavelength as the incident radiation and comes from *elastic* (or *Rayleigh*) scattering. The electric field of the wave scattered by a particle much smaller than the wavelength of the light, referring to the geometry of Figure 2.1, is<sup>28</sup>

$$(2.1) \quad \vec{E}_s(\vec{R}_p, t) = \frac{\vec{q}_s \times (\vec{q}_s \times \vec{E}_0)}{4\pi \epsilon \vec{R}_p} \mathbf{a} \exp[i(\mathbf{w}_0 t - \vec{q}_s \cdot \vec{R}_p)] \exp[i\vec{q} \cdot \vec{r}]$$

In above expressions,  $\epsilon$  is the dielectric constant of the medium in which the particle is suspended and  $\mathbf{a}$  is the polarizability of the particle. In general, if there is more than one particle in the scattering volume, the scattered field at the detector will be given by the sum of all the contributions from the N particles

$$(2.2) \quad E_s(\vec{R}_p, t) = \exp[i(\mathbf{w}_0 t - \vec{q}_s \cdot \vec{R}_p)] \sum_{j=1}^N f_j \exp[i\vec{q} \cdot \vec{r}_j]$$

where  $\vec{r}_j$  specifies the position of the centre of mass of the  $j^{\text{th}}$  particle and  $f_j$  is the scattering amplitude of the  $j^{\text{th}}$  particle.

The radiated or scattered field of Eq. (2.2) at a given time is the sum (superposition) of the electric fields radiated from all of the charges in the illuminated scattering volume and consequently depends on the exact positions of the charges. The molecules in the illuminated region are perpetually translating, rotating and vibrating by the virtue of thermal motion (Brownian motion). Because of this motion the position of the charges are constantly changing so that the total scattered electric field at the detector will fluctuate in time. This fluctuation gives rise to a Doppler effect and so the scattered light possesses a range of frequencies shifted very slightly from the frequency of the incident light. This phenomenon is called DLS. We usually deal with very small broadenings  $\Delta\mathbf{w}$  with respect to the frequency of the incident light  $\mathbf{w}_0$ , so in literature, these experiments often referred as *quasi-elastic scattering (QELS)* instead of DLS too. Such small widths are generally inaccessible to optical spectrometers because of their limited resolution. They are measured by means of optical beating on the light detector, the so-called intensity correlation technique. The intrinsic differential nature of this technique allows measurements of spectral width even smaller than the laser source itself.<sup>27</sup> These frequency shifts (field time correlation function) yield information relating to the movement (i.e. the dynamics) of the scatterers. The time average of scattered field bears information on the static properties of the scattering medium: size, shape of the scatterers and thermodynamic quantities.

## 2.3 Small Angle Neutron Scattering (SANS)

SANS has been developed rapidly as a useful probe of structure and dynamics of colloidal systems. The particular utility of SANS in structural research arises from the opposite signs and large difference between the scattering lengths of  $^1\text{H}$  and  $^2\text{H}$ , whereas electrons and X-rays are scattered from  $^1\text{H}$  and  $^2\text{H}$  with similar intensities. The contrast of a molecule (with respect to the scattering length of its environment) observed by neutrons can be varied by altering the  $^2\text{H}_2\text{O}:\text{}^1\text{H}_2\text{O}$  ratio of the sample background. This means that at certain measurable deuterium: hydrogen ratios, components of a complex system can be made invisible.

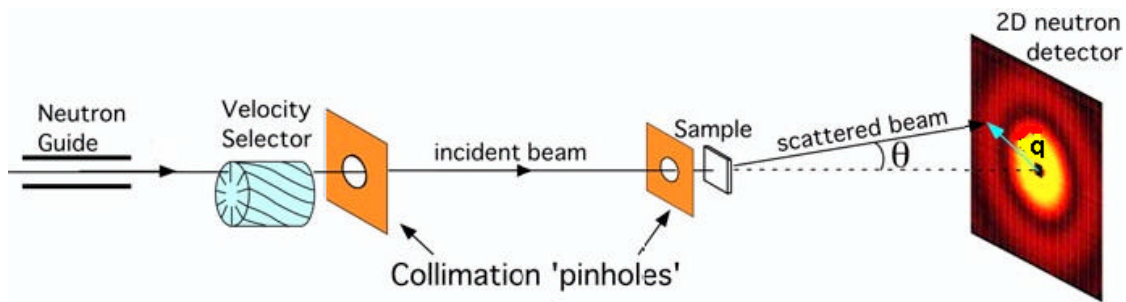


**Figure 2.4** Typical Small Angle neutron scattering experiment.

A typical SANS experiment and a basic quantity in a scattering experiment  $\vec{q}$  is shown in the above picture (Figure 2.4). In any SANS experiment, a collimated beam of neutrons of intensity  $I_0$ , is incident at a sample, illuminating a small volume,  $V (= A t_s$ , where  $A$  is the cross-sectional area of the beam and  $t_s$  is the pathlength of the sample) containing  $N$  particles in solution. Some of the incident radiation is transmitted by the sample, some is absorbed and some is scattered. A detector, or detector element, of dimensions  $dx \times dy$  positioned at some distance,  $L_{sd}$ , and scattering angle,  $\theta$ , from the sample then records the intensity of neutrons scattered into a solid angle element,  $d\Omega (= dx dy / L_{sd}^2)$ . This scattered intensity  $I(\mathbf{l}, \mathbf{q})$ , can be expressed in general terms in the following way

$$(2.3) \quad I(\mathbf{l}, \mathbf{q}) = I_0(\mathbf{l}) d\Omega \mathbf{h}(\mathbf{l}) T_s \frac{d\mathbf{s}(\vec{q})}{d\Omega}$$

where  $\mathbf{h}$  is the detector efficiency (sometimes called the response),  $T_s$  is the sample transmission and  $d\mathbf{s}/d\mathbf{W}$  is a function known as the (*microscopic*) *differential cross-section*. Although this function is specific to SANS, analogous functions exist for light [Eq. (3.3)] and X-rays. The first three terms of Eq. (2.3) are clearly instrument-specific while the last two terms are sample-dependent. The objective of a SANS experiment is to determine the differential cross-section, since it contains all the information on the shape, size and interactions of the scattering bodies (assemblies of scattering centers) in the sample.

### 3 Theoretical Background

In this chapter, the theoretical background of static and dynamic light scattering as well as small angle neutron scattering is presented. The discussion of light scattering begins with the scattering theory of colloidal particles in solution. On the basis of this basic theory, the equations for static and dynamic light scattering, necessary for the evaluation of the results of the measurements are deduced.

The knowledge necessary for the evaluation and classification of the results over pair distribution function and to the structure factor and the form factor are made available. During the evaluation of the experimental neutron scattering curves different particle form factors and structure factors were tested<sup>29</sup>. It was shown that the spherical form factor and Percus and Yevick<sup>30</sup> structure factor describe the scattering curves best. A special emphasis is put on the discussion of the used form and structure factors.

#### 3.1 SLS from Interacting ME Droplets

In SLS experiments the time-average (or 'total') intensity of the scattered light is measured, and for MEs, it arises from concentration fluctuation of the droplets in ME. The excess scattering intensity  $I_{excess}$  of the droplets at the scattering angle  $\mathbf{q}$  at distance  $R_p$ , over that of the continuous phase can be written as<sup>28,31</sup>

$$(3.1) \quad \begin{aligned} I_{excess} &= I_{solution} - I_{solvent} \\ &= I_0 \frac{\mathbf{P}^2 \sin^2 \mathbf{g}}{I_0^4 R_p^2} \left\langle |\mathbf{de}(\vec{q}, t)|^2 \right\rangle_{excess} \end{aligned}$$

where  $I_0$  is the incident intensity,  $\left\langle |\mathbf{de}(\vec{q}, t)|^2 \right\rangle_{excess}$  is the mean square dielectric fluctuation and  $\mathbf{g}$  is the angle between the scattering direction and the incident electric field. The term "excess" is used to describe the scattering resulting from the droplets in a ME alone. The inverse fourth power dependence on  $\lambda_0$  [see Eq. (3.1)] was firstly predicted by Lord Rayleigh on the basis of simple dimensional arguments.<sup>32</sup> It accounts for the blue color of the sky, red sunset, green flash and twilight wedge.

The mean square dielectric fluctuation  $\left\langle |\mathbf{de}(\vec{q}, t)|^2 \right\rangle_{excess}$  is related to the mean square fluctuation in the concentration as<sup>33</sup>

$$(3.2) \quad \left\langle \left| \mathbf{d}\mathbf{e}(\bar{q}, t) \right|^2 \right\rangle_{excess} = \left( 2n \frac{\partial n}{\partial \mathbf{f}} \right)^2 \left\langle \left| \mathbf{d}\mathbf{f}(\bar{q}, t) \right|^2 \right\rangle$$

where  $\mathbf{f}$  is volume fraction of the droplets in a ME.

By means of Eqs. (3.1) and (3.2), the excess scattered intensity of the droplets over that of the continuous phase (solvent) becomes

$$(3.3) \quad I_{excess} = I_0 \frac{4\mathbf{p}^2 n^2 \sin^2 \mathbf{g}}{\mathbf{I}_0^4 R_p^2} \left( \frac{\partial n}{\partial \mathbf{f}} \right)^2 \left\langle \left| \mathbf{d}\mathbf{f}(\bar{q}, t) \right|^2 \right\rangle$$

Notice that the scattered intensity depends strongly on the refractive-index increment  $\frac{\partial n}{\partial \mathbf{f}}$ . MEs with the same refractive index as the solvent become invisible by light scattering.

The mean square concentration fluctuation  $\left\langle \left| \mathbf{d}\mathbf{f}(\bar{q}, t) \right|^2 \right\rangle_{excess}$  is usefully expressed as<sup>33</sup>

$$(3.4) \quad \left\langle \left| \mathbf{d}\mathbf{f}(\bar{q}, t) \right|^2 \right\rangle = \left\langle \left| \mathbf{d}\mathbf{f}(0, 0) \right|^2 \right\rangle S(q)$$

where  $\left\langle \left| \mathbf{d}\mathbf{f}(0, 0) \right|^2 \right\rangle$  is a purely thermodynamic quantity, and  $S(\bar{q})$  is the structure factor. ME droplets are always much smaller than  $\lambda$  ( $\sim 532$  nm) so that their scattering intensities are independent scattering vector. For such case  $S(\bar{q}) = 1$  and  $\left\langle \left| \mathbf{d}\mathbf{f}(0, 0) \right|^2 \right\rangle$  can be written as<sup>34</sup>

$$(3.5) \quad \left\langle \left| \mathbf{d}\mathbf{f}(0, 0) \right|^2 \right\rangle = \frac{k_B T \mathbf{f}}{v_d \left( \frac{\partial \Pi}{\partial \mathbf{f}} \right)}$$

where  $v_d = 4\mathbf{p}R^3/3$  is the volume of a scatterer (droplet in case of ME) having a radius  $R$  and  $\Pi$  is the osmotic pressure.

Substitution of Eqs.(3.4), (3.5) into the Eq. (3.3) then excess scattered intensity becomes

$$(3.6) \quad I_{excess} = I_0 \frac{4\mathbf{p}^2 n^2 \sin^2 \mathbf{g}}{\mathbf{I}_0^4 R_p^2} \left( \frac{\partial n}{\partial \mathbf{f}} \right)^2 \mathbf{f} \frac{k_B T}{v_d} \left( \frac{\partial \mathbf{f}}{\partial \Pi} \right)$$

Average scattered intensity  $I$  measurements are done at a fixed angles, and are relative. We obtain in this way a quantity  $I$  proportional to the product of  $I_{excess}$  by the solid angle of the detection  $d\mathbf{W}$ .  $d\mathbf{W}$  varies with the refractive index of the sample as  $d\mathbf{W} \propto \frac{1}{n^2}$ .<sup>35</sup> Therefore,

$$(3.7) \quad I = \frac{I_{excess}}{d\mathbf{W}} = G \left( \frac{\partial n}{\partial \mathbf{f}} \right)^2 \mathbf{f} \frac{k_B T}{v_d} \left( \frac{\partial \mathbf{f}}{\partial \Pi} \right)$$

with

$$G = I_0 \frac{4\mathbf{p}^2 \sin^2 \mathbf{g}}{\mathbf{I}_0^4 R_p^2}$$

where  $G$  is a constant, independent of the sample.

In 1976 Vrij and co-workers applied liquid state theories to droplet-phase MEs.<sup>36</sup> For the osmotic pressure  $\Pi$  they used semiempirical expression

$$(3.8) \quad \Pi = \frac{k_B T}{v_d} \left( \mathbf{f} + \frac{B_2}{v_d} \mathbf{f}^2 + \dots \right)$$

where  $B_2$  is the second virial coefficient.

Using Eq. (3.7) and Eq. (3.8), one can write

$$(3.9) \quad \frac{\mathbf{f}}{I} \approx \frac{3}{4\mathbf{p}R^3 G} \left( \frac{\partial n}{\partial \mathbf{f}} \right)^{-2} (1 + K_I \mathbf{f} + \dots)$$

where  $K_I = 2B_2/v_d$  is the perturbation due to thermodynamic effect. This  $K_I$  is related to the interaction potential  $U(r)$  as<sup>37,38,33</sup>

$$(3.10) \quad K_I = K_I^{HS} + \int_0^\infty dx 24(1+x)^2 [1-g(x)]$$

*with*

$$K_I^{HS} = 8$$

where  $x = r - 2R/2R$ , and  $g(x)$  pair distribution function.

Assuming that the droplet size does not vary significantly over the concentration range and systems under study are ideal mixture ( $\partial n/\partial \phi$  is constant), one can obtain simplified expression by normalizing  $\mathbf{f}I = I$  as limit  $\phi \rightarrow 0$

$$(3.11) \quad \frac{\mathbf{f}}{I} \approx (1 + K_I \mathbf{f} + \dots)$$

Eq. (3.11) is used to analyze the relative intensity of samples at different concentrations, provided  $R$  remains constant.

The relationship between the mean square dielectric fluctuation and the mean square optical excess polarizability per scatterer (droplet) per unit volume  $\alpha_{\text{excess}}$  is

$$(3.12) \quad \left\langle |\mathbf{d}\mathbf{e}(q, t)|^2 \right\rangle_{\text{excess}} = N \frac{\langle \mathbf{a}^2 \rangle_{\text{excess}}}{\epsilon_0^2} \quad \text{with} \quad N = \frac{\mathbf{f}}{\langle v_d \rangle}$$

where  $\epsilon_0$  is the dielectric constant for free space.<sup>33</sup>

From Eqs. (3.1), (3.7) and (3.10), average scattered intensity  $I$  can be written as the product of the average differential scattering cross-section  $\left( \propto \frac{\langle \mathbf{a}^2 \rangle}{I^4} \right)$  of the ME droplets and the number density  $\frac{\mathbf{f}}{\langle v_d \rangle}$

$$(3.13) \quad \langle I \rangle \propto \frac{\langle \mathbf{a}^2 \rangle \mathbf{f}}{I^4 \langle v_d \rangle}$$

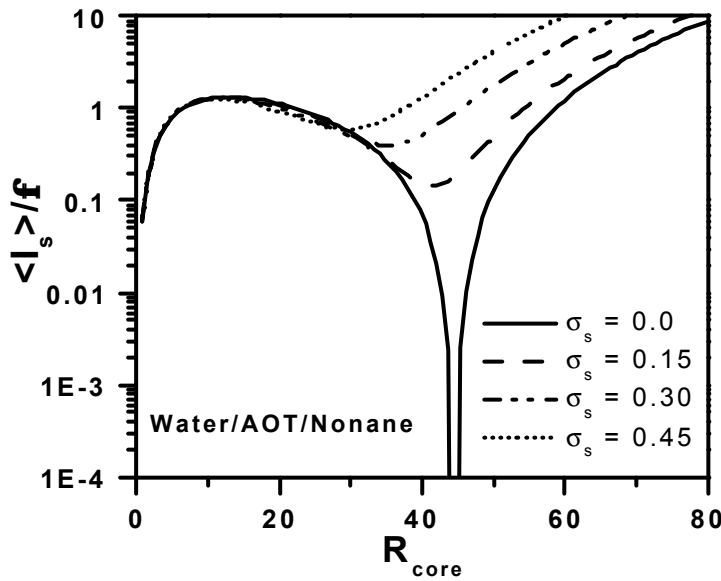


**Figure 3.1** Normalized scattered Intensity  $\langle I_s \rangle$  divided by  $\mathbf{f}$  for different value of  $\sigma_s$ , as the function of the radius of inner core  $R_{core}$ .

A ME droplet has inner core surrounded by a shell of surfactant (see Figure 1.1). Because of different dielectric constant (or refractive indices) for inner core ( $\mathbf{e}_{core}$ ) and surfactant ( $\mathbf{e}_s$ ), the optical contrast of the droplets changes with the water to AOT ratio. The continuous phase used may have dielectric constants  $\mathbf{e}_{solvent}$  that lies between those of inner core and surfactant. It is therefore possible to combine inner core and surfactant in such a proportion that the average dielectric constant of core plus surfactant is the same as that of the continuous phase used. For this particular composition of inner core and surfactant the droplets become “invisible” in a light scattering experiment. At this point, which is normally referred as the optical matching point, resulting excess polarizability  $\alpha_{excess}$  goes through zero. The layered sphere model in a simple linear mixing approximation, excess polarizability  $\alpha_{excess}$  can be obtained as<sup>8</sup>

$$(3.14) \quad \mathbf{a}_{excess} = 4\mathbf{p}\mathbf{e}_{solvent} \left[ E_{core} \times R_{core}^3 + E_s \times 3 \times \frac{v_s}{a_s} \times R_{core}^2 \right]$$

with, reduced dielectric constant  $E_i = \frac{\mathbf{e}_i - \mathbf{e}_{solvent}}{\mathbf{e}_i + 2\mathbf{e}_{solvent}}$

where  $v_s$  = specific volume of surfactant molecule and  $a_s$  = average area occupied by a surfactant molecule on the interface.

At the optical matching point, resulting excess polarizability  $\alpha_{\text{excess}}$  goes through zero. Therefore zero scattering intensity will be obtained at the matching point. However, if the droplets are polydisperse, scattering intensity exhibits a sharp dip but there remains a substantial residual scattering. This is because only the part of the ME droplets is completely matched and thus invisible. The depth and position of the characteristic dip of the scattering intensity at the optical matching are extremely sensitive to polydispersity. Optical contrast variation experiments thus permit a precise determination of the polydispersity of the droplet like ME particles.<sup>8</sup> This is illustrated in Figure 3.1, where normalized intensity  $\langle I_s \rangle / \phi$  from

Eqs. (3.13) and (3.14)  $\mathbf{s}_s = \sqrt{\frac{\langle R_{\text{core}}^2 \rangle}{\langle R_{\text{core}} \rangle^2}} - 1$  are shown as the function of  $R_{\text{core}}$  for the

polydisperse ME droplets stabilized by AOT surfactant in nonane. For our calculation we used Schulz size distribution.<sup>39</sup> We can see in Figure 3.1 that for monodisperse system, the scattering intensity is zero at optical matching point and for polydisperse system, depth and position of the characteristic dip of the scattering intensity in the vicinity of optical matching point are extremely sensitive to  $\sigma_s$ .

In order to be able to compare directly the intensity of light scattered by various liquids and macromolecular solutions, it is convenient to define the Rayleigh ratio  $R_q$  as follows<sup>28</sup>

$$(3.15) \quad R_q = \frac{I_{\text{excess}}}{I_0} \frac{R_p^2}{\sin^2 \mathbf{g}}$$

Eqs. (3.3) and (3.15) can be combined to obtain<sup>40,34</sup>

$$(3.16) \quad \frac{Kc}{R_q} = \frac{1}{M_{\text{app}}} + 2B_2c + \dots$$

with

$$\frac{1}{M_{\text{app}}} = \frac{1}{MP'(q)}$$

where  $M$  is the molecular weight of a scatterer,  $P(q)$  is the molecular form factor and  $c$  is the concentration of the droplets in a ME and  $K$ , the optical constant, is defined by

$$(3.17) \quad K = \frac{4\mathbf{p}^2 n^2}{I_0^4 N_A} \left( \frac{\partial n}{\partial c} \right)^2$$

Eq. (3.16) is the fundamental equation for SLS, which is used for data analysis.

### 3.2 DLS from ME Droplets

*DLS*, also known as *Photon Correlation Spectroscopy* or *quasi-elastic light scattering*, is a useful means of determining a droplet's size. While static light measurements provide a wealth of information (e.g. weight-average molar mass  $M_w$ , second osmotic virial coefficient  $B_2$ ), still more can be obtained by considering the real-time random (i. e. Brownian) motion of the solute molecules. This motion gives rise to a Doppler effect and so the scattered light possesses a range of frequencies shifted very slightly from the frequency of the incident light. These frequency shifts yield information relating to the movement (i. e. the dynamics) of the solute molecules. A very popular means of monitoring the motion of solute molecules is to record the real-time fluctuations in terms of the intensity time-correlation function  $g_2(\mathbf{t})$  of the scattered light (see Figure 3.2). Measurement of above mentioned intensity time-correlation function, yield hydrodynamic properties of the solute e.g. the diffusion coefficient of the droplet, which is related to the hydrodynamic radius by the Stokes-Einstein equation and size distribution as well as a description of the droplet's motion in the medium.

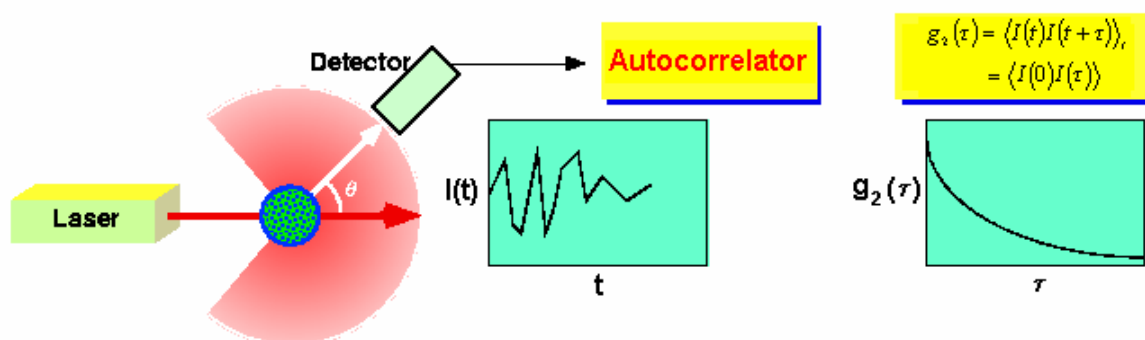


Figure 3.2 Typical dynamic light scattering.

As described above, scattered intensity autocorrelation function  $g_2(\delta) = \langle I(t)I(t+\delta) \rangle_t$  is usually detected with a photomultiplier tube (PMT) and fluctuations in the photo count rate (see Figure 3.2). But, the normalized field autocorrelation function  $g_1(\mathbf{t})$ , carries the information about the motions of droplets in a system and is a quantity of basic interest in DLS. The normalized field autocorrelation function  $g_1(\mathbf{t})$  has been derived from the measured scattered intensity autocorrelation function  $g_2(\mathbf{t})$  via Siegert relation<sup>27,33</sup>.

$$(3.18) \quad g_1(\mathbf{t}) = C\sqrt{1 - g_2(\mathbf{t})}$$

where the constant  $C$  is in the order of unity and dependent on instrumental conditions and the amount of back ground scattering from solvent etc.

In interpreting DLS data obtained from MEs, it will be assumed that: (i) over the range of intensity-fluctuation times of interest, the scattering is due entirely to the droplets and their associated interfacial layers, (ii) multiple scattering is negligible so that the first Born approximation is valid, (iii) the ME droplets are always much smaller than  $\lambda$  ( $\sim 532$  nm) so that their scattering amplitudes are independent of the scattering vector.

Under these conditions,  $g_l(\mathbf{t})$  can also be expressed in terms of the “measured” dynamic structure factor  $F(\mathbf{t})$  and the “measured” static structure factor  $S(\vec{q})$ , namely,<sup>27</sup>

$$(3.19) \quad g_l(\vec{q}, \mathbf{t}) = \frac{F(\vec{q}, \mathbf{t})}{S(\vec{q})}$$

With,

$$(3.20) \quad F(\vec{q}, \mathbf{t}) = [N\overline{f^2}]^{-1} \left\langle \sum_{i=1}^N \sum_{j=1}^N f_i f_j \exp \{i\vec{q}[\vec{r}_i(0) - \vec{r}_j(\mathbf{t})]\} \right\rangle$$

$$S(\vec{q}) \equiv F^M(\vec{q}, 0)$$

$N$  is the number of droplets in the scattering volume.  $\vec{r}_j(\delta)$  is the space position of the droplet  $j$  at time  $\mathbf{t}$ .  $f_i$  is the field amplitude of the light scattered by the droplet  $i$ , which for simplicity, will be assumed to be independent of time as well as the scattering wave vector. The bar indicates a number average over the distribution of scattering amplitudes (powers), while angular brackets represent the ensemble average or time average. Accordingly, the average and the mean-square scattering amplitude is given by

$$(3.21) \quad \overline{f} = \frac{1}{N} \sum_{i=1}^N f_i \quad \text{and} \quad \overline{f^2} = \frac{1}{N} \sum_{i=1}^N f_i^2$$

### 3.2.1 Monodisperse, Non-Interacting ME Droplets

In a non-interacting or very dilute monodisperse solutions the value of  $f_i$  and  $f_j$  are identical in Eq.(3.20), so interdroplet correlations disappear and  $S(\vec{q})$  reduces to unity,  $F(\vec{q}, \mathbf{t})$  becomes<sup>27</sup>

$$(3.22) \quad F(\vec{q}, \mathbf{t}) = \frac{1}{N} \left\langle \sum_{i=1}^N \sum_{j=1}^N \exp \{i\vec{q}[\vec{r}_i(0) - \vec{r}_j(\mathbf{t})]\} \right\rangle$$

$$= \frac{1}{N} \langle n(\vec{q}, 0) n^*(\vec{q}, \mathbf{t}) \rangle$$

In Eq. (3.22)  $n(\vec{q}, \mathbf{t})$  is the  $q^{\text{th}}$  spatial Fourier component of the number density  $n(\vec{r}, \mathbf{t})$ .

According to the Onsager regression hypothesis,<sup>41</sup> the time dependence of  $n(\vec{q}, \mathbf{t})$  can be obtained as<sup>33</sup>

$$(3.23) \quad \langle n(\bar{q}, \mathbf{t}) \rangle_0 = n(\bar{q}, 0) \exp(-Dq^2 \mathbf{t}) \quad (\mathbf{t} > 0)$$

where  $\langle \dots \rangle_0$  signifies a conditional average with  $n(\bar{q}, 0)$  as initial value. Substituting this time dependence in Eq. (3.22) one obtains

$$(3.24) \quad \begin{aligned} F(\bar{q}, \mathbf{t}) &= \frac{1}{N} \langle |n(\bar{q}, 0)|^2 \rangle \exp(-Dq^2 \mathbf{t}) \\ &= F(\bar{q}, 0) \exp(-\Gamma \mathbf{t}) \end{aligned}$$

where the relaxation rate  $\Gamma$  is related with the translational diffusion coefficient  $D$  according to

$$(3.25) \quad \Gamma = Dq^2.$$

Using the results expressed by Eqs. (3.24) in Eq. (3.19) one finally finds that

$$(3.26) \quad |g_1(\mathbf{t})| = \exp(-Dq^2 \mathbf{t})$$

In practice, the  $\mathbf{t} = 0$  delay intercept is 'A' where  $A \ll 1$ . Thus  $g_1(\tau)$  has the form

$$(3.27) \quad |g_1(\mathbf{t})| = A \exp(-Dq^2 \mathbf{t})$$

### 3.2.2 Polydisperse, Interacting ME Droplets

In general, ME systems contain a distribution of droplet sizes (polydispersity) and consequently a distribution of scattering amplitude so that  $g_1(\mathbf{t})$  becomes a summation, with weightings, over all the sizes present,

$$(3.28) \quad \begin{aligned} g_1(\mathbf{t}) &= A(w_1 e^{-D_1 q^2 \mathbf{t}} + w_2 e^{-D_2 q^2 \mathbf{t}} + \dots) \\ &= A \sum_{i=1}^m w_i e^{-D_i q^2 \mathbf{t}} \end{aligned}$$

where  $w_i$  corresponds to a weighting factor related to the relative abundance of droplets of a size indexed by  $i$ , and  $m$  stands for the number of sizes. Having a continuous distribution of sizes Eq. (3.27) can be replaced by,

$$(3.29) \quad |g_1(\mathbf{t})| = A \int_0^{\infty} G(\Gamma) \exp(-\Gamma \mathbf{t}) d\Gamma,$$

with

$$(3.30) \quad \int_0^{\infty} G(\Gamma) d\Gamma = 1$$

The distribution function of the decay rates,  $G(\mathbf{G})$ , can be broad continuous distribution, a series of discrete delta functions or some combination of two.  $G(\mathbf{G})d\mathbf{G}$  is the function of the total intensity scattered, on average, by molecules for which  $Dq^2 = \mathbf{G}$  within  $d\mathbf{G}$ . Various approaches to the characterization of  $G(\mathbf{G})$  have been developed. These approaches are discussed in detail in the Section 4.3.

For the situation when the droplet size distribution is fairly narrow, an approximate simplification has been proposed by Weissman.<sup>42</sup> This involves the assumption that the droplet correlation and dynamics are completely unaffected by the droplet size distribution and that the only important effect of the latter is to provide a distribution of scattering amplitudes. Using these assumptions the thermal average and the average over the droplet size distribution can be separated<sup>43</sup> in Eq. (3.20) to give

$$(3.31) \quad F(\bar{\mathbf{q}}, \mathbf{t}) = (1-x) F_c(\bar{\mathbf{q}}, \mathbf{t}) + x F_s(\bar{\mathbf{q}}, \mathbf{t})$$

where,

$$(3.32) \quad x = 1 - \frac{\bar{f}^2}{f^2}$$

$$(3.33) \quad F_c(\bar{\mathbf{q}}, \mathbf{t}) = \frac{1}{N} \left\langle \sum_{i=1}^N \sum_{j=1}^N f_i f_j \exp\{i\bar{\mathbf{q}}[\bar{r}_i(0) - \bar{r}_j(\mathbf{t})]\} \right\rangle$$

$$(3.34) \quad F_s(\bar{\mathbf{q}}, \mathbf{t}) = \left\langle \exp\{i\bar{\mathbf{q}}[r_i(0) - r_j(\mathbf{t})]\} \right\rangle$$

with  $F_c$  and  $F_s$  is the full dynamic structure and the self-dynamic structure factors respectively, which would be approximate in the absence of polydispersity.

Following an analysis of Kirkwood and Goldberg<sup>44</sup> for thermodynamic fluctuations of multicomponent systems, Pusey et al<sup>43</sup> argued that total number density fluctuation mode  $F_c(\bar{\mathbf{q}}, \mathbf{t})$ , is the equivalent description of the collective diffusion mode, and the concentration fluctuation mode  $F_s(\bar{\mathbf{q}}, \mathbf{t})$ , is equivalent to long time self diffusion mode. In the small  $q$ -limit and  $\mathbf{t} \gg \mathbf{t}_I$ , the “measured” dynamic structure factor is thus predicted to be<sup>43,45</sup>

$$(3.35) \quad F(\bar{\mathbf{q}}, \mathbf{t}) = (1-x) S^I(0) \exp(-D_c q^2 \mathbf{t}) + x \exp(-D_s q^2 \mathbf{t})$$

where  $\mathbf{t}_I$  is the collision time, between the droplets, which in a concentrated dispersion, are less than the time taken by the droplet to diffuse freely a distance equal to its diameter.  $D_c$  is the collective diffusion coefficient,  $S^I(0)$  is the static structure factor of the ideal monodisperse system and  $D_s$  is the self diffusion coefficient.

Macroscopic collective diffusion coefficient  $D_c$  (for detail see Appendix A) is given by

$$(3.36) \quad D_c = \frac{k_B T}{S^1(0) f_c} = \frac{\left( \frac{\partial \Pi}{\partial \mathbf{r}} \right)}{f_c}$$

where  $k_B$  is the Boltzmann's constant,  $T$  is the absolute temperature and  $f_c$  is the frictional coefficient associated with collective diffusion,  $\Pi$  is the osmotic pressure of suspension and  $\rho^{-1}(\partial \rho / \partial \Pi)$  called as an "osmotic compressibility",  $\rho$  is the density of droplets.

The macroscopic self diffusion coefficient  $D_s$  (for detail see Appendix A) is given by

$$(3.37) \quad D_s = \frac{k_B T}{f_s}$$

where  $f_s$  is the frictional coefficient for self diffusion of the ME droplets.

For  $\tau = 0$ , Eq. (3.35) yield the "measured" static structure factor  $S(0)$  which is in some cases theoretically obtainable, i.e.,

$$(3.38) \quad S(0) = (1-x)S^1(0) + x = A_1 + A_2$$

The Amplitude of the "self-mode" is  $A_2$  and  $A_1$  the amplitude of the "collective mode"

$$(3.39) \quad A_1 = (1-x)S^1(0) = \frac{\bar{f}^2}{f^2} k_B T \left( \frac{\partial \mathbf{r}}{\partial \Pi} \right)_{T, \mu_0}$$

where  $\mu_0$  is the chemical potential of the solvent.

For a mixture of hard spheres, the thermodynamic quantity  $k_B T (\partial \rho / \partial \Pi)_{T, \mu_0}$  can be obtained via the PY approximation.  $A_1$  is then given by<sup>43</sup>

$$(3.40) \quad A_1 = \frac{\bar{f}^2}{f^2} \frac{(1-f)^4}{\left( (1-f)^2 + \frac{6m_2}{m_3} f(1-f) + \frac{9m_2^3}{m_3^2} f^2 \right)}$$

where  $\phi$  is the droplet volume fraction,  $m_n$  are the normalized moments of droplet radius  $R$ , defined by

$$(3.41) \quad m_n = \frac{\overline{R^n}}{\bar{R}^n}$$

and thus can be related to the relative standard deviation of droplet radius.

Combining Eqs. (3.19), (3.35) and (3.38), one can get

$$(3.42) \quad g_1(\mathbf{t}) = \frac{A_1}{A_1 + A_2} \exp(-D_c q^2 \mathbf{t}) + \frac{A_2}{A_1 + A_2} \exp(-D_s q^2 \mathbf{t}).$$

The use of Eq. (3.42) under various limiting conditions can be discussed as follow:

- I. For monodisperse systems  $x = 0$ , and therefore  $g_1(\mathbf{t})$  measures only the collective diffusion process through the first term.
- II. For very dilute systems at the zero concentration limit,  $S^d(0) = 1$  and  $f_c = f_s = f_0$ , where  $f_0$  is given by the stokes expression, i.e.,

$$(3.43) \quad f_0 = 6\pi h R_h$$

$$(3.44) \quad D_0 = \frac{k_B T}{f_0} \Rightarrow R_h = \frac{k_B T}{6\pi h D_0}$$

where  $h$  is the viscosity of the continuous phase and  $R_h$  is the hydrodynamic radius of the droplet and  $D_0$  is the free droplet diffusion coefficient.

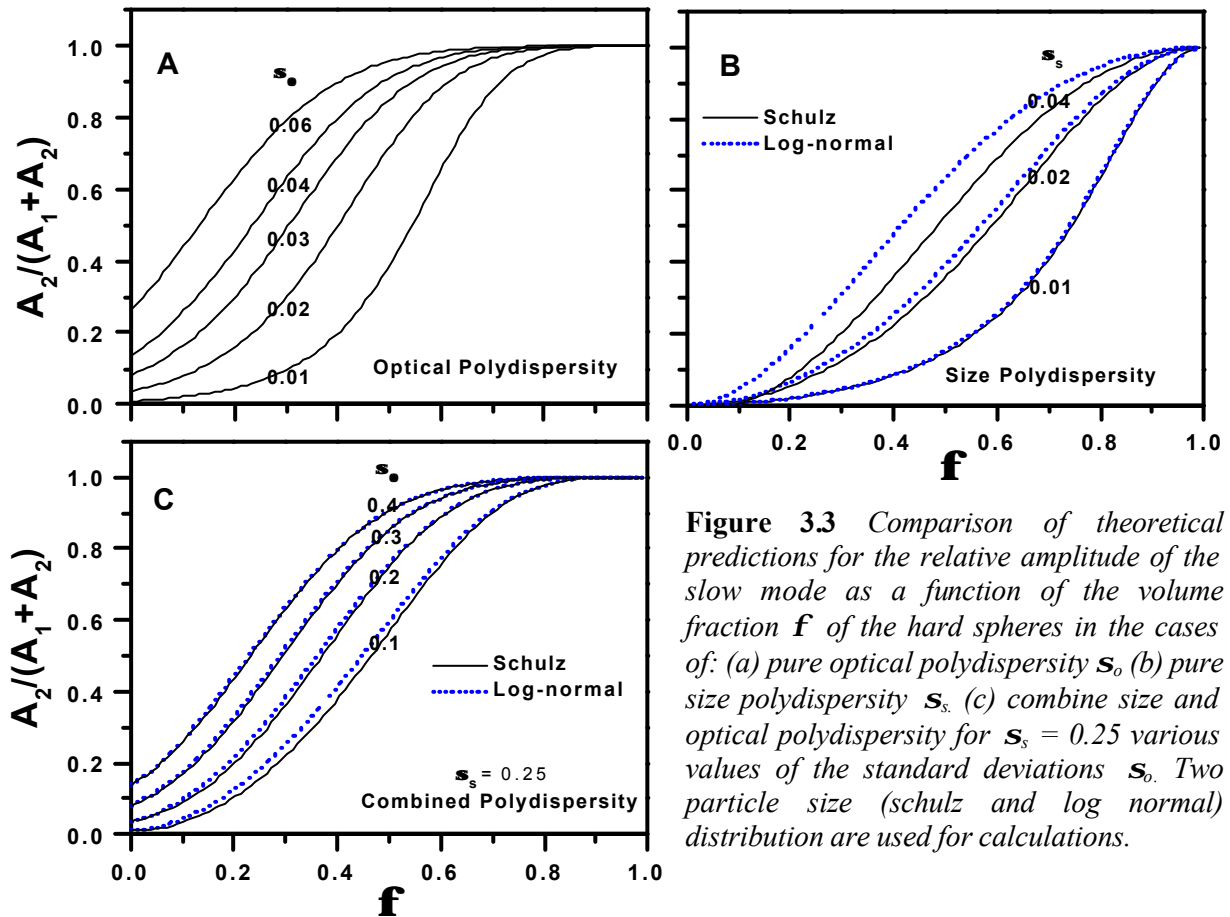


**Figure 3.3** Comparison of theoretical predictions for the relative amplitude of the slow mode as a function of the volume fraction  $f$  of the hard spheres in the cases of: (a) pure optical polydispersity  $s_o$ , (b) pure size polydispersity  $s_s$ , (c) combine size and optical polydispersity for  $s_s = 0.25$  various values of the standard deviations  $s_o$ . Two particle size (schulz and log normal) distribution are used for calculations.

The Relative amplitude of slower decaying mode,  $\frac{A_2}{A_1 + A_2}$  can be used as a measure of the polydispersities in size and refractive index.<sup>46,47</sup> Theoretical predictions (see Appendix B) for the relative amplitude of the slow mode as a function of the volume fraction  $f$  in the cases of:

(a) pure optical polydispersity  $\mathbf{s}_o = \sqrt{\frac{\langle f^2 \rangle}{\langle f \rangle^2}} - 1$  [ $f \propto (\langle n \rangle - n_o)$   $n$  and  $n_o$  refer to refractive indices of the droplets and the solvent respectively] (b) pure size polydispersity  $\mathbf{s}_s = \sqrt{\frac{\langle R^2 \rangle}{\langle R \rangle^2}} - 1$  are shown in Figure 3.3A & 3.3B. The optical i.e., refractive index and the size variation are completely coupled because variation in the droplet size gives rise to a distribution in the droplet refractive indices too. Coupled combination of  $\sigma_s$  and  $\sigma_o$  approach was used to estimate the values for the polydispersity in size and refractive index (shown in Figure 3.3C). It can be shown that  $\frac{\mathbf{s}_o^2}{1 + \mathbf{s}_o^2}$  equals the ratio of the scattered intensity at the matching point ( $n \sim n_b$ ) to the measured scattered intensity; provided these measurements were taken with the same dilute samples.<sup>46</sup> This is used as the rule of thumb to estimate the influence of optical polydispersity alone.

### 3.3 Volume Fraction Dependence of Diffusion Coefficient

Particles in the liquid dispersion, be they solid colloidal particles, micelles or ME droplets, are in continual erratic Brownian motion whose average properties are usually described in terms of diffusion coefficients. The detailed nature of these diffusion processes is of interest for several reasons:

- I. They are determined by the fundamental composition of the dispersion, in particular by the interactions between the particles, and thereby constitute a challenging theoretical problem.
- II. Diffusion coefficients can be measured quite accurately by DLS, neutron scattering and nuclear magnetic resonance, etc.
- III. Many properties of the dispersion, e.g. reactions, can be controlled by diffusion.

Consider a non interacting system of suspended particles with a number density  $n$ . Local difference in this density will smooth out by the process of diffusion. This tendency can be described by the diffusion equation<sup>48</sup>

$$(3.45) \quad \frac{\partial n(\vec{r}, t)}{\partial t} = D_0 \nabla^2 n(\vec{r}, t)$$

where  $D_0$  is the free diffusion coefficient given by Einstein relation [see Eq. (3.44)].

In general however, system will interact via both static and hydrodynamic interactions. On the time scale measured in light scattering experiments the system of interacting Brownian particles is described by the generalized Smoluchowski equation<sup>27</sup>

$$(3.46) \quad \frac{\partial n(\vec{r}, t)}{\partial t} = D_0 \vec{\nabla} \cdot \left( \vec{\nabla} n(\vec{r}, t) + n(\vec{r}, t) \vec{\nabla} \frac{U}{k_B T} \right)$$

Interparticle interactions are represented by potential  $U$ . The generalized Smoluchowski equation provides a description of the particle motion, which is adequate for the discussion of DLS.

For highly concentrated polydisperse suspensions where hydrodynamic interactions become more important, there will be two fluctuation modes [see Eq. (3.31)]. The Fast mode is due to collective diffusion  $D_c$ , where as the other slow is due to self diffusion  $D_s$ .  $D_c$  describes the diffusive motion of an object among other similar objects when concentration is not uniform. In DLS experiment,  $D_c$  is associated to concentration fluctuations and goes to zero at a critical point.  $D_s$  describes the diffusive motion of a tracer object in an uniform medium.  $D_s$  is associated to size or connectivity fluctuations and goes to zero at a percolation point (formation of an infinite aggregates of droplets). These measured collective and self diffusion coefficients can be represented as an expansion in powers of the volume fraction  $\mathbf{f}$  as<sup>49</sup>

$$(3.47) \quad D_{c,s} = D_0 \left( 1 + \mathbf{a}_1^{c,s} \mathbf{f} + \mathbf{a}_2^{c,s} \mathbf{f}^2 \dots \right)$$

where  $D_0$  is the free diffusion coefficient and  $\mathbf{a}_1^{c,s}$  and  $\mathbf{a}_2^{c,s}$  ( $s$  refers to self and  $c$  refers to collective) are the virial coefficients of diffusion (For detail see Appendix A). For hard spheres,<sup>49</sup>  $(\mathbf{a}_1^c)^{HS} = 1.56$ ,  $(\mathbf{a}_1^s)^{HS} = -2.01$ .

In the diluted region the difference between  $D_c$  and  $D_s$  is expected to be small as can be seen from Eq. (3.47). Therefore in the diluted region, resolution of the measured autocorrelation function by a sum of two exponents will be difficult. Analyzing the obtained functions by a single exponent (or cumulants) gives an apparent diffusion coefficient  $D_{app}$ , which can be related to the first  $D_c$  and  $D_s$  using an expansion for both exponents of Eq. (3.31). One can obtain<sup>47</sup>

$$(3.48) \quad \frac{D_{app}}{D_0} = 1 + [\mathbf{a}_1^c (1-x) - \mathbf{a}_1^s x] \mathbf{f}$$

$$(3.49) \quad \frac{D_{app}}{D_0} = 1 + k_{app}(\mathbf{f})$$

$$\text{where } x = 1 - \frac{\bar{f}^2}{f^2}.$$

Far from the matching point,  $x = 0$ , where as in the matching point itself  $(1-x) = 0$ .

### 3.4 SANS from Interacting ME Droplets

ME usually consists of droplets of relatively stable structure that can be distinguished from the solvent. Thus it is more convenient to consider each droplet as a scattering centre. Suppose the sample contains  $N_p$  droplets immersed in a homogeneous solvent. Then one can imagine the sample volume  $V$  to be partitioned into  $N_p$  cells, each containing exactly one droplet. The differential cross-section per unit volume, which contains all the information on the shape, size and interactions of the droplets (assemblies of scattering centers) in the sample, is given by the following ensemble average<sup>26</sup>

$$(3.50) \quad \frac{d\Sigma(\vec{q})}{d\Omega} = \frac{1}{V} \frac{d\mathcal{S}(\vec{q})}{d\Omega} = \frac{1}{V} \left\langle \left| \sum_{i=1}^{N_p} \sum_{j=1}^{N_i} b_{ij} \exp[i\vec{q}\vec{r}_{ij}] \right|^2 \right\rangle$$

where  $b_{ij}$  and  $\vec{r}_{ij}$  are the scattering length and position of the  $j^{\text{th}}$  nucleus in the  $i^{\text{th}}$  cell.  $N_i$  is the number of nuclei in the  $i^{\text{th}}$  cell.  $\frac{d\Sigma(\vec{q})}{d\Omega}$  has dimensions of  $(\text{length})^{-1}$  and is normally expressed in units of  $\text{cm}^{-1}$ .

Eq. (3.50) can be understood as the result of the interference between the neutrons scattered from each nucleus in the sample. In general, the scattering length  $b_{ij}$  depends on the situation of the scattering nucleus as well as on the spin states. Therefore, it would be more convenient to separate the scattering cross-section into a coherent and an incoherent part. The numerical values of the scattering lengths for nearly all isotopes are tabulated in ref.<sup>50</sup> which vary randomly within the range of  $-6 \times 10^{-15}$  to  $+25 \times 10^{-15}$  m. The spin dependence of the nuclear scattering is responsible for the high incoherent scattering cross-sections of hydrogen. Therefore, in practice the incoherent scattering is appreciable only from hydrogen atoms. Since the contribution from the incoherent part is simply a flat background that can be calculated by knowing the number density of hydrogen atoms.<sup>26</sup> In the subsequent discussion the differential scattering cross-sections refer to the coherent part only.

Denoting the centre of droplet  $i$  by  $\vec{R}_i$  and the position of a nucleus at  $\vec{r}_{ij}$  relative to this point by  $\vec{x}_j$ , one can make the decomposition  $\vec{r}_{ij} = \vec{R}_i + \vec{x}_j$ . Then,

$$(3.51) \quad \frac{d\Sigma(\vec{q})}{d\Omega} = \frac{1}{V} \left\langle \left| \sum_{i=1}^{N_p} \exp(i\vec{q}\vec{R}_i) \sum_{j=1}^{N_{is}} b_{ij} \exp(i\vec{q}\vec{x}_j) \right|^2 \right\rangle.$$

Now define the form factor  $F_i(\vec{q})$  of  $i^{\text{th}}$  droplet as

$$(3.52) \quad F_i(\vec{q}) = \sum_{j=1}^{N_{is}} b_{ij} \exp(i\vec{q}\vec{x}_j).$$

Then,

$$(3.53) \quad \frac{d\Sigma(\vec{q})}{d\Omega} = \frac{1}{V} \left\langle \sum_{i=1}^{N_p} \sum_{i'=1}^{N_p} F_{i'}^*(\vec{q}) F_i(\vec{q}) \exp[i\vec{q}(\vec{R}_i - \vec{R}_{i'})] \right\rangle.$$

The form factor  $F_i(\vec{q})$  is expressed in terms of the individual scattering lengths of the nuclei in the cell containing the  $i^{\text{th}}$  droplet. Generally one can not divide the sample volume into  $N_p$  scattering segments separated from each. So that one turns into to a continuous formulation for the form factor. In this case, it is more convenient to express the form factor in terms of scattering length densities, thus rewriting Eq. (3.52) as One defines the microscopic, and it follows

with,

$$(3.54) \quad F_i(\vec{q}) = \int_{\text{celli}} d\vec{r}^3 \mathbf{r}_i(\vec{r}) \exp[i\vec{q}\vec{r}],$$

where

$$(3.55) \quad \mathbf{r}_i(\vec{r}) = \sum_{j=1}^{N_i} b_{ij} \mathbf{d}(\vec{r} - \vec{x}_j)$$

is the scattering length density (SLD) at position  $\vec{r}$  of the  $i^{\text{th}}$  cell. It is preferable to transform the form factor to an integral over the droplet volume only. Then Eq. (3.54) can be expressed as

$$(3.56) \quad F_i(\vec{q}) = \int_{\text{droplet } i} d\vec{r}^3 [\mathbf{r}_i(\vec{r}) - \mathbf{r}_s] \exp[i\vec{q}\vec{r}] + \mathbf{r}_s \int_{\text{cell } i} d\vec{r}^3 \exp[i\vec{q}\vec{r}],$$

where  $\rho_s(\mathbf{r})$  is the SLD of solvent. Since the second integral is simply a  $\delta$  function centered at  $\vec{q} = 0$ , we obtain

$$(3.57) \quad F_i(\vec{q}) = \int_{\text{droplet } i} d\vec{r}^3 [\mathbf{r}_i(\vec{r}) - \mathbf{r}_s] \exp[i\vec{q}\vec{r}] \quad \vec{q} \neq 0.$$

Up to this point, the derivation of the scattering cross-section has been completely general for identical droplet. When considering droplets are polydisperse, the form factor varies from droplet to droplet. In that case, one can write<sup>51</sup>

$$(3.58) \quad \frac{d\Sigma(\vec{q})}{d\Omega} = \frac{1}{V} \left\langle \sum_{i=1}^{N_p} \sum_{i'=1}^{N_p} \langle F_{i'}^*(\vec{q}) F_i(\vec{q}) \rangle \exp[i\vec{q}(\vec{R}_i - \vec{R}_{i'})] \right\rangle$$

where the small angular bracket represents an average weighted by the distribution of droplet sizes. This average can be decomposed into

$$(3.59) \quad \langle F_i^*(\vec{q})F_i(\vec{q}) \rangle = \left[ \langle |F_i(\vec{q})|^2 \rangle - \langle F_i(\vec{q}) \rangle^2 \right] \mathbf{d}_{ii} + \langle |F_i(\vec{q})|^2 \rangle$$

If the scattering unit is itself a collection of objects e.g., ME droplets, the summations of Eq. (3.58) are to be taken for all the pairs  $i$  and  $i'$ , both in the droplets and between the droplets. It is therefore convenient to group these contributions into two parts. One obtains Eq. (3.58) combining with Eq. (3.59) as<sup>51,52,33</sup>

$$(3.60) \quad \frac{d\Sigma(\vec{q})}{d\Omega} = n_p P(\vec{q}) S'(\vec{q})$$

with,

$$(3.61) \quad P(\vec{q}) = \langle |F(\vec{q})|^2 \rangle \quad \text{and} \quad S'(\vec{q}) = 1 + \mathbf{b}(\vec{q})[S(\vec{q}) - 1]$$

with

$$S(\vec{q}) = \frac{1}{N_p} \left\langle \sum_{i=1}^{N_p} \sum_{i'=1}^{N_p} \exp[i\vec{q}(\vec{R}_i - \vec{R}_{i'})] \right\rangle \quad \text{and} \quad \mathbf{b}(\vec{q}) = \frac{\langle |F(\vec{q})|^2 \rangle^2}{\langle |F(\vec{q})|^2 \rangle}$$

We see that differential cross-section per unit volume is proportional to the droplet density  $n_p = N_p/V$  and a product of the droplet form factor  $P(\vec{q})$  and the apparent interdroplet structure factor  $S'(\vec{q})$ .  $\mathbf{b}$  is a  $\vec{q}$ -dependent factor between zero and one, which suppresses the oscillations of the average structure factor  $S(\vec{q})$  in the observed scattering spectrum from a polydisperse system.

### 3.5 The Form Factor

The form factor  $F(\vec{q})$  is a function that describes how the scattered intensity is modulated by interference effects between radiations scattered by different parts of the same scattering body. It depends only on the shape of the colloidal droplet when the scattering density is uniform. Since the form factor depends on the relative SLD between the droplet and solvent [see Eq. (3.54)], it implies that one may change the contrast by varying  $\mathbf{r}_s$  to look at different parts of the droplet, if the droplet has portions with different scattering densities. Theoretically, the form factor can be computed from a structural model of the colloidal droplet.<sup>29</sup> For a homogeneous spherical droplet of radius  $R$ , the integration in Eq. (3.57) can be carried out to give

$$(3.62) \quad F(\vec{q}) = \Delta \mathbf{r} V_{sphere} \frac{3[\sin(qR) - qR \cos(qR)]}{(qR)^3}$$

$$P(\vec{q}) = \langle |F(\vec{q})|^2 \rangle = \left[ \langle |F(\vec{q})|^2 \rangle \right] = 9(\Delta \mathbf{r} V_{sphere})^2 \frac{j_1^2(qR)}{q^2 R^2}$$

where  $\Delta\rho$  is the difference between the SLD of the droplet and the solvent and  $j_1(x) = \frac{(\sin x - x \cos x)}{x^2}$  is the first order spherical Bessel function.

The extension of  $F(\vec{q})$  to spherical core shell droplets (Figure 3.4) is straightforward and is useful for the calculation of  $P(\vec{q})$  of MEs having internal core of a radius  $R_{core}$  (SLD,  $\rho_{core}$ ) surrounded by a surfactant shell with an outer radius  $R_{shell}$  (SLD,  $\rho_{shell}$ ).<sup>26</sup>

$$(3.63) \quad F(\vec{q}) = V_{core}(\rho_{core} - \rho_{shell}) \frac{3j_1(qR_{core})}{qR_{core}} + V_{shell}(\rho_{shell} - \rho_s) \frac{3j_1(qR_{shell})}{qR_{shell}}$$

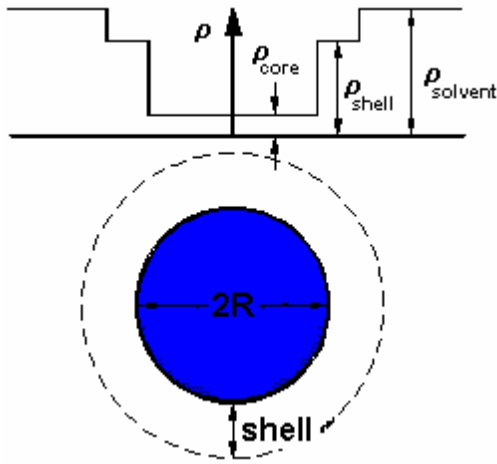


**Figure 3.4** Core Shell Sphere droplet model and SLD profile of droplet.

The behavior of  $P(\vec{q})$  at different regions of  $\vec{q}$  is shown in Figure 3.5. At small  $\vec{q}$  (more exactly, at values of  $\vec{q}$  smaller than the inverse of the characteristic dimension of the droplet, so called Guinier region  $qR \leq 1$ ), the spatial resolution is not sufficient to determine the shape, and only information about the size can be obtained.

Under these conditions (For small  $x$ ,  $j_1(x) = 1 - x^2/10 + \dots$ , and hence the small  $q$ ),  $P(\vec{q})$  follows the well known Guinier law<sup>29</sup>

$$(3.64) \quad P(\vec{q}) = (V_{sphere} \Delta\rho)^2 \exp\left(-\frac{R_g^2 q^2}{3}\right) \quad \text{with} \quad R = \sqrt{\frac{5}{3}} \cdot R_g$$

$R_g$  is the so called radius of gyration and  $R$  is radius of a hard sphere.

For values of  $\vec{q}$  much larger than the inverse of the smallest dimensions of the droplet,  $P(\vec{q})$  follows the equation of Porod:

$$(3.65) \quad P(\vec{q}) = 2\mathbf{p}(\Delta\rho)^2 \left(\frac{S}{V}\right) q^{-4}$$

where  $S/V$  is the total area of the interface per unit of the volume of the droplet.

It is at the intermediate range that  $P(\bar{q})$  contains the maximum of information about the size and shape of the droplets. When there is some information about the shape of colloidal droplet, the fitting of the data consists to compare the theoretical  $P(\bar{q})$  to the real data.

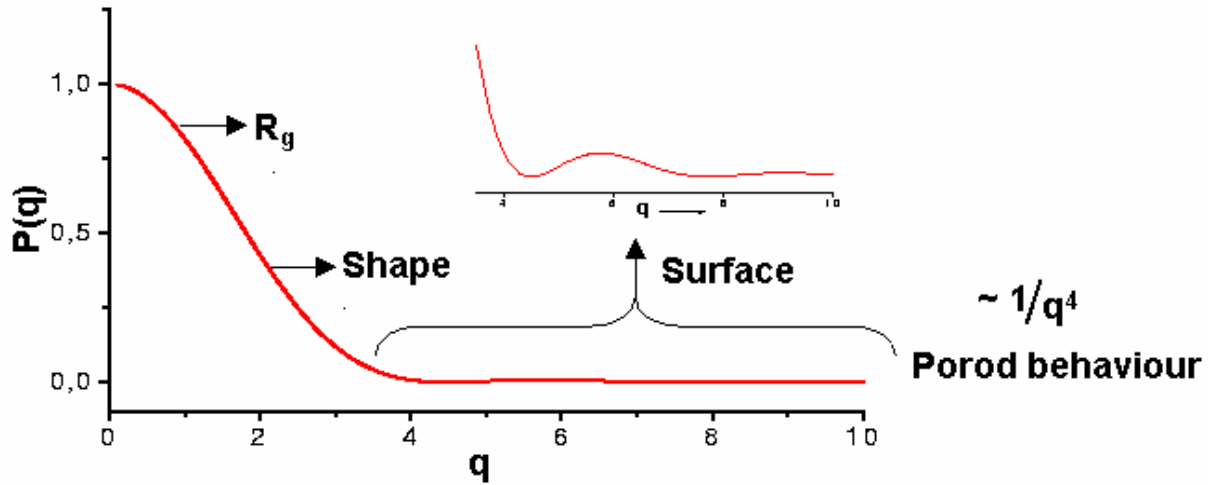


Figure 3.5 Different regions of the form factor.

### 3.6 The Structure Factor $S(\bar{q})$ and Pair Distribution Function $g(r)$

The Structure factor  $S(\bar{q})$  is a function that describes how the scattered intensity is modulated by interference effects between radiations scattered by different scattering bodies. Consequently it depends on the degree of local order in the sample, such as might arise in interacting system for example. Real-space solution structure factor  $S(\bar{q})$  can be determined by Fourier transformation of  $S(\bar{q})$  to the interdroplet pair distribution function  $g(r)$ , which measures the probability of finding a droplet at a distance  $r$  from a given reference.<sup>53,33</sup>

$$(3.66) \quad S(\bar{q}) = 1 + n_p \int d\bar{r}^3 e^{i\bar{q}\bar{r}} (g(r) - 1)$$

Calculation of  $g(r)$  from a given interdroplet potential is the central problem of liquid-state theory.<sup>54</sup> While no exact calculation is available, a number of approximate methods have been developed<sup>55</sup> The simplest approximation consists of the dilute-gas result

$$(3.67) \quad g(r) \approx \exp[-\mathbf{b}U(r)] \quad \text{with} \quad \mathbf{b} = \frac{1}{k_B T}$$

where,  $U(r)$  is interdroplet potential between a pair of droplets.

This is the approximation which has been used to analyze the light scattering data. In fact, dilute gas approximation is simply the first term in a convergent density expansion of  $g(r)$ <sup>56</sup>

$$g(r) = \exp[-\mathbf{b}V(r)] \{1 + n_p y_1(r) + n_p^2 y_2(r) + \dots\}$$

(3.68) 
$$y_k = \frac{1}{k!} \sum \int \dots \int d\{r_k\} \prod f_{ij}$$

$$f_{ij} = \exp[-\mathbf{b}U(r_{ij})] - 1 \quad \text{Mayer function}$$

where  $y_i(r)$  are cluster integrals<sup>33</sup> which may be evaluated numerically for any given potential and  $\Sigma$  means sum over all allowed conducting diagrams of  $f$  bonds on two white circles and one or more black circles, with no direct bond between the white. Where, white circle represent the interacting droplets. Each black circle describes a field droplet whose coordinate is integrated. Each connecting line is a Mayer  $f$  Function ( $f$  bond). In practice, evaluation of the  $y_i$  becomes prohibitive beyond about  $y_2$ , but the calculation of increasingly high-order terms is an excellent method to determine the extent to which convergence has occurred. A rather different approach is involved in approximation such as Percus - Yevick (PY) approximation,<sup>30</sup> Hypernetted - Chain (HNC) approximation, the mean spherical approximation,<sup>57</sup> perturbation approaches and computer simulation in which certain terms are summed to all orders in the density and others are ignored altogether.<sup>58</sup> All possible diagrams<sup>33</sup> for  $y_1, y_2$  and  $y_3$  using HNC and PY approximations are shown in Figure 3.6. PY approximation is most satisfactory for hard sphere, short range potential even repulsive soft spheres, PY approximation is not satisfactory for attractive force. The HNC approximation complement of the PY approximation. It is unsatisfactory for hard sphere but appears to account satisfactory for the effect of the attractive force and non hard core forces.

	Exact	HNC	PY
$n_p$			
$n_p^2/2!$	$2 + 4 + 1 + 1$ 	$2 + 4 + 1$ 	$2 + 4$ 
$n_p^3/3!$	$6 + 6 + 12 + 12$  $6 + 12 + 12 + 6$  $6 + 6 + 6 + 6$  $12 + 1 + 3 + 12$  $12 + 3 + 3 + 6$  $6 + 6 + 3 + 1$ 	$6 + 6 + 12 + 12$  $6 + 12 + 12 + 6$  $6 + 6$  $12 + 1$ 	$6 + 6 + 12 + 12$  $12 + 12$  $6$ 

Figure 3.6 All graphs representing the Eq.(3.68). are arranged according to the powers on  $n_p$  and along with the comparison of other approximations. Each graph consists of two white circles, which mark the interacting droplets. Each black circle describes a field droplet whose coordinate is integrated. Each connecting line is Mayer  $f$  Function ( $f$  bond).

The PY can be solved for hard sphere potential analytically<sup>54</sup>. The structure factor resulting from it is used in this work. Structure factor for hard sphere potential using PY approximation<sup>33,30</sup> is

$$S_{pY}(K) = \frac{1}{1 - n_p c(K)} \quad K = dq$$

$$(3.69) \quad c(K) = -\frac{4pd^3}{K^3} \left\{ \mathbf{a}_0 K^3 (\sin K - K \cos K) + \mathbf{b}_0 K^2 [2K \sin K - (K^2 - 2)\cos K - 2] \right. \\ \left. + \mathbf{g}_0 [\sin K (4K^3 - 24K) - (K^4 - 12K^2 + 24)\cos K + 24] \right\}$$

$$\mathbf{a}_0 = \frac{(1 + 2\mathbf{j})^2}{(1 - \mathbf{j})^4} \quad \mathbf{b}_0 = -\frac{6\mathbf{j} \left(1 + \frac{\mathbf{j}}{2}\right)^2}{(1 - \mathbf{j})^4}$$

$$\mathbf{g}_0 = \frac{\mathbf{j}\mathbf{a}_0}{2} \quad \mathbf{j} = \frac{\mathbf{P}}{6} n_p d^3$$

where  $d = 2R$  and  $n_p$  are the droplet diameter and droplet number density, respectively.

### 3.7 Interdroplet Interaction

In a two component system composed of particles and liquid, mainly two types of interaction potential act on a droplet as shown in the Figure 3.7

#### Direct:

via the intermolecular interaction potential, and

#### Indirect:

Due to the presence of the other droplets.

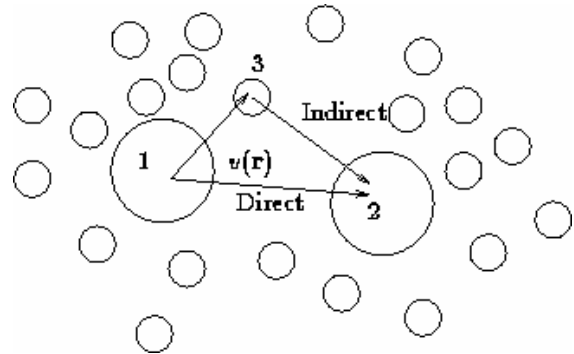


**Figure 3.7** Interaction between two droplets, dispersed into the medium.

Assume that interdroplet interaction has pair wise form so the pair interaction potential can be written as

$$(3.70) \quad U(r) = U_{\text{effective}}(r) = U_{\text{Direct}}(r) + U_{\text{Indirect}}(r).$$

The first potential is due to the direct interaction between the droplets, e.g., a shielded coulombic potential between charged droplets or simply an “excluded-volume” or “hard-sphere” or dispersion forces. The hard sphere potential ( $U_{HS}$ ) represents short range strong repulsive force that ensures the identity of ME and prevents the overlap of different ME. Dispersion forces arise from the fact that in any material thermal motion and quantum effects

produces local charge fluctuations. This force is responsible for Brownian motion of isolated droplets and at  $r \rightarrow \infty$ ,  $U_{dis} \sim -\frac{1}{r^6}$ .

The second indirect interaction  $U_{ind}$  is the coupling between droplet motions transmitted indirectly by the flow they induce in the liquid.

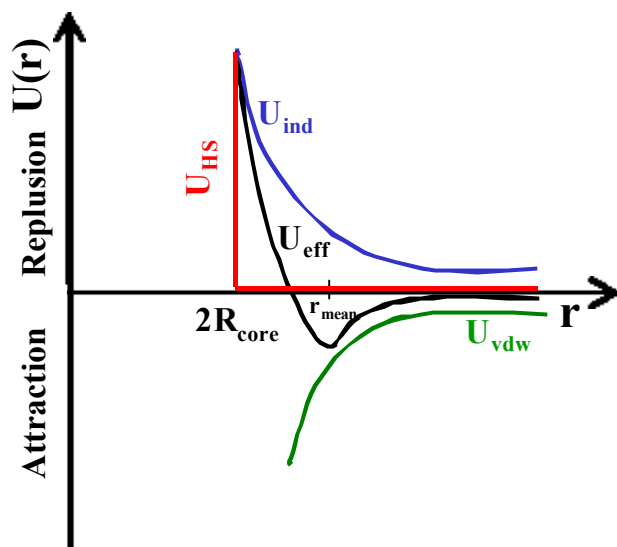


**Figure 3.8** The total interaction potential  $U_{eff}$  as a function of the distance of the surface separation ( $r$ ) for two similar ME droplets.

The total interaction potential  $U_{eff}$  as a function of the distance of the surface separation ( $r$ ) for two similar ME droplets is shown in Figure 3.8. The adsorbed emulsifier stabilizes the system by the introduction of additional repulsive force (e.g., electrostatic or steric) that counteract the dispersive force and prevents the close approach of droplets. Electrostatic effects are particularly important with ionic emulsifier whereas steric effects dominate with nonionic emulsifier. DLVO theory, which was developed independently by Derjaguin and Landau and by Verwey and Overbeek to analyze the influence of electrostatic forces on the stability of lyophobic colloidal droplets, has been adapted to describe the influence of similar forces on the flocculation and stability of simple model emulsions.<sup>33</sup>

The DLVO theory does not explain either the stability of water in oil MEs or the stability of oil-in-water MEs stabilized by adsorbed nonionic surfactants where the electrical considerations are often of secondary importance. In these, steric and hydrational forces, which arise from the loss of entropy when adsorbed hydrated chains of nonionic polyether surfactants intermingle on close approach of two similar droplets, are more important. Therefore for our oil-in-water MEs systems, which are stabilized by nonionic surfactants, we used interdroplet potential which account for the hard sphere, Van der Waals interaction potential among the droplets as well as local free energy associated with a given configuration of the droplets. Detailed review of such potential has been given in results and discussion chapter.

## 4 Data Acquisition and Treatment

### 4.1 Data Acquisition: Static and Dynamic Light Scattering

All light scattering measurements were carried out in a commercially available apparatus for simultaneous static and dynamic experiments made by ALV-Laser Vertriebsgesellschaft m.b.H. Langen, Germany shown in Figure 4.1.

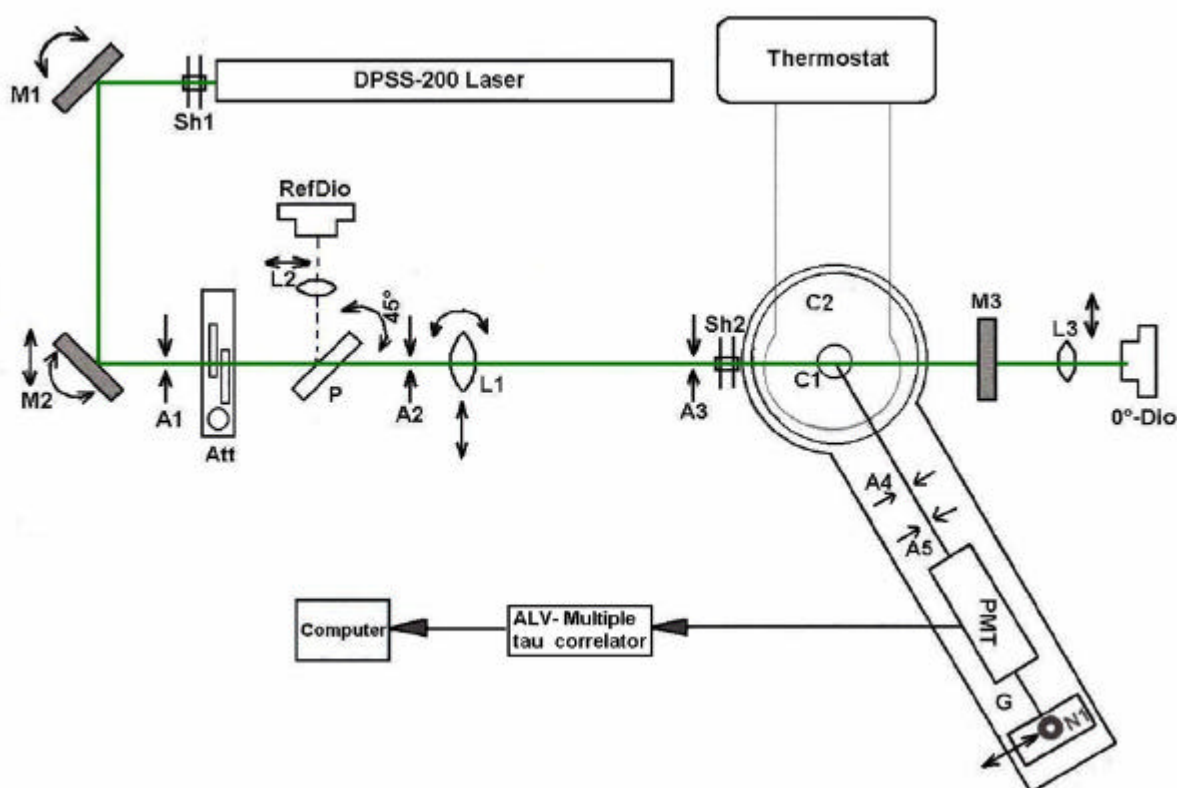


**Figure 4.1** Light Scattering Apparatus. *Sh1* and *Sh2* (Shutter), *M1* – *M3* (Mirrors), *A1* – *A5* (Apertures), *P* (Beam splitter plate), *Att* (Beam attenuator), *RefDio* (Reflection quadrant photodiodes), *L1* – *L3* (Bispherical lens), *C1* (Probe holder), *C2* (Therostated measurement cell), *g* (Goniometer), *PMT* (Photomultiplier tube), *ALV* (ALV- 5000/Fast correlator board).

To reduce effects from structure borne vibrations this apparatus is mounted on a vibration-damped optical table. As the light source vertically polarized green Nd: YAG DPSS-200 laser (532 nm) from Coherent, Auburn, CA, USA with an output of 200 mW was used. In case of high scattered light intensity, the incident beam intensity can be reduced by a liquid crystal attenuator. After passing the attenuator (*Att*) the incident intensity and beam position were analyzed using a quadrant-photodiode (*RefDio*) coupled with a beam splitter plate (*P*).<sup>27,59</sup>

Afterwards the laser light is focused using a bispherical lens (L1) into the sample. The sample cell was positioned in the center of the scattering cell (C2), which is filled with toluene in order to minimize reflections from the interface. The cylindrical sample cells C1 were made of Suprasil<sup>®</sup> quartz glass by Hellma, Muellheim, Germany and had a diameter of 10 mm. The temperature of the quartz glass-made sample cell was controlled ( $\pm 0.01\text{K}$ ) by a single Lauda-type RC6 thermostat with circulating water as the medium. The scattering cell was provided with special planer apertures that allowed diffraction of the incident and unscattered light passing through the device to be reduced effectively. Transmitted parts of light were analyzed by quadrant-photodiode ( $0^\circ$  Diode) at the end of optical path. For analyzing the scattered light the thermostated scattering cell is placed on a motor-driven precision goniometer ( $\pm 0.01^\circ$ ) which enables the photomultiplier detector to move from  $20^\circ$  to  $150^\circ$  scattering angle. A fast photon count digital correlator ALV-5000/Fast in combination with a laboratory computer was connected directly to the photomultiplier, which enable to obtain the intensity time-correlation functions (ITCF)  $g_2(\tau)$  for a dynamic analysis of scattered light. The minimal sampling time of this correlator is 12.5 ns. The correlator, originally developed by Schätzel,<sup>60,61,62</sup> is provided with 288 channels which are set in a logarithmic scale. The complete optical construction is adjusted with respect to the position of the cuvette and it is controlled and checked with calibration scattering measurements. To determine the quality of optical adjustment, test measurements were carried out with pure toluene as a scattering medium showing no angle dependence of the scattering intensity. During the whole measurement period the angle dependence of scattered light intensity was less than 3%. The photo detector is, of course, unable to follow the rapid changes of the optical field. Because of its quadratic characteristics curve, it produces a photocurrent  $i(\omega)$  which according to the integral

$$(4.1) \quad i(\omega) = \hat{i} \int_{-\infty}^{\infty} S_E(\omega' - \omega) d\omega$$

is given by the amplitude spectrum  $S_E(\omega)$  of the scattered light. Where  $\hat{i}$  denotes an amplitude and  $\omega = 2\pi\nu$  is the angular frequency of the optical signal.

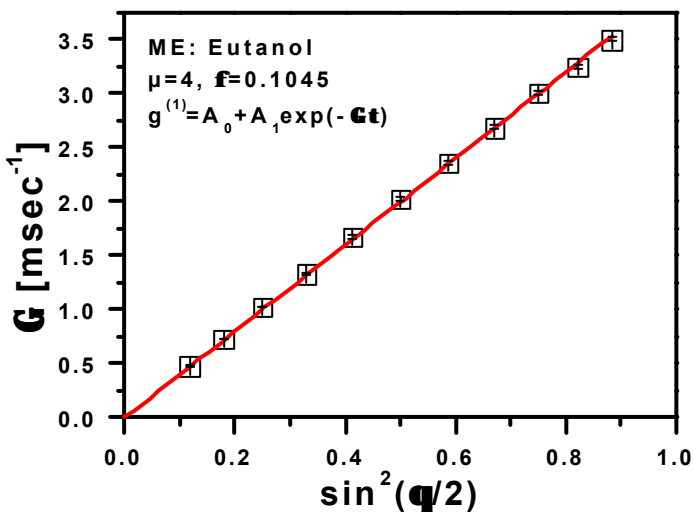


**Figure 4.2** The relaxation rate  $G$  of the photon autocorrelation function displayed versus  $\sin^2(q/2)$ .

The Rayleigh line is a Lorentzian. If its half power width is denoted by  $\frac{\Gamma}{2}$ , the photocurrent is given by

$$(4.2) \quad i(\mathbf{w}) = \hat{i} \frac{\Gamma}{\mathbf{w}^2 + \Gamma^2}$$

and relaxation rate  $\Gamma$  is related with the translational diffusion coefficient  $D$  according to the Eq. (3.25), which yield relation<sup>63</sup>

$$(4.3) \quad \Gamma = 2D \left( \frac{4pn}{l} \right)^2 \sin^2 \left( \frac{q}{2} \right)$$

This relation has been used to test whether the experimental setup was adjusted adequately, and whether effects from multiple reflections and from any isotropy in the arrangement could be neglected. An example for a  $\Gamma$  versus  $\sin^2(\theta/2)$  relation reflecting the favorable measurement conditions is shown in Figure 4.2.

## 4.2 Data Treatment: SLS

Light scattering probes value of  $\bar{q}$ , such that  $\frac{1}{\bar{q}}$  ( $\sim 1000 \text{ \AA}$ ) is much greater than the size of ME droplets so that it is possible to ignore the  $\bar{q}$  dependence in excess scattering intensity. Therefore, the excess scattering intensity of the ME droplets over that of the continuous phase were analyzed according to Eq.(3.11) and (3.13) at given  $\bar{q}$ .

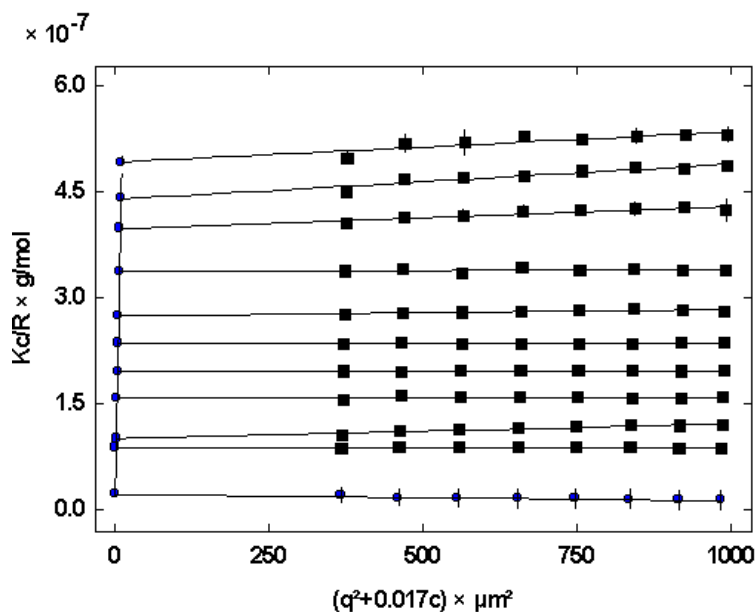


Figure 4.3 Zimm plot for AOT-Water-Heptane/Xylene ME.

Further more SLS data obtained from macromolecular solutions (size of droplets in the solution is at least  $1/20^{\text{th}}$  of the wavelength of incident light) at different angle as well as different concentration can also be analyzed by graphical technique firstly reported in a classical article by Zimm<sup>64</sup>. This technique involves simultaneously extrapolating light scattering data to both zero angle and zero concentrations. This can be achieved by plotting  $Kc/R_{\theta}$  vs.  $q^2 + (\text{constant } k)c$  as shown in Figure 4.3. Where arbitrary mathematical constant (lower case k) with no physical significance is chosen to give a convenient spacing of the data points on the graph. It is seen that the data points fall on a grid, producing two families of curves, one corresponding to constant concentration and the other to constant angle. Data analysis is based on the formula given in Eq. (3.16).

Flow chart shown below (Figure 4.4) describes the method for analyzing SLS data by graphical technique

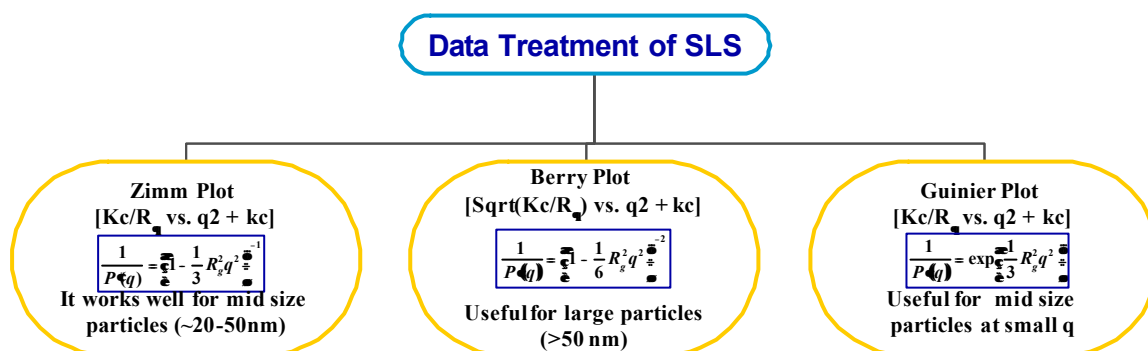


Figure 4.4 Classification of methods to analyze the SLS data

### 4.3 Data Treatment: DLS

An attempt to sort and regroup the DLS data analysis methods according to main features is presented in the flow chart given in Figure 4.5 and in the following discussion.

The treatment of the DLS relies on the assumptions that Siegert relation [Eq. (3.18)] is appropriate for conditions studied. This requirement is fulfilled in vast majority of cases. Cases in which the Siegert relation is violated include mainly three types of situation:

1. Experiments with a small number of particles in the scattering volume so that this number fluctuates substantially during one coherence time;<sup>65</sup>
2. Experiments with strongly interacting particles, where the non-Gaussian behavior is again due to number fluctuations, in this case caused by repulsive interactions;<sup>66</sup>
3. Scattering from non-ergodic systems, such as gels or glasses, where the time-averaged intensity correlation function of scattered light is different from the ensemble averaged function.<sup>67</sup>

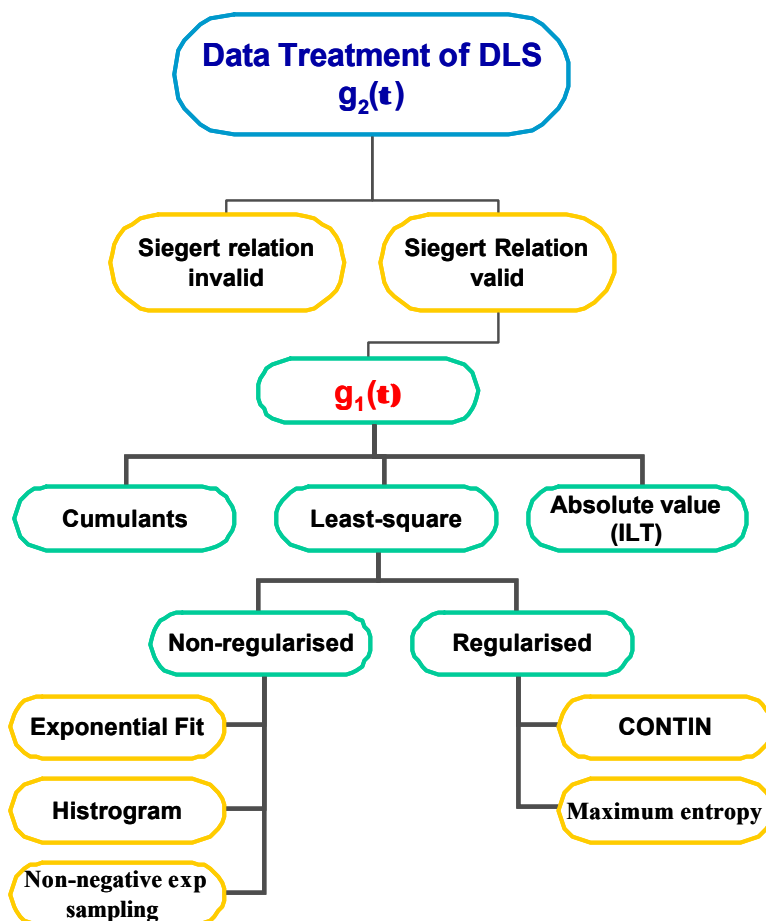


Figure 4.5 Classification of methods to analyze the DLS data.

Various approaches to the reliable estimation of  $G(\mathbf{G})$  needed to compute  $g_1(\mathbf{t})$  [see Eq. (3.30)] have been developed. One can estimate  $G(\mathbf{G})$  directly, by inverting the integral Eq. (3.30) with *inverse Laplace transform (ILT)*.<sup>68</sup> Unfortunately, this is a mathematically ill-conditioned problem which is not subjected to the usual criteria of goodness-of-fit: there exists an infinite set of distributions  $G(\mathbf{G})$ , which upon transformation, yield correlation functions which agree, within the inevitable experimental errors, with the measured data. Therefore, while this method is theoretically feasible, extremely precise data over extended ranges are required and even state-of-the art correlators have difficulty in satisfying the very demanding conditions for such successful inversions. Thus this technique has not been widely used.

Other approaches to the “inversion” of Eq. (3.30) are *least-squares* fitting procedure in which,

$$(4.4) \quad \mathbf{c}^2 = \left( \sum_m \left( \frac{1}{\mathbf{s}_m^2} \right) (g_1(\mathbf{t}) - w_m(\Gamma) e^{-\Gamma_m \mathbf{t}}) \right)^2$$

is minimized with respect to the variables  $w_m$  and  $\mathbf{G}_m$  or maximizing the entropy of the solution with a constraint on  $\mathbf{c}^2$  (where  $\mathbf{s}_m$  is standard error at point  $m$ ). In these approaches, either a specific size or molecular weight distribution function is preassumed, the corresponding

method thus called “parameter fit”<sup>69,70</sup>, or the specific distribution form is unknown, but some type of constraint on  $G(\mathbf{G})$  is imposed in order to achieve a unique solution.

**Non-Regularization Methods:** data analysis using *non-regularization* methods involve *exponential analysis* (1 Exp, 2 Exp and 3 Exp)<sup>71</sup>, *histogram analysis*<sup>72</sup> and *combined exponential sampling with non negative least square (NNLS) procedures*<sup>73,74</sup>. In this method  $w$ 's are restricted to be positive. The set of  $w$ 's obtained corresponds to the amplitudes or relative weights tied to each of the  $\mathbf{G}$  in the exponentials of Eq. (4.4). The amplitudes can be displayed in histogram form because each  $\Gamma$  has a corresponding particle size.<sup>75</sup>

**Regularization Methods (CONTIN & Maximum-Entropy Methods):** all constrained *regularization* methods<sup>76</sup> aim at inverting the Laplace transformation of Eq. (3.30), in general way not assuming any particular form of  $w(\mathbf{G})$ . In this method a solution of the Eq. (3.30) is obtained by minimizing the function

$$(4.5) \quad c^2 = \left( \sum_m \left( \frac{1}{s_m^2} \right) (g_1(t) - w_m(\Gamma) e^{-\Gamma_m t}) \right)^2 + \alpha \|\wp w(\Gamma)\|^2$$

with respect to the function  $w(\mathbf{G})$ . This objective function differs from the usual  $c^2$  parameter by the last term in Eq. (4.5);  $\alpha$  is called the regularization parameter and  $\wp$  is an operator which is usually taken to be the second derivative. The value of  $\alpha$  controls the strength of the regularization;  $\alpha = 0$  or very small value will be equivalent to be a bare non-negative least squares method, where as the larger  $\alpha$  is the more penalized are solutions with many peaks.

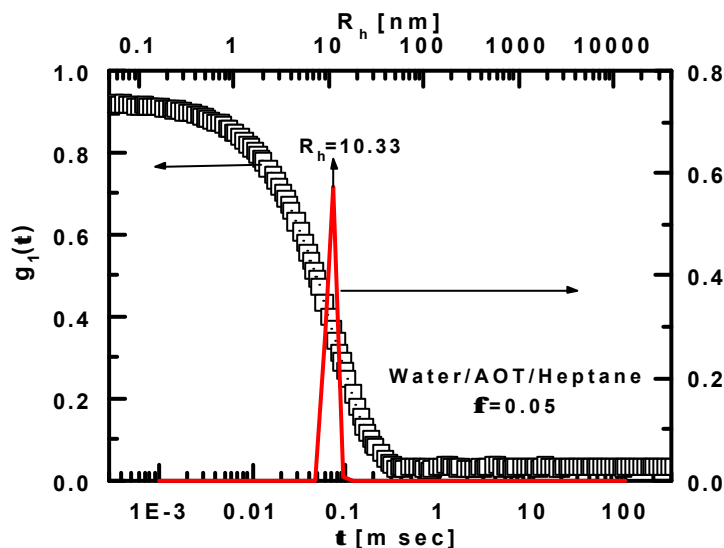


**Figure 4.6** Results of DLS data of -  $H_2O$  - AOT-n-heptane ME ( $\mu = 45$ ,  $f = 0.05$ ) using CONTIN fit. "Probability to Reject" = 0.5, used for Fisher F-test. Results obtained from fitting are discussed in the Chapter 5.

A very important issue is to select the value of  $\alpha$  properly. Provencher<sup>76</sup> used the Fisher F test, suitable when little is known about the solution or the errors. The Fisher F-test can be visualized for given a data *set 1* and a data *set 2* as follows: if the hypothesis is that both data sets are drawn from the same sample set, this hypothesis can be checked on the basis of the

variances  $V1$  and  $V2$  of these data sets. Fisher F-test uses these variances, the number of data points and the degrees of freedom in the data set to test this hypothesis and returns the probability to accept the hypothesis. Obviously,  $1 -$  this probability will give you the "Probability to Reject" the hypothesis. For a probability of 0.5, one accepts/rejects on the same level and this probability ensures the least residual information in the data is left. This method has been encoded in a very popular and widely used FORTRAN program package, *CONTIN* by Provencher.<sup>76</sup> Figure 4.6 shows one example of the data analysis using *CONTIN* method. *Maximum-entropy method* also aims at selecting a smooth solution to Eq. (4.5) but instead of using regularization parameter  $\alpha$ , it used  $-S$ , the entropy of the solution.<sup>77</sup> Detailed review of such special inversion methods has been given by Stock and Ray.<sup>78</sup>

**Cumulant Analysis:** another approach devised by Koppel<sup>79</sup>, is a very simple and widely used method for characterization of a reasonably narrow distribution without requiring a priori assumption on the form of the line width distribution function. This method, known as "cumulant expansion", is based on the formalism of the statistical cumulant generating function.  $g_1(q, \mathbf{t})$  is expanded as follows

$$(4.6) \quad \log_e g_1(q, \mathbf{t}) = \sum_{m=1}^{\infty} \Gamma_m \frac{(-\mathbf{t})^m}{m!}$$

where  $\Gamma_m$  is the  $m^{\text{th}}$  cumulant. The coefficients in this series describe some of the properties of the  $G(\mathbf{Q})$ .

The apparent diffusion coefficient  $D_{app}$  can be obtained from first cumulant

$$(4.7) \quad D_{app} = \frac{\Gamma_1}{q^2}$$

Another quantity, which is often used to specify the polydispersity,  $\mathbf{g}$  is the normalized variance defined as<sup>80</sup>

$$(4.8) \quad \mathbf{g}_a = \frac{\Gamma_2}{\Gamma_1^2}$$

whereas for other size distribution through algebra it can easily be shown that this simple relation will hold only when the distributions are very narrow.

In the case of log-normal size distribution, width of radius distribution  $\mathbf{s}_s$  can be related to experimentally determined  $\mathbf{g}$  as<sup>80</sup>

$$(4.9) \quad \mathbf{s}_s = \sqrt{\frac{R^2}{R^2} - 1} = \sqrt{\mathbf{g}_a}$$

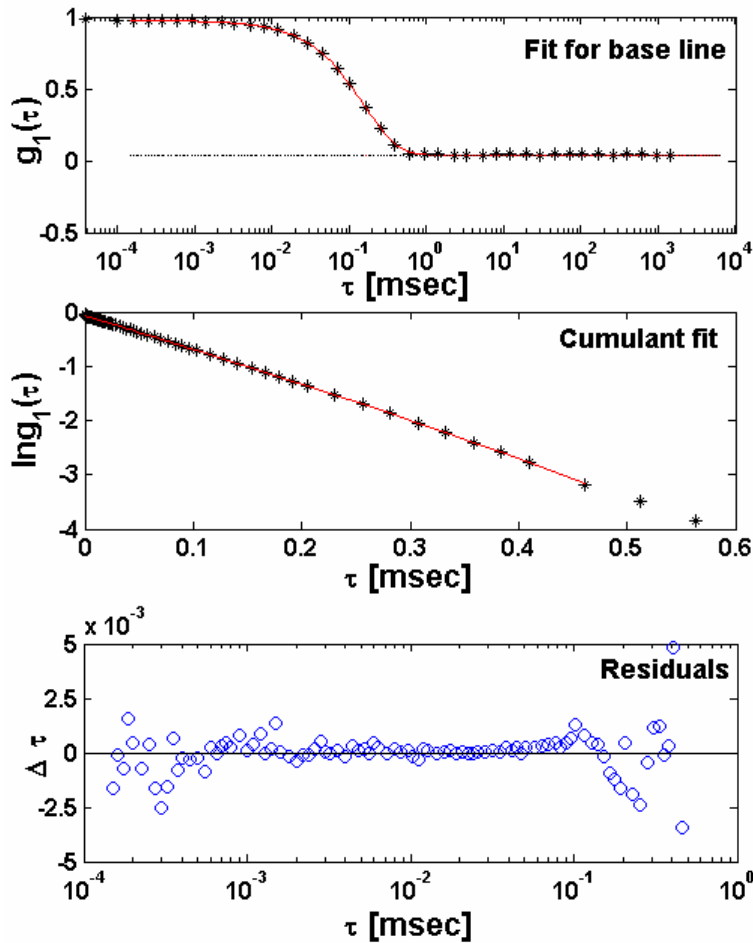


**Figure 4.7** Examples of DLS autocorrelation data obtained for ME in the Water/AOT/n-Nonane at  $\mu = 40$  and  $T = 22.5^\circ\text{C}$ . The autocorrelation data and single exponential fit are plotted in upper graph. The only 5th point of the autocorrelation data is plotted. Data and cumulant fit of order 3 are plotted in middle graph. The residuals (deviations of the experimental points from fitting line) are plotted on the lower graph. This shows no systematic error. The data were taken at scattering angle  $50^\circ$ .

Similarly,  $G_3$  and  $G_4$  are the measures of the skewness or asymmetry, and kurtosis or flatness of the distribution. In order to specify completely the distribution the cumulants of all orders are necessary. However, with the available precision of DLS data statistical significance can usually be given only to the first two or three order cumulants. High order cumulants beyond the third moment can not be determined precisely even using modern instrumentation in DLS. Nevertheless, the cumulant method is still a powerful technique for defining the gross characteristics of  $G(\mathbf{G})$ . The fitting procedure was the first to use model function

$$(4.10) \quad |g_1(\mathbf{t})| = A_0 + A_1 e^{-Dq^2 t}$$

to fit for a base line (base line  $A_0$  is due background scattering). Then base line estimate was subtracted from the data, logarithms of these data are then plotted as a function of the delay time  $\tau$  and it was refit by a polynomial  $A_1 - \Gamma_1 \tau + 1/2 \Gamma_2 \tau^2 - 1/6 \Gamma_3 \tau^3$  [Eq. (4.6)] from which first cumulant  $G_1$  second cumulant  $G_2$  and third cumulant was extracted  $G_3$ . Last correlation channel included in the fit for cumulant model if  $g(\tau) \geq$  baseline is valid. Residuals are calculated using equation  $\Delta \mathbf{t} = \ln(g_1(\mathbf{t}) - A_0) - \sum_{n=0}^j a_n t_i^n$ , where  $i$  the index of correlation channels,  $j$  the order of the polynomial fit and  $a_n$  the polynomial coefficients. Figure 4.7 shows

one example of how satisfactory the data analysis at low concentration is using this method. Some difficulties may exist in the interpretation of  $G(\mathbf{G})$  using this method. Firstly, the method is insensitive to a small degree of polydispersity. On the other hand, as polydispersity increases, the series expansion becomes valid only for small values of correlation delay times. Then, information on the correlation profile at larger delay times is not utilized. Secondly, when  $G(\mathbf{G})$  is bimodal (e.g., when two decay modes are present), difficulties can arise because of the slow convergence or even divergence of the cumulant expansion. Of the foregoing data analysis techniques, the method cumulant has been the simplest and most widely used so far.

**Two-Exponential Analysis:** for highly concentrated polydisperse, or strongly interacting system of colloidal particles, there will be two decay modes [see Eq. (3.42)]. The data for samples at high concentration could be fitted well by the *sum of two exponentials* (solid lines in Figure 4.8) whose decay constants were assumed to give the collective and self-diffusion coefficients  $D_c$  and  $D_s$ . For small, homogeneous hard spheres, size polydispersity  $\sigma_s$  and optical polydispersity  $\sigma_o$  can be deduced from relative amplitude of slower decay mode. In Figure 4.8 shows one example of how satisfactory the data analysis at high concentration is using two exponential. Inadequate cumulant best fit is also shown as broken line for higher concentration in Figure 4.8.

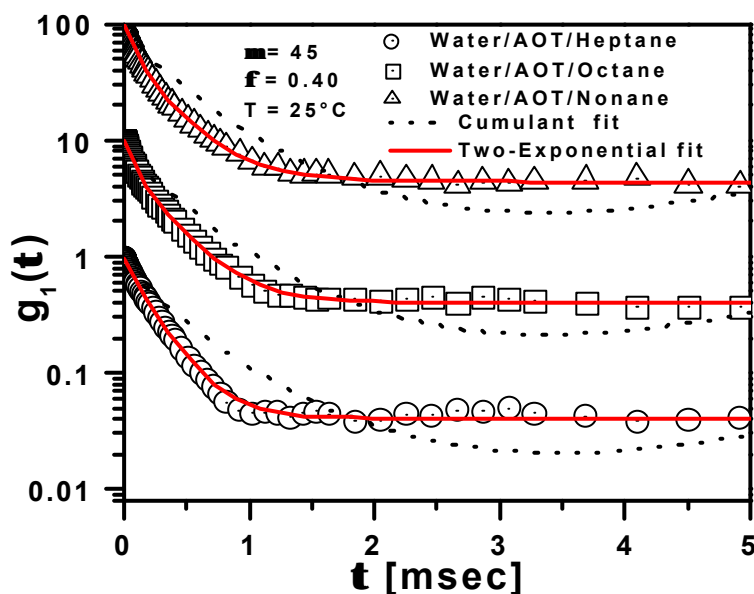


**Figure 4.8** DLS autocorrelation  $g_1(t)$  for the ME systems AOT/Water/*n*-Alkanes with  $f = 0.40$  at  $25^\circ\text{C}$ . A two exponential fit is plotted through the solid line. The inadequate cumulant best fit is shown as a broken line. The curves are shifted upward one unit with respect to previous one to avoid overlap.

#### 4.4 SANS: Data Acquisition and Treatment

The SANS measurements were carried out at the small-angle neutron spectrometer at the Hahn-Meitner-Institute, Berlin (BENS) and at the small angle scattering spectrometer YUMO at the Joint Institute for Nuclear Research Dubna, Russia. The pulsed neutron source IBR-2 at the Joint Institute for Nuclear Research delivers a spectra of thermal neutrons and the momentum transfer is calculated by time-of-flight methods with an averaged resolution of  $\sim$

0.10 ( $\Delta q/q$ ). The spectrometer is equipped with the circular multiwire proportional  $^3\text{He}$  detectors.<sup>81</sup>

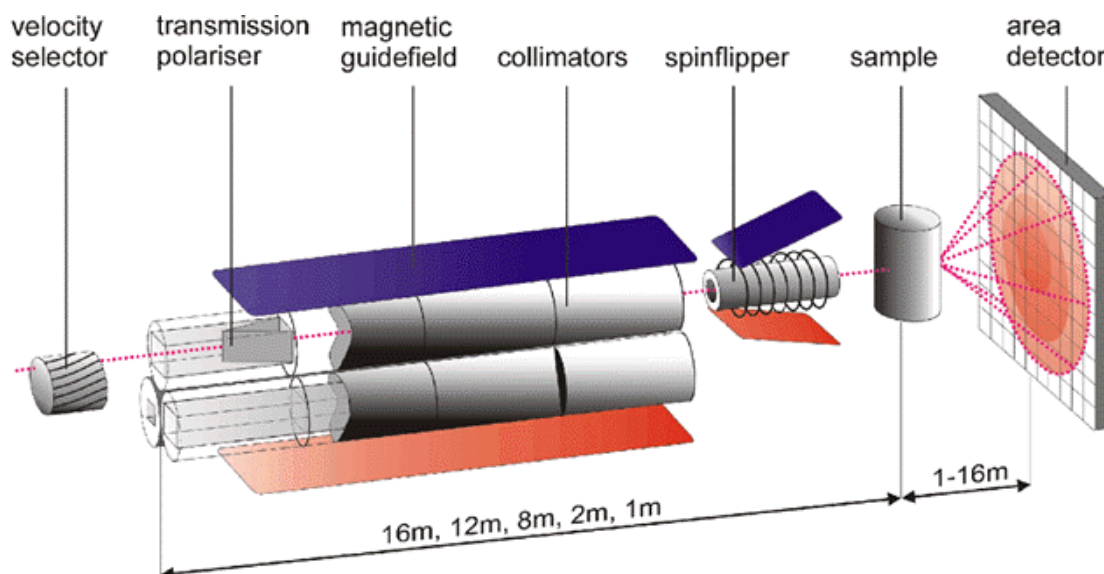


**Figure 4.9** SANS Apparatus V4 at the Hahn-Meitner-Institute, Berlin (BENSCH).

Small-angle neutron spectrometer at the Hahn-Meitner-Institute, Berlin (BENSCH) is shown in Figure 4.9. At the small-angle neutron spectrometer (V4) at BENSCH, incoming neutrons are monochromatized by a mechanical velocity selector with variable wavelengths from 0.38 nm to 3 nm. The two-dimensional  $^3\text{He}$ -detector with  $64 \times 64$  elements of  $10 \times 10 \text{ mm}^2$ ; can be positioned at any distance between 1 and 16 m from the sample in the horizontal direction. Additionally, at 1 m distance the detector can be moved vertically by 0.3 m extending the  $\vec{q}$  range to higher values. One can also adjust collimation range of incoming neutrons at five different lengths (1m, 2m, 8m, 12m and 16m) of the collimation as shown in Figure 4.9. A large sample chamber is connected to a vacuum system with the detector and collimator tubes. It can be equipped with a temperature controlled sample changer ( $5^\circ\text{C} - 80^\circ\text{C}$ ), electromagnet (2 T) with sample changer or heatable sample stick ( $600^\circ\text{C}$ ), a high temperature furnace ( $1800^\circ\text{C}$ ). The instrument is fully controlled via CAMAC by an ALPHA workstation using the instrument control program CARESS. Polarized neutrons are now available at the instrument. A high-transmission supermirror polarizer can be introduced by remote control in front of the 12 m collimation without any modification of the instrument alignment. The polarization direction can be reversed by a RF gradient spin-flipper in front of the sample. The SANSPOLE option is characterized by a high neutron flux of more than 30% of the non-polarized beam, a high degree of polarization ( $> 90\%$ ) and high efficiency of the spin-flipper ( $> 95\%$ ) for  $\lambda < 1.8 \text{ nm}$  without any additional background. The samples were poured into quartz cells (Hellma, Muellheim, Germany), which have a path length of 2 mm.

Following measurements are required for SANS experiment:



(e.g., two-dimensional  $^3\text{He}$ -detector with  $64 \times 64$  cells used at BENSC Berlin), one has to correct the data cell by cell. The intensity measured in a particular cell  $(i,j)$  of the 2D multi detector is first corrected for detector dead time  $t$  according to the formula

$$(4.11) \quad I_{ij\text{-corrected}} = \frac{I_{ij\text{-measured}}}{1 - \frac{t}{T} \sum_{i,j} I_{ij\text{-measured}}}.$$

In this equation,  $i$  represents each of the input types for scattering data and  $t$  is the total measurement time used for the appropriate input data type. The detector deadtime  $\tau$  had been experimentally determined.

After this correction, the number of detected neutrons at cell  $(i,j)$ ,  $I_{ij\text{-corrected}}$ , must be first normalized  $\bar{I}_{ij\text{-corrected}}$  to a given individual monitor values recorded in the measured data files and then corrected for the electronic noise background (Cd) and sample background (SB) according to the formula

$$(4.12) \quad \bar{I}_{i,j\text{-corrected}} = \frac{\bar{I}_{ij\text{-corrected}}^S - \bar{I}_{ij\text{-corrected}}^{Cd}}{T^S} - \frac{\bar{I}_{ij\text{-corrected}}^{SB} - \bar{I}_{ij\text{-corrected}}^{Cd}}{T^{SB}}.$$

The next step is to obtain the differential cross-section from these corrected intensities  $\bar{I}_{ij\text{-corrected}}$ . One usually uses water as an absolute standard to calibrate the detector. Water is nearly a completely incoherent scatterer, and one expects the single scattering intensity to be isotropically distributed in the forward direction. If one further assumes that the multiple scattered intensities are also isotropically distributed in the forward direction, then one can simply obtain the scattering cross-section of the water specimen by a transmission measurement. The absolute coherent scattering cross-section  $\frac{d\Sigma}{d\Omega}$  of the sample is given by<sup>33</sup>

$$(4.13) \quad \left( \frac{d\Sigma}{d\Omega} \right)_{i,j} = \frac{\bar{I}_{ij\text{-corrected}}}{\frac{\bar{I}_{ij\text{-corrected}}^W - \bar{I}_{ij\text{-corrected}}^{Cd}}{T^W} - \frac{\bar{I}_{ij\text{-corrected}}^{WB} - \bar{I}_{ij\text{-corrected}}^{Cd}}{T^{WB}}} \times \frac{SFW}{SFS} - \frac{\Sigma_{inc}}{4p}.$$

$\frac{\Sigma_{inc}}{4p}$  is the incoherent scattering contribution of samples. SFW and SFS represent the scaling factor for water and sample, respectively.  $T$  represents the transmission of these input data types. Sample transmission  $T_S$  is calculated from the total sum of the corrected and normalized intensities of all detector cells of the input types of transmission data according to the formula

$$(4.14) \quad T_S = \frac{\bar{I}_{corrected}^S - \bar{I}_{corrected}^{Cd}}{\bar{I}_{corrected}^{EH} - \bar{I}_{corrected}^{Cd}}.$$

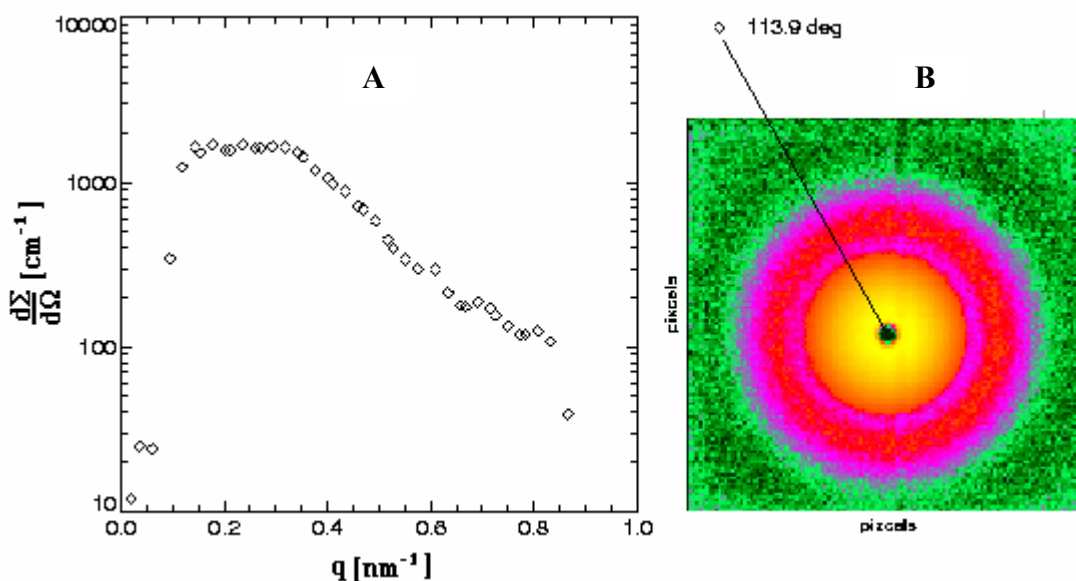


Figure 4.11 A typical SANS patterns: (A) 2D spectra, (B) 1D spectra.

A typical SANS pattern of 2D detector resulting from Eq. (4.13) is shown in Figure 4.11A. Radial average of 2D patterns gives SANS spectra as shown in Figure 4.11B too. As described in the Section 3.4, these SANS spectra can be analyzed according to Guinier relation, Porod relation or fitting of the data consists to compare the theoretical  $P(\vec{q})$  and  $S(\vec{q})$  to the real data. A typical fit of SANS spectra for polydisperse core shell sphere model for the form factor  $F(\vec{q})$  and PY hard sphere potential model for the structure factor is shown in Figure 4.12.  $F(\vec{q})$  is integrated during the fitting procedure over a Schultz distribution function to get the polydispersity  $\sigma_s$  concerning the overall size  $R_{\text{shell}}$ .<sup>51</sup>

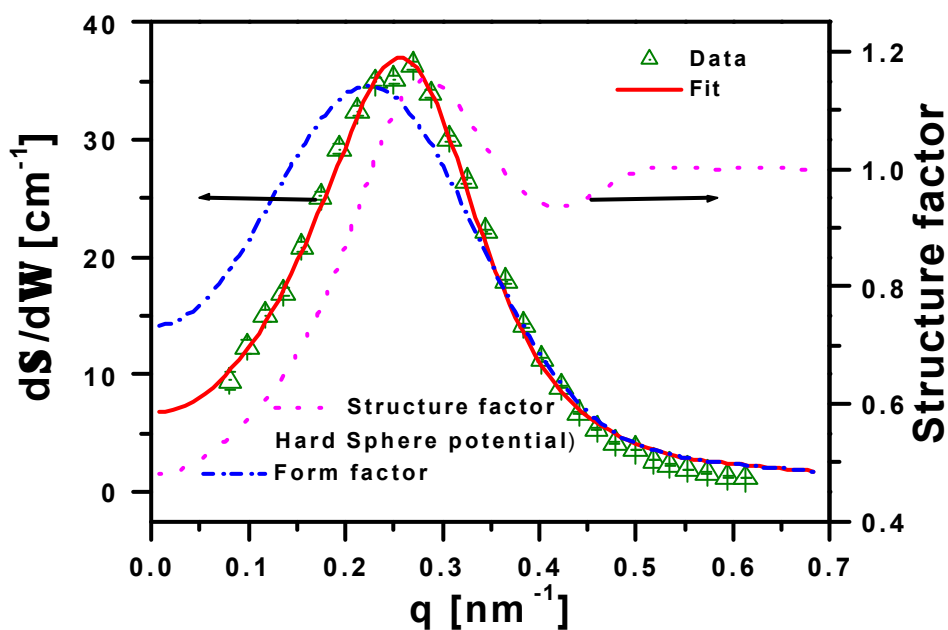


Figure 4.12 SANS curve (points) from O/W - ME (Eutanol-Tagat<sup>®</sup> O2 /Poloxamer 331 - water/PG) and theoretically predicted curve (line). Results obtained from fitting are discussed in the Chapter 5.

## 5 Results and Discussion

Our interest is focused especially on the shape and size of ME droplets, which are expected to be a function of interdroplet interaction. Scattering techniques were used to extract the above mentioned informations. In some cases, three complementary techniques (SLS, DLS and SANS) were used to compare and get more detailed description of our results. This chapter is primarily divided into three parts.

- In the first part, model ternary AOT-MEs were investigated. This system is chosen because it has a relatively wide range of one-phase ME regions at room temperature without a fourth element such as a cosurfactant or brine (instead of water). This enables a rather simple interpretation of the experimental results and a direct comparison with existing theory. Size growth and size fluctuations of system have been precisely estimated by contrast variation experiments. And dilution procedure was used to extract information about droplet size, diffusion coefficient, interaction and polydispersities (both optical and size) from experimental data.
- In second part, MEs of pharmaceutical interest derived in our group were characterized. We proposed interaction potential for these MEs stabilized by non ionic surfactants. From this interaction potential, parameters describing stability of our systems have been calculated which are consistent with observed stability of our systems. Effect of concentration of each constituent solubilized in MEs on droplet size and stability was also estimated.
- In the third part, effect of concentration of each constituent solubilized in O/W MEs in which local anesthetics (drug) are in oil form on droplet size was investigated. Effect of pH on stability of these MEs was also estimated.

### 5.1 Water / AOT / *n*- Alkanes MEs

Water-in-oil MEs can solubilize hydrophilic guest molecules such as ions,<sup>82</sup> enzymes, or synthetic polymers, which would otherwise have only limited or no solubility at all in the organic solvent.<sup>83</sup> This property makes MEs very interesting model systems for both basic research as well as an increasing number of applications such as drug delivery, enzymatically catalyzed organic-phase synthesis, cosmetics, enhanced oil recovery etc.<sup>82,21,22,23,24</sup> Physics of these systems is very diverse, but in all cases a detailed description of the structure is very important to correctly interpret the observed phenomena and to develop good theoretical models of the driving forces responsible for both droplet formation and solubilization of guest molecules in MEs.<sup>84</sup> The W/O - ME systems studied were water/AOT/*n*-alkanes systems (see

Figure 5.1) due to its ability to solubilize<sup>85</sup> large amount of polar solvent (typically water) in apolar solvents without need for a stabilizing cosurfactant.<sup>86,87</sup> AOT can form reverse micelles both in the presence and in the absence of solubilized water. However if the medium is completely water free, there is no well defined critical micellar concentration, and the aggregates formed are very small and polydisperse.<sup>88,89</sup> Close packing of the surfactant polar heads leaves an empty volume in the centre of the micellar core, which can only be filled with hydration (or bound) water. This explains why the presence of water is necessary to form a large surfactant aggregate. We will study the properties of large and well defined micelles formed when water is present. The “surfactant packing parameter  $v_s/a_s L$ ” introduced in the Section 1.4, gives a good idea of the shape of the aggregates which will be formed spontaneously. Let us estimate now  $v_s/a_s L$  for AOT:  $v_s \sim 650 \text{ \AA}^3$ ,  $L \sim 9 \text{ \AA}$  and  $a_s \sim 50 \text{ \AA}^2$  gives<sup>82</sup>  $v_s/a_s L > 1$ . This indicates that W/O - ME is favored. The reverse micelles considered here then W/O - MEs.

### 5.1.1 Layered Sphere Model

For the interpretation of our results, a model for microemulsion droplet is needed. A ME droplet modeled as a layered dielectric sphere (see Figure 5.1),<sup>90,91</sup> considered as made of a water core of radius  $R_{core}$ , surrounded by a penetrable shell of thickness  $L$  consisting nonpolar tails of the AOT molecules. The hydrodynamic radius is thus  $R_h = R_{core} + L$ . The AOT is assumed to be entirely at the interface with only a negligible concentration of free molecules in the oil phase. A layered sphere droplet model of W/O - ME and profile of dielectric constant:  $\epsilon_w$  indicates dielectric constant of water,  $\epsilon_s$  indicates dielectric constant of surfactant and  $\epsilon_o$  indicates dielectric constant of oil is presented in Figure 5.1. In this layered spherical model, the MEs are considered as a priori formed objects: the water core and surfactant film form a single entity, immersed in a continuous oil phase. Therefore, the volume fraction ( $\phi$ ) of the ME droplets can be defined as

$$(5.1) \quad \mathbf{f} = \mathbf{f}_w + \mathbf{f}_{AOT}$$

The size of MEs stabilized by AOT is highly dependent on the concentration of each constituent;<sup>85</sup> however, it is recognized that the aggregate size is typically characterized by the molar water to AOT ratio  $\mu$  rather than the actual concentration.<sup>85</sup>

Let us define

$$(5.2) \quad \mathbf{m} = \frac{[H_2O]}{[AOT]} = \frac{\Theta M_{AOT}}{\Xi M_{H_2O}}$$

where,  $Q$  is weight percentage of water,  $M_{H_2O} = 18.02$  g/mol (molecular weight of water) and  $\Xi$  is weight percentage of AOT,  $M_{AOT} = 444.57$  g/mol (molecular weight of AOT).

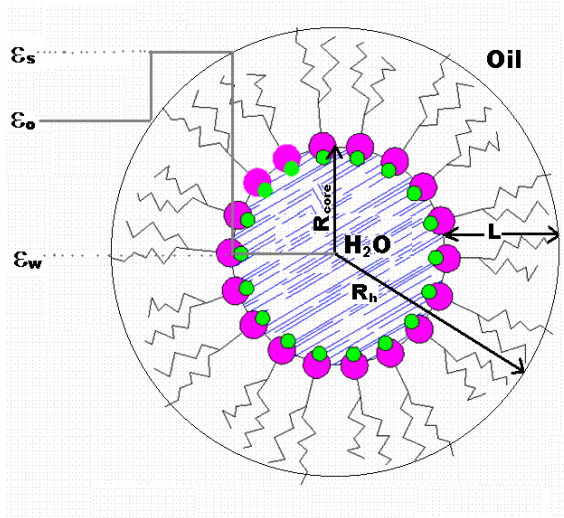
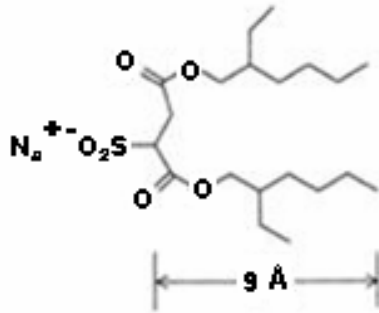


**Figure 5.1** Layered dielectric sphere droplet model of W/O – ME is shown in upper figure (see text for details). The structure of AOT molecule is shown in lower figure.



Using the simple geometry of Figure 5.1, one can write

$$(5.3) \quad V = V_{core} + V_{shell}$$

where,  $V_{core}$  is the volume of core and  $V_{shell}$  is the volume of surfactant layer.

We note

$$(5.4) \quad V_{core} = \frac{4\mathbf{p}}{3} \langle R_{core}^3 \rangle, \quad \text{and} \quad A_{core} = 4\mathbf{p} \langle R_{core}^2 \rangle$$

The angular bracket denote the average

$$(5.5) \quad \langle \dots \rangle \propto \int f(r) \dots d(r)$$

where  $f(r)$  is the size distribution function of ME droplets. For our calculations we used a Schulz size distribution.

So that dividing both sides of Eq. (5.3) by  $A_{core}$  gives

$$(5.6) \quad \frac{1}{3} \frac{\langle R_{core}^3 \rangle}{\langle R_{core}^2 \rangle} = \frac{V_{core}}{A_{core}} = \frac{v_w}{a_s} \mathbf{m}$$

Using recursive formula relating the moments for Schulz size distribution given in Eq. (B.9), one can get

$$(5.7) \quad \mathbf{y}(\mathbf{s}_s) \langle R_{core} \rangle = 3 \frac{v_w}{a_s} \mathbf{m}$$

where prefactor  $\mathbf{y}(\mathbf{s}_s)$  depends on size distribution parameter  $\mathbf{s}_s$ .  $\mathbf{y}(\mathbf{s}_s) = 1$  for monodisperse droplets and  $\mathbf{y}(\mathbf{s}_s) = 1 + 2 \mathbf{s}_s^2$  for a Schulz size distribution (polydisperse droplets). In order to simplify the notation of subsequent formula, we have chosen parameter  $\gamma$ , which is related to the polydispersity index (relative standard deviation) as

$$\mathbf{s}_s = \sqrt{\mathbf{g}} = \sqrt{\frac{\langle R^2 \rangle - \langle R \rangle^2}{\langle R \rangle^2}}$$

Using the simple picture in Figure 5.1, one derives for the hydrodynamic radius  $R_h$  of an individual droplet as

$$(5.8) \quad R_h = R_{core} + L$$

where  $L$  is the thickness of the surfactant monolayer, including possible solvent molecules which migrate with the droplet.

In this study, we focused on two aspects of ME formation. First we varied the  $\mu$  ranging from 5 to 60 and keeping the *water weight percentage*  $\mathbf{Q}$  constant at 5% in order to vary the optical contrast of droplets (*Optical Contrast Variation*). Size and polydispersity of the ME droplets were determined with very high precision using optical contrast variation experiment because polydispersity influences the characteristic features of scattering data as well as the hydrodynamic radius with the molar ratio  $\mu$ . In the second step, we varied the water weight ratio in the range  $2\% < \Theta < 39\%$  and keeping the  $\mu$  constant at 45 in order to preserve a constant droplet radius (*Dilution*). DLS studies on concentration dependence of diffusion coefficient allow to determine the virial coefficient of diffusion and the hydrodynamic radius of ME droplets. Several theories relate this virial coefficient to interdroplet interaction.<sup>92,93,94</sup>

W/O - ME Compositions	Contrast Variation			Dilution Procedure			Temperature Dependent		
	$\mu$	$\mathbf{Q}$ [%]	T[°C]	$\mu$	$\mathbf{Q}$ [%]	T[°C]	$\mu$	$\mathbf{Q}$ [%]	T[°C]
<i>n</i> -heptane	5 to <b>60</b>	5	25	45	2 to 39	25	50 & 60	5	25 to 37.5
<i>n</i> -octane	10 to <b>55</b>	5	25	45	2 to 39	25	45 & 55	5	25 to 37.5
<i>n</i> -nonane	5 to <b>50</b>	5	25	45	2 to 39	25	30 & 40	5	25 to 37.5

**Table 5.1** Composition of the W/O - MEs ( $\mu$  is molar water to surfactant ratio and  $\Theta$  is weight percentage of water).

Hydrodynamic radius, and interdroplet interactions have been deduced from dilution procedure. The microstructure of MEs critically depends on the composition, temperature, and additives.<sup>95,96</sup> We know, ME (stable) droplets can be smaller than droplets of a macroemulsion (metastable) in a given surfactant-water-oil system, but the oil water interface in a ME is not under the kind of tension often present in a macroemulsion droplet. Thus depending on the conditions, a nonspherical droplet may be the thermodynamically stable shape in MEs. Therefore, these systems investigated at different compositions and temperatures in the range  $25^{\circ}\text{C} < T < 37.5^{\circ}\text{C}$ . Chain length of the *n*-alkane has been varied in order to show the dependence of some general features of systems on chain length of *n*-alkane ( $n = 7, 8$  and  $9$ ). The compositions of the MEs used are summarized in Table 5.1. All samples were prepared below the percolation threshold  $\phi \sim 0.55$  predicted for water/AOT/*n*-alkane MEs at  $T=25^{\circ}\text{C}$ .<sup>97</sup> All samples were analyzed in the single-phase ME, normally denoted as  $L_2$  phase (Lower phase separation or solubilization temperature  $T_l = 22.2^{\circ}\text{C}$ ,  $17.3^{\circ}\text{C}$  and  $14.5^{\circ}\text{C}$  and upper phase separation temperature  $T_u = 62.4^{\circ}\text{C}$ ,  $55.3^{\circ}\text{C}$  and  $47.3^{\circ}\text{C}$  for ME droplets in *n*-heptane, *n*-octane and *n*-nonane respectively).<sup>98, 99</sup>

Refractive index  $n$  (or optical dielectric constants  $\epsilon = n^2$ ), molecular volumes  $v$  and mass densities  $\rho$  at temperature  $25^{\circ}\text{C}$  used for the sample preparation as well as for the mathematical modeling of the ME systems are given in Table 5.2 (in the subsequent formula subscript  $s$  refers surfactant (AOT), subscript  $w$  refers water and subscript  $oil$  refers *n*-alkanes). For this work, curvature-dependent area per AOT molecule  $a_s$  at the interface is used<sup>82</sup>

$$(5.9) \quad a_s [\text{\AA}^2] = a_0 - 11 \times \exp[-0.0963(\mu - 10)]$$

where  $a_0$  is constant for AOT in different solvent.

	$n$	$\rho$ [g/cm <sup>3</sup> ]	$v$ [Å <sup>3</sup> ]
AOT	1.4850	1.127	648
H <sub>2</sub> O	1.3280	0.997	29.9
<i>n</i> -heptane	1.3851	0.683	-
<i>n</i> -octane	1.3951	0.703	-
<i>n</i> -nonane	1.4050	0.718	-

- parameter not used

**Table 5.2** Refractive indices ( $n$ ), mass densities ( $\rho$ ), and molecular volumes ( $v$ )

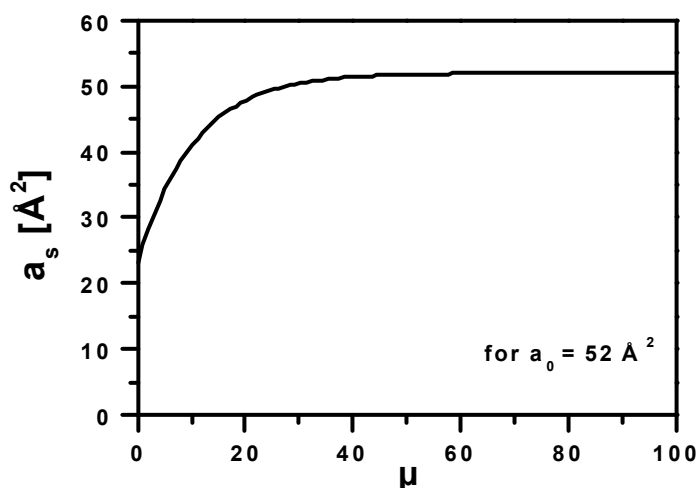


**Figure 5.2**  $\mu$  dependent area  $a_s$  per AOT molecule at interface.

## 5.1.2 Droplet size and polydispersity

A W/O - ME droplet has water core surrounded by a shell of surfactant (AOT). Contrast variation light scattering experiments exploits the fact that, since water and AOT have different refractive indices (or dielectric constant) for water ( $\epsilon_w$ ) and AOT ( $\epsilon_s$ ), the optical contrast of the ME droplets changes with  $\mu$  (see Table 5.1). The  $n$ -alkanes used for the study have dielectric constants ( $\epsilon_o$ ) that lie between those of water and AOT. It is therefore possible to combine water and AOT in such a proportions that the average dielectric constant of water plus AOT is the same as that of the  $n$ -alkane used. At this point, which is normally referred as the optical matching point, resulting excess polarizability goes through zero [see Eq.(3.14)]. For this particular composition of water and AOT the droplets become “invisible” in a light scattering experiment. This is illustrated in Figure 5.3, where the optical excess polarizability  $\alpha_{\text{excess}}$  [see Eq.(3.14)] is plotted as a function of  $\mu$ . It can be seen from the Figure 5.3 that for a particular composition of water and AOT (that is for particular  $\mu$ ), resulting excess polarizability goes through zero. Figure 5.3 also shows that the location of this optical matching point (i.e.,  $\alpha_{\text{excess}} = 0$ ) can be shifted by changing the solvent in the ME because of the strong dependence of  $\alpha_{\text{excess}}$  on the dielectric constant of solvent  $\epsilon_o$  (low  $\epsilon_o$  value leads to a matching point at high  $\mu$ ; see Figure 5.3). We have chosen three  $n$ -alkanes ( $n = 7, 8$  and  $9$ ). We investigated the quantitative applicability of the layered sphere model for the description of the optical and geometrical properties of MEs ( $\Theta = 5\%$ ). We compare theoretical prediction of the optical and geometrical properties of the model with the following data:

- I. Refractive index increment,
- II. DLS and SANS (Hydrodynamic, gyration radii and apparent polydispersity as obtained from the first and second cumulant) and
- III. SLS (Averaged scattering intensity).

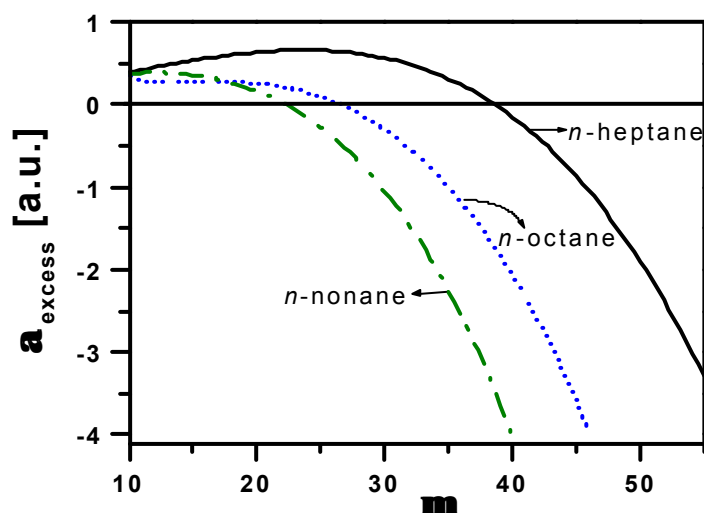


**Figure 5.3** Molar ratio  $\mu = [H_2O]/[AOT]$  dependence of the optical excess polarizability  $\langle a \rangle$  of W/O - ME droplet in the systems water/AOT/ $n$ -alkane from Eq.(3.14) and parameters given in the text.

This allows us to measure the polydispersity very precisely.<sup>100,91,84</sup> This will be illustrated with experiments using W/O - MEs having *n*-heptane, *n*-octane and *n*-nonane as continuous phase. The composition of the MEs used is summarized in Table 5.1 under the heading “contrast variation”.

### 5.1.2.1 Refractive Index Increment

The measurable quantity, refractive index increment  $\frac{\Delta n}{\Delta f}$  of the dispersion with respect to the pure oil is related to the average excess polarizability  $\langle \alpha \rangle_{\text{excess}}$  as<sup>33,91</sup>

$$(5.10) \quad \frac{\Delta n}{\Delta f} = \frac{1}{2\sqrt{\epsilon_{oil}}} \frac{\langle \mathbf{a} \rangle_{\text{excess}}}{\langle v_d \rangle} = \frac{w}{2\sqrt{\epsilon_o}} \frac{\frac{m}{y} + n}{\frac{m}{y} + 1}$$

with

$$w = 3\epsilon_{oil}\epsilon_w, \quad n = \frac{E_s}{E_w} \quad \text{and} \quad y = \frac{v_s}{v_w}$$

Note that all involved quantity in Eq. (5.10) can be determined from independent measurements. Experimental data are fitted with different values of parameter  $v_s$  (548, 648 and 748  $\text{\AA}^3$ ) because of large range of  $v_s$  values reported in the literature.

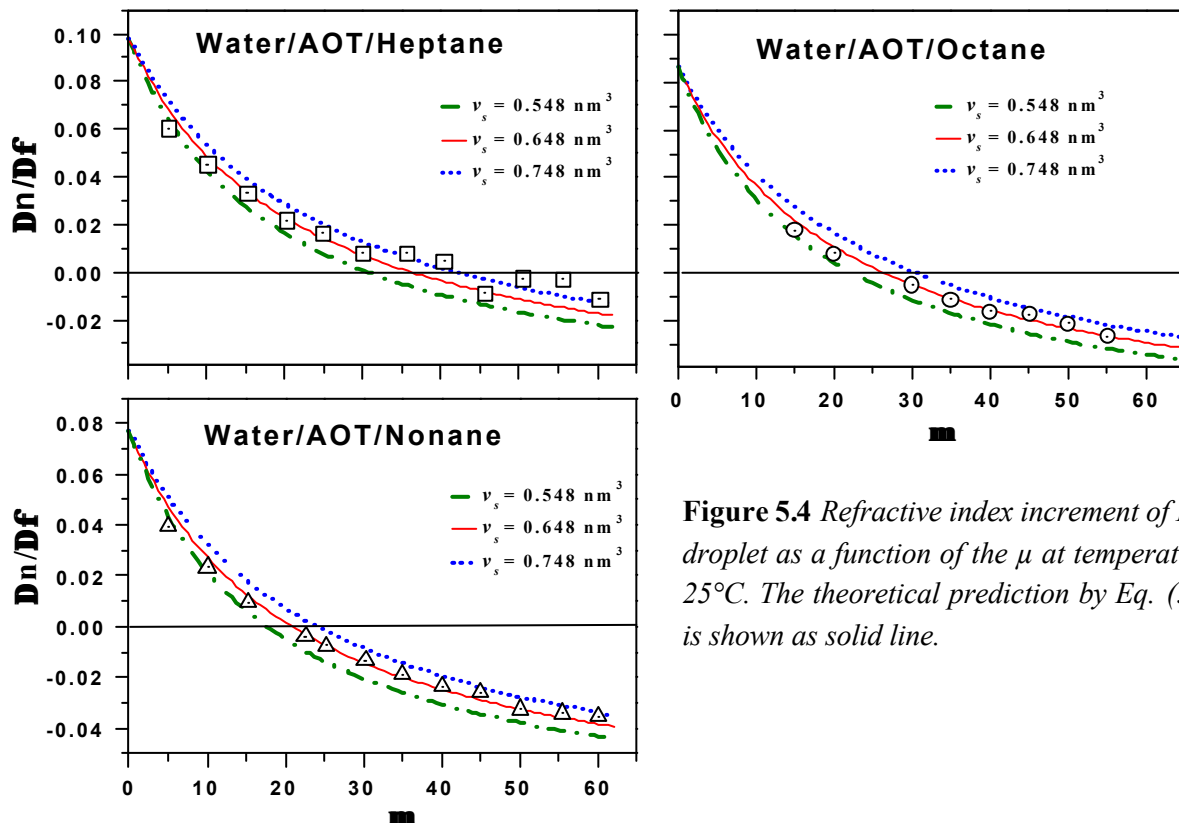


**Figure 5.4** Refractive index increment of ME droplet as a function of the  $\mu$  at temperature 25°C. The theoretical prediction by Eq. (5.8) is shown as solid line.

As shown in Figure 5.4, the agreement between the values theoretically predicted by Eq. (5.8) with  $v_s = 648 \text{ \AA}^3$  (shown by solid lines) and experimentally measured values is very good. In particular the predicted optical matching point i.e.,  $\Delta n / \Delta \mathbf{f} = 0$ , are close to the experimentally observed optical matching point. The  $v_s = 648 \text{ \AA}^3$  is same as used in reference 100. The values of  $\mu$  at which optical matching point occur for different  $n$ -alkanes are listed in Table 5.3.

### 5.1.2.2 DLS Results

For each sample, measurements (the average scattered intensity  $I$  and the intensity correlation function  $g_2(\tau)$ ) were performed at different scattering angles between  $50^\circ$ ,  $55^\circ$  and  $60^\circ$  at temperature  $25^\circ\text{C}$ . The intensity of the scattered light  $I$  and  $g_2(\tau)$  corresponding one set of experimental parameters have been measured five times and data used for fitting are averaged over these five measurements. Field auto correlation function  $g(\tau)$  derived from  $g_2(\tau)$  using Eq. (3.18) were fitted by a third order cumulant expansion [see Eq. (4.6)] from which first cumulant  $\Gamma_1$  second cumulant  $\Gamma_2$  and third cumulant  $\Gamma_3$  were extracted (fitting procedure was discussed in detail in the Section 4.3). The apparent diffusion coefficient has been deduced from first cumulant  $\Gamma_1$  [see Eq. (4.7)]. The second cumulant  $\Gamma_2$  is very sensitive to the correct value of the baseline  $A_0$  because of the high correlation between them. Polydispersity index  $\gamma_a$  calculated from second cumulant [see Eq. (4.8) and (4.9)] was  $\sim 0.1$  for all samples. As already pointed out by several authors<sup>45,84,91</sup> that the second cumulant  $\Gamma_2$  (represents only small correction to the shape of the correlation function) overestimate the polydispersity of ME droplets. To get the free diffusion coefficients of droplets  $D_0$ ,  $D_{app}$  is extrapolated to  $\phi \rightarrow 0$ .<sup>8</sup> Hydrodynamic radius was calculated from  $D_0$  using Eq. (3.44). Initial studies indicated that the MEs were too small to exhibit significant angular dependence; therefore results used for the discussion are the average of the results obtained at three different angles. Mean hydrodynamic radius  $\langle R_h \rangle$  as a function of molar water to AOT ratio  $\mu$  is plotted in Figure 5.5. These results are consistent with that  $\langle R_h \rangle$  varies linearly with  $\mu$  (except in the vicinity of optical matching point) shown by an array of different techniques.<sup>101,102,103,104,105,106</sup> As shown in the Figure 5.5, sigmoidal shape of  $R_h$  in the vicinity of optical matching point versus  $\mu$  reflects the polydispersity of MEs. Optical contrast variation experiments not only allow for a structural characterization of MEs, they also permit a precise determination of polydispersity of the droplet like ME particles. Position of the optical matching point and sigmoidal shape of  $R_h$  can be fit using expression in terms of  $\gamma$  given below<sup>91</sup>

$$(5.11) \quad \langle R_h \rangle = \frac{\langle a^2 \rangle}{\langle a^2 / R_h \rangle} = 3L \frac{m1 + 3g}{y 1 + 2g} \frac{A}{B - \left(\frac{2}{9}\right) \left(\frac{y}{m}\right) C}$$

with,

$$A = \frac{(1 + 5g)(1 + 4g)}{(1 + 2g)(1 + 2g)} \left(\frac{m}{y}\right)^2 + 2n \frac{(1 + 4g)}{(1 + 2g)} \left(\frac{m}{y}\right) + n^2,$$

$$B = \frac{(1+4g)(1+3g)}{(1+2g)(1+2g)} \left( \frac{m}{y} \right)^2 + 2n \frac{(1+3g)}{(1+2g)} \left( \frac{m}{y} \right) + n^2 \quad \text{and} \quad C = \frac{(1+3g)}{(1+2g)} \left( \frac{m}{y} \right)^2 + 2n \left( \frac{m}{y} \right) + n^2$$

where,  $R_h$  is the hydrodynamic radius of an individual droplet.

Note that Eq. (5.11) has only two adjustable parameters  $\gamma$  and  $a_0$  to fit the experimental data. For monodisperse droplets, Eq. (5.11) leads to an almost linear dependence of  $R_h$  on  $\mu$ . (see Figure 5.5 A,  $\gamma=0$ ). However for polydisperse solutions, the incomplete optical matching near the matching point due to polydispersity results in a sigmoidal shape of  $R_h$  versus  $\mu$ , which depends on the polydispersity index  $\gamma$  only.

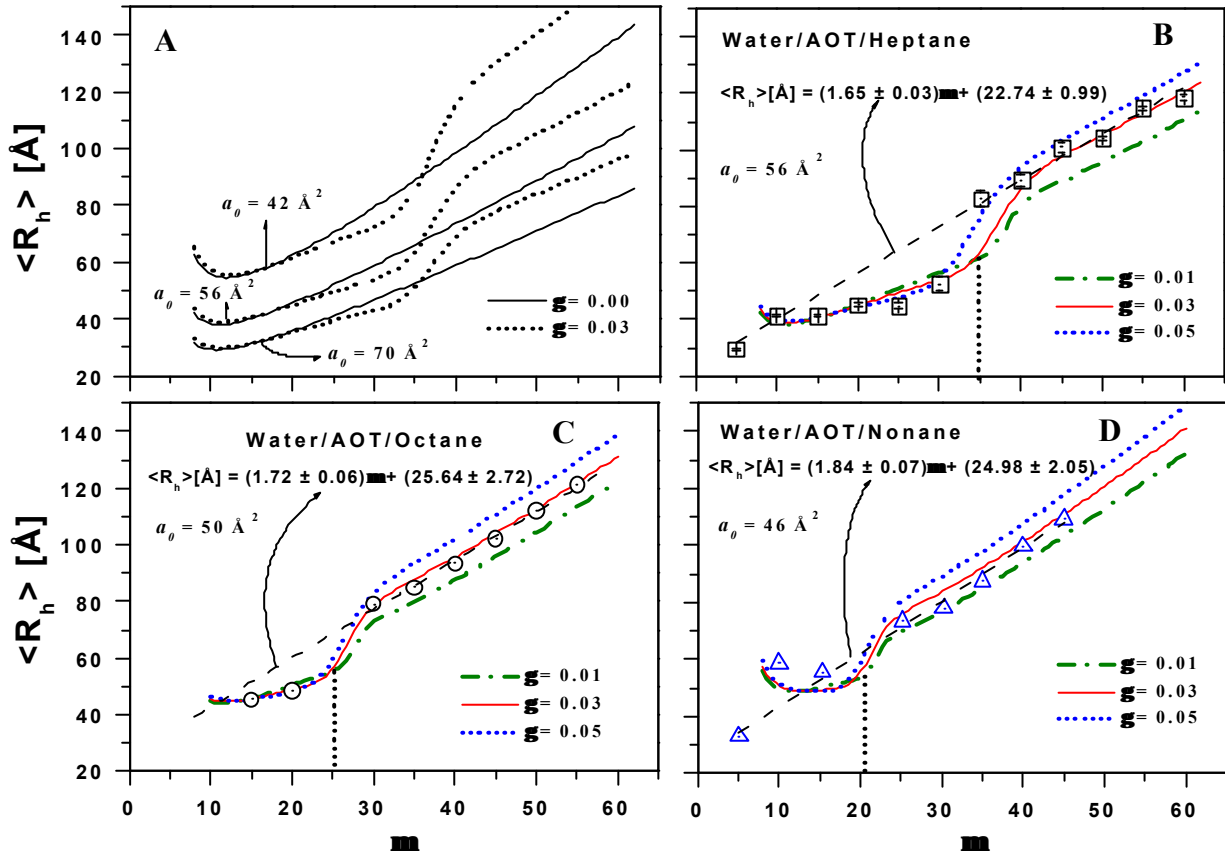


**Figure 5.5** Mean hydrodynamic radius  $\langle R_h \rangle$  of ME droplet as a function of the  $\mu$  at temperature 25°C. Prediction of  $\langle R_h \rangle$  by Eq. (5.11) for three different values of  $a_0$  are shown in figure A. Three fits of experimental data by Eq. (5.11) are shown in figure B, C and D.

As shown in Figure 5.5 A, a change of parameter  $a_0$  results merely in a vertical shift of the fitting curve. Therefore, first  $R_h$  dependence on  $\mu$  is fitted for  $a_0$  keeping  $\gamma = 0$  (fitting range of  $\mu < \text{optical matching point}$ , it is almost independent of  $\gamma$ ), then using obtained value of  $a_0$ , position of optical matching point and sigmoidal shape of  $R_h$ , which is characteristic shape of polydisperse MEs is fitted for different  $\gamma$  values. A reasonable fit of experimental data can be obtained with  $a_0$  and  $\gamma$  shown in Figure 5.5 (B, C and D) and listed in Table 5.3, which leads to optical matching point at  $\mu \sim 35, 25$  and  $20$  as expected from Figure 5.4 (see Table 5.3).

Further, as shown in Figure 5.5 (B, C and D), linear dependence of  $R_h$  on  $\mu >$  the value for optical matching point (assuming that area per surfactant molecule at interface  $a_s$  does not depend on the  $\mu$ , when  $\mu >$  the value for optical matching point, it is reasonable assumption for  $\mu \gg 20$ , second term in Eq. (5.9) tend to zero for  $\mu \gg 20$  and  $a_s \sim a_0$ ) are fitted according to the linear Eq. (5.8), which yield thickness of surfactant layer  $L$  (from intercept) and area occupied by a surfactant molecule on interface  $a_s$  (from slope) for given value of  $\gamma$ . Clearly the two parameters  $\gamma$  and  $a_s$  can not be determined separately from the linear dependence of  $R_h$  on  $\mu$ . The latter value is recovered for  $\gamma = 0.03$  (for best fitted value see Figure 5.5) and given in Table 5.3. The values obtained for  $a_0$  are in agreement with the values obtained earlier by fitting Eq. (5.11) and found in literature e.g.,  $a_0 = 52.6 \text{ \AA}^2$  at  $\mu = 36.5$  for AOT molecule in *n*-heptane obtained by time-resolved fluorescence probing<sup>107</sup> and  $a_0 = 48$  for AOT molecule in isooctane<sup>82</sup> (see Table 5.3). *The fact that one can obtain a self-consistent interpretation of DLS data using optical properties Eq. (5.11) or packing consideration Eq. (5.8) on the basis of the layered sphere model.*

	DLS						SLS	
	Eq. (5.11)			Eq. (5.8)			Eq. (3.13)	
	$g$	OMP	$a_0 [\text{\AA}^2]$	$g$	$a_0 [\text{\AA}^2]$	$L [\text{\AA}]$	$g$	OMP
<b>water/AOT/<i>n</i>-heptane</b>	0.03	35	56	0.03	52	22.7	0.03	35
<b>water/AOT/<i>n</i>-octan</b>	0.03	25	50	0.03	50	25.6	0.03	25
<b>water/AOT/<i>n</i>-nonane</b>	0.03	20	46	0.03	46	25.0	0.03	20

**Table 5.3** Results (polydispersity index  $g$ , optical matching point OMP and area per head group at interface  $a_0$ , when  $\mu \gg 20$ ) obtained from DLS and SLS.

### 5.1.2.3 SLS Results

A similar effect as obtained for  $\langle R_h \rangle$  can be observed in the dependence of the normalized intensity  $\langle I_s \rangle$  on  $\mu$ . As shown in Figure 5.6A that our systems exhibit a well-defined minimum of the intensity at values of matching point listed in Table 5.3 (as expected from Figure 5.4 and Figure 5.5). First we can see in Figure 5.6A, at the optical matching point, normalized intensity goes through zero for monodisperse systems. However, if the droplets are polydisperse, in the vicinity of optical matching point the scattering intensity exhibits a sharp dip but there remains a substantial residual scattering. Second, a change of parameter  $a_0$  results merely in a vertical shift of the fitting curve. The depth and position of the characteristic dip of the normalized scattering intensity at the optical matching can be fitted with only one free parameter  $\gamma$ . A reasonable fit of experimental data and theoretical curves according to Eqs. (3.13) and (3.14) can be obtained with  $\gamma$  shown in Figure 5.6 (B, C and D)

and listed in Table 5.3, which leads to optical matching point at  $\mu \sim 35, 25$  and  $20$ . The values for  $\gamma$  are in agreement with the values obtained from DLS. *The fact that one can obtain a self-consistent interpretation of SLS and DLS data on the basis of the layered polydisperse sphere model- both sets of data resulting from fundamentally different measurements – confirm the small polydispersity  $s_s = \sqrt{g} = 0.17$  of the droplet radius in MEs and independent of n-alkane chain as already predicted theoretically from multiple chemical equilibrium approach<sup>108,109</sup> that the size polydispersities  $s_s$  in the range of 0.1 to 0.25 and independent on the alkane type.<sup>110,111,112</sup> These values are also consistent with the values  $s_s = 0.16$  obtained from careful analysis of SANS data in the full  $\bar{q}$  range for  $D_2O/AOT/decane$  and  $D_2O/AOT/iso-octane$  by Arleth et al.<sup>100</sup>*

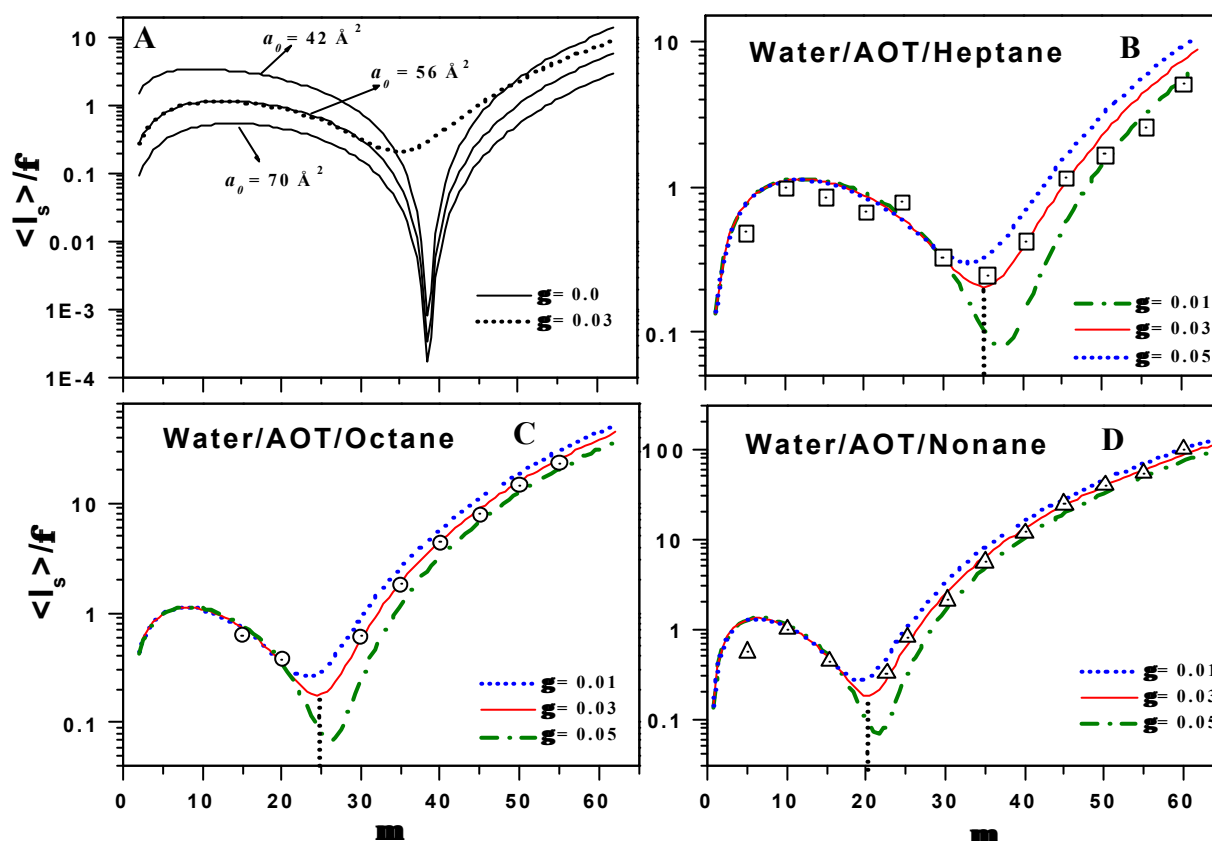


**Figure 5.6** Normalized scattering intensity  $\langle I_s \rangle / f$  of ME droplet as a function of the  $\mu$  at temperature 25°C. Prediction of  $\langle I_s \rangle / f$  by Eq. (3.13) for three different values of  $a_0$  are shown in figure A. Three fits of experimental data by Eq. (3.13) are shown in figure B, C and D.

We note that area per AOT head group decreases as the alkane chain length increases (see Table 5.3). The possible explanation for this is that  $R_h$  is slightly larger (see Figure 5.5) in the larger chain alkane oil because oil penetration into the surfactant tail region is smaller, which causes decrease in spontaneous curvature of the surfactant layer in comparison to smaller chain. Small droplets have larger area per volume than the large droplet. This implies that area per AOT head group decreases with increase of chain length. The values for thickness of the surfactant layer  $L$  (see Table 5.3) are somewhat higher than the value estimated for

hydrophobic chain length of surfactant (AOT)  $L = 9 \text{ \AA}$ . This deviation could be explained by assuming the existence of several layers of solvent molecules, which migrate with the droplet.

Further more, SANS data for AOT-n-Octane- $D_2O$  systems at three different  $\mu$  values are fitted in Guinier approximation range, [see Eq. (3.64)] yielding the gyration radius. This size parameter is connected with the moment of inertia of the particle. Best fitting obtained using Guinier approximation is shown in Figure 5.7A. The results are shown in Figure 5.7B as a function of  $\mu$ . As it is shown in Figure 5.7B, the obtained radius increases linearly with slope 1.87 which is in agreement with the result obtained from DLS (see Figure 5.5). One can calculate the ratio between  $R_g$  and  $R_h$  and got the values 0.79, 0.84 and 0.89 for  $\mu=25, 35$  and 45 respectively. These values are quite in agreement for the smallest possible value of 0.77 for solid spheres justifying our calculations, in which we used a sphere droplet model.

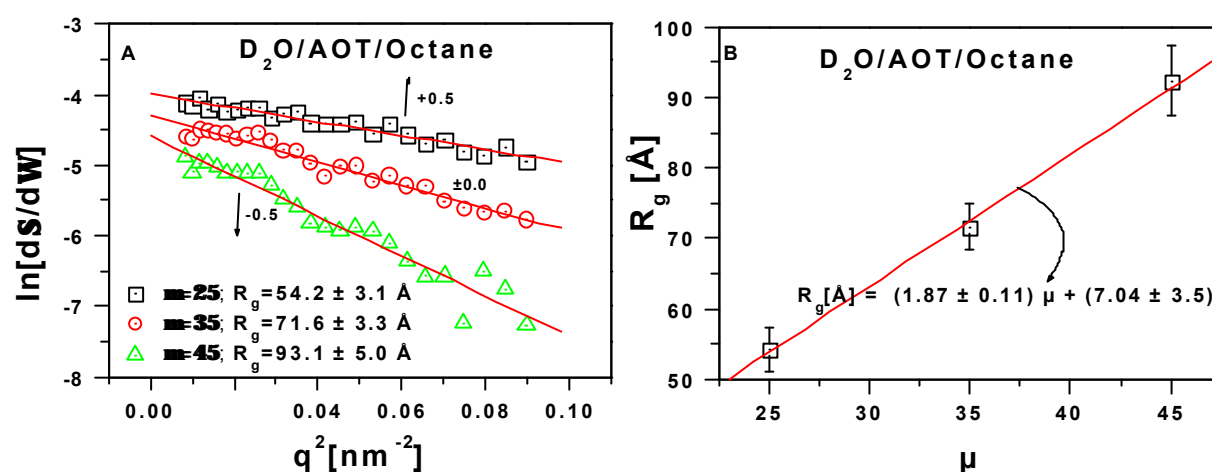


**Figure 5.7** (A) Best fitting of SANS data of  $D_2O/AOT/n-Octane$  MEs using Guinier approximation. (B) Gyration radius of ME versus  $\mu$ .

### 5.1.3 Interdroplet interactions and droplet size

In addition to their practical applications, AOT-MEs represent an ideal model structure for studying interdroplet interactions. DLS studies on concentration dependence of diffusion coefficients allow to determine the virial coefficients of diffusion and the hydrodynamic radius of ME droplets. SLS study on concentration dependence enable one to determine the osmotic compressibility<sup>35</sup> and apparent molar mass<sup>33</sup> that are the function interdroplet interaction too. A dilution procedure was used in the region of the phase diagram where the ME has the microstructure of AOT covered water droplets in oil, which allowed us to deduce the concentration dependence of DLS and SLS data.

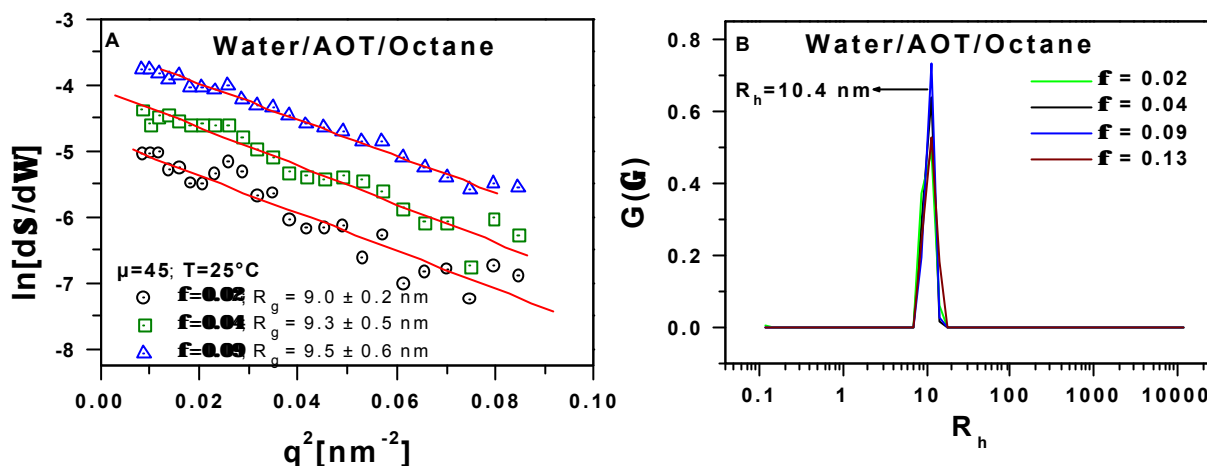
Following measurements of water/AOT/*n*-alkanes MEs over the large range of  $\phi$  (0.02 – 0.50) at constant  $\mu=45$  and  $T=25^\circ\text{C}$  are presented and discussed.

- I. SANS measurement and CONTIN fit of DLS data were used to check, whether dilution procedure preserves a constant droplet radius or not.
- II. SLS enables one to determine the osmotic compressibility that is related to the interaction potential between the droplets.
- III. DLS study on concentration dependence of diffusion coefficients allows one to determine droplet size, polydispersities (both optical and size) and the virial coefficients of diffusion that are also related to the interaction potential between the droplets.

Chain length of the *n*-alkane has been varied in order to show the dependence of some general features of systems on chain length of *n*-alkane. The composition of the MEs used is summarized in Table 5.1 under heading “*dilution*”.

#### 5.1.3.1 SANS and CONTIN Results

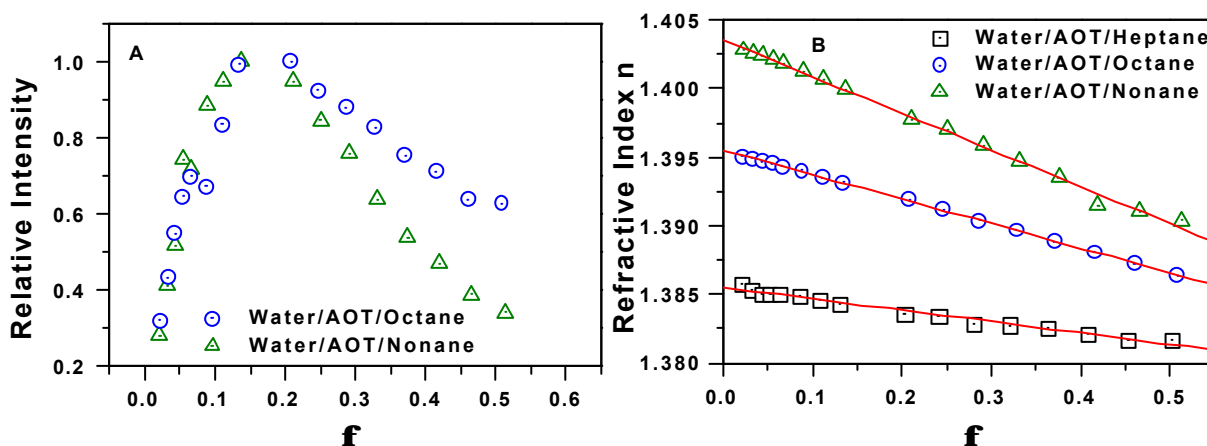
Constancy of droplet size were checked by SANS and DLS measurements at high dilution because at low volume fraction, droplet is strongly strained by interactions with solvent molecules, which may cause change in droplet size. SANS curves for  $\text{D}_2\text{O}/\text{AOT}/n$ -octane-systems having different  $\phi$  (at constant  $\mu=45$ ) are analyzed using Guinier approximation [see Eq. (3.64)]. Best fitting and gyration radius obtained using Guinier approximation is shown in Figure 5.8A. DLS data for  $\text{H}_2\text{O}/\text{AOT}/n$ -octane systems having different  $\phi$  (at constant  $\mu=45$ ) are analyzed using CONTIN [see Eq. (4.5)]. Results are shown in Figure 5.8B. It shown in Figure 5.8, the obtained radius remains constant (with in experimental error) on high dilution. As expected, the gyration radius is substantially smaller than  $R_h$ .



**Figure 5.8 (A)** Best fitting and results of SANS data of AOT-*n*-Octane- $D_2O$  systems using Guinier approximation. **(B)** Results of DLS data of AOT-*n*-Octane- $H_2O$  systems using CONTIN fit ("Probability to Reject" = 0.5, used for Fisher F-test).

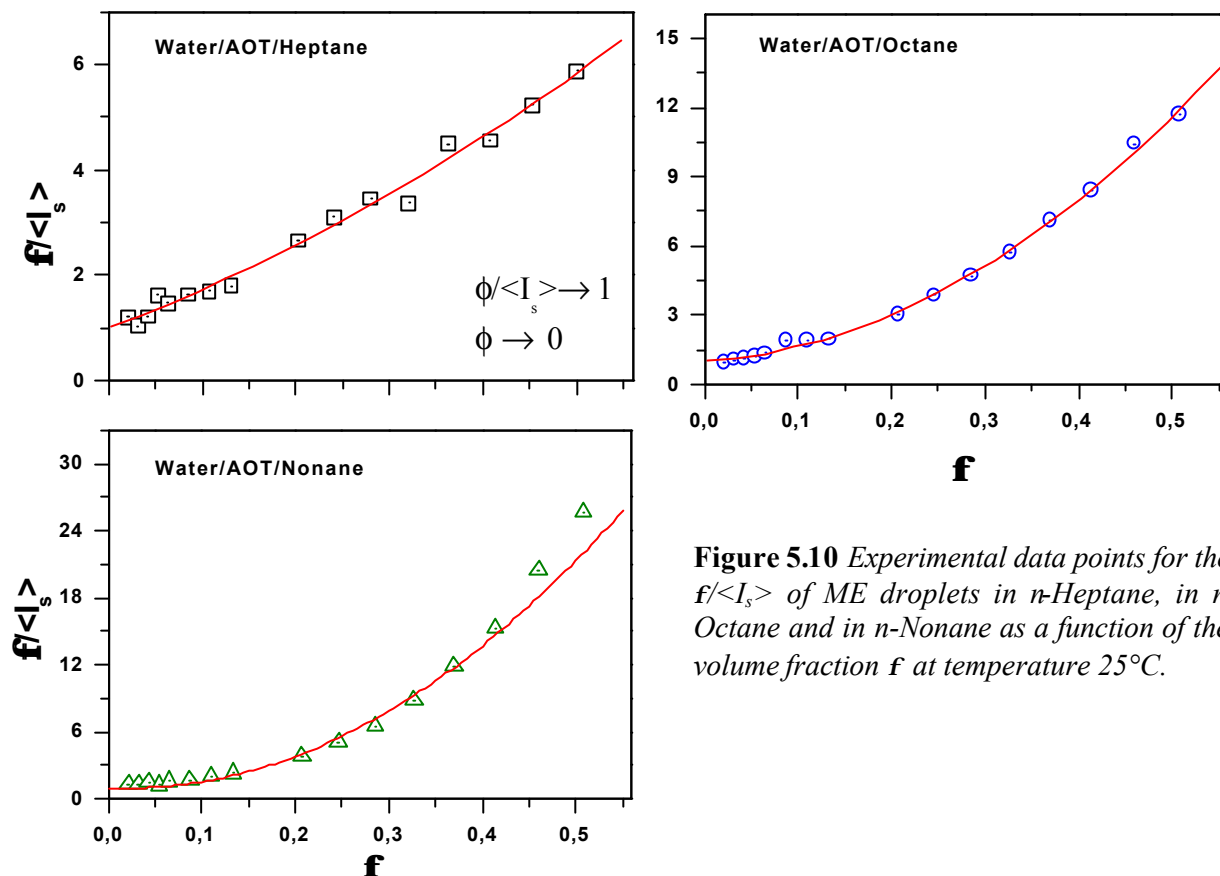
### 5.1.3.2 SLS Results

Figure 5.9A shows examples of relative scattered intensity variation versus  $\phi$ . For all the MEs studied, their relative intensities pass through their respective maxima at  $\phi \sim 0.16$  and differ afterward with increasing  $\phi$ . This is classical behavior for a system having comparable droplet size but different strength of interaction. This is consistent with the fact that all the MEs studied have constant molar water to AOT ratio  $\mu$  hence comparable size. Strength of interaction can be estimated by fitting the average normalized intensity  $\langle I_s \rangle$  using an expression given in Eq. (3.11) provided systems under investigations are ideal mixtures and droplet radius remains constant. A proof of the constancy of droplet size can be found in Figure 5.8. In Figure 5.9B,  $\phi$  dependence of refractive index is presented in order to check whether our systems are ideal mixture or not.



**Figure 5.9 (A)** Relative intensity  $I$  as a function of  $f$  for MEs of comparable droplet sizes but different attractive interactions. **(B)** Refractive index of the ME droplets in *n*-heptane, in *n*-octane and in *n*-nonane as a function of the volume fraction  $f$  at temperature  $25^\circ\text{C}$ .

The  $dn/d\phi$  for each series of MEs is found to be constant upon dilution at 25°C, the MEs investigated are thus considered to be the ideal mixtures. The value of refractive index of continuous phase ( $n$ -alkanes) was in good agreement with those obtained from the extrapolations of the plots of refractive index ( $n$ ) versus  $f$  as  $f$  approaches to zero.



**Figure 5.10** Experimental data points for the  $\phi / \langle I_s \rangle$  of ME droplets in  $n$ -Heptane, in  $n$ -Octane and in  $n$ -Nonane as a function of the volume fraction  $f$  at temperature 25°C.

As discussed above that systems under study are ideal mixture and droplet size does not vary significantly over wide range of  $\phi$ , under such conditions normalized intensity  $\phi / \langle I_s \rangle \rightarrow 1$  as  $\phi \rightarrow 0$  can be fitted according to Eq. (3.11). Figure 5.10 shows the variation of  $\phi / \langle I_s \rangle$  versus  $\phi$  and quadratic fit according to Eq. (3.11). Quadratic best fit yields  $K_I$  given in Table 5.5. To estimate the magnitude of the attraction and repulsion giving rise to  $K_I$ , the measured value is generally compared to the  $K_I^{HS}$  for a hard sphere repulsion. Hard sphere contribution to the virial coefficient  $K_I^{HS}$  is 8. If  $\Delta K_I = K_I - K_I^{HS}$  is positive, the droplets have a net repulsive interaction while if  $\Delta K_I$  is negative, the droplets are attractive.<sup>113,38,122</sup> For this system,  $\Delta K_I$  (see Table 5.5) is negative as expected for droplets interacting via hard sphere interaction with perturbation of attractive potential. The ME droplets in longer  $n$ -alkane chain length oil are more attractive (larger negative  $\Delta K_I$  value, see Table 5.5) than those in smaller  $n$ -alkane chain length. AOT molecules along with the interface of the ME droplets allow penetration of the surfactant hydrophobic chains of the other droplets during collisions. The overlapping of the penetrable volume of the ME droplets under dynamic motion giving rise to an attractive interaction. Such systems undergo Brownian motion in the usual fashion and the attractive energy gives rise to “sticky” interactions due to surface adhesion upon collision<sup>114</sup>. Such

sticky encounters result in short lived clusters that may exchange solubilized material before dissociating into separate droplets causing collective and self diffusion of droplets.<sup>115</sup> In the next section, collective and self diffusion coefficients were measured by DLS. From the concentration dependence of diffusion coefficients, droplet size, polydispersities (both optical and size) and the virial coefficients of diffusion that are also related to the interaction potential between the droplets were determined.

W/O - ME Composi- tions	SLS		DLS					
			Cumulant		Bi-Exp			
AOT + water +	$K_I$	$dK_I$	$(k_{app})^{HS}$	$k_{app}$	$a_1^c$	$da_1^c$	$a_1^s$	$da_1^s$
<i>n</i> -heptane	6.67 ± 1.12	-1.33	0.53	-1.17 ± 0.02	2.09 ± 1.20	0.53	-2.20 ± 0.35	-0.10
<i>n</i> -octane	2.63 ± 1.15	-5.37	1.43	-0.61 ± 0.02	0.90 ± 0.35	-0.66	-2.30 ± 0.16	-0.20
<i>n</i> -nonane	-3.68 ± -1.97	-11.68	1.51	-1.44 ± 0.11	-1.34 ± 0.36	-2.90	-3.17 ± 0.14	-1.07

**Table 5.4** Fitting parameters of scattered light (SLS) and diffusion coefficients (DLS) of the ME droplets in *n*-heptane, *n*-octane and *n*-nonane at temperature 25°C (see text for details).

### 5.1.3.3 DLS Results

Field auto correlation functions  $g(\tau)$  measured from DLS (see Section 4.1 for the detail) at two volume fractions,  $\phi = 0.02$  and  $\phi = 0.36$  are shown in Figure 5.11. Striking features of these experiments was the two-exponential nature of the correlation functions observed at large  $\phi$ . It can be easily seen in Figure 5.11 that at large  $\phi = 0.36$ ,  $g_1(\tau)$  is best fitted by two-exponential, while at  $\phi = 0.02$ ,  $g_1(\tau)$  is best fitted by single-exponential. The data for samples with  $\phi > 0.20$ , could be fitted well by the sum of two exponentials. Below this concentration it was difficult to resolve the two exponentials unambiguously, in these cases data were fitted to third-order cumulants expansion [see Eq. (4.6)]. Apparent diffusion coefficient  $D_{app}$  was deduced from first cumulant using Eq. (4.7). To get the free diffusion coefficients of droplets  $D_0$ ,  $D_{app}$  is extrapolated to  $\phi \rightarrow 0$ . Mean droplet hydrodynamic radius  $R_h$  obtained from  $D_0$  using Eq. (3.44) is listed in Table 5.5. It is seen that  $R_h$  slightly increases with increase of length of *n*-alkane chain, which is consistent with the results obtained from contrast variation experiment in the Section 5.1.2.

The most likely interpretation of the two exponential decay of correlation function at high volume fraction seems to be polydispersity and interaction of the droplets, which would lead to the observation of coherent (number density fluctuation) and incoherent (polydispersity fluctuation) scattering as outlined in Chapter 3. These two fluctuation modes at high volume fraction have been observed in several DLS measurements on concentrated (or strongly interacting) system such as dispersion of silica spheres,<sup>47,46</sup> latex particles,<sup>116,117</sup> MEs<sup>118,119</sup>

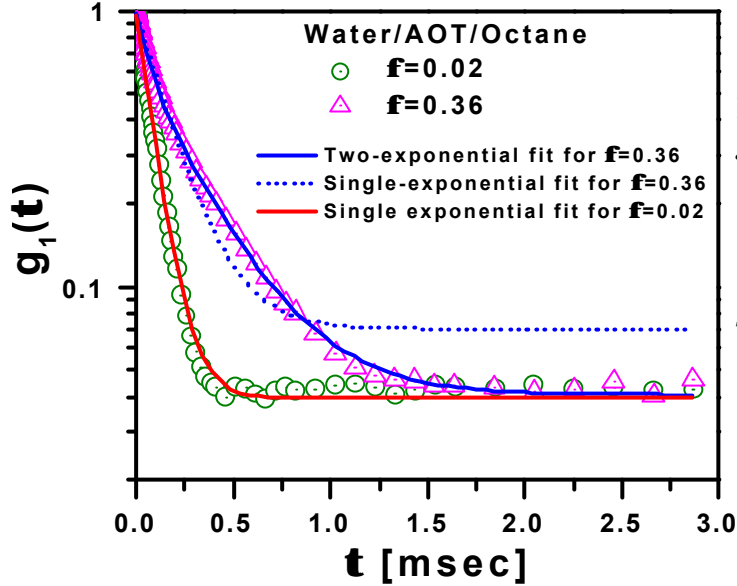


**Figure 5.11** DLS autocorrelation data  $g_1(t)$  for ME AOT/Water/n-Octane with  $f = 0.02$  and  $f = 0.36$  at  $25^\circ\text{C}$ . For  $f = 0.36$ , two exponential fit is plotted through the — (solid line) and inadequate single exponential best fit is shown as - - - (broken line). for  $f = 0.02$ , single exponential fit is plotted through the — (solid line).

In the so called thermodynamic or hydrodynamic limit,  $q^{-1} > r_{\text{mean}}$  (the interparticle spacing) and  $\tau_c$  (characteristic decay time)  $> \tau_1$  (droplet collision time), number density fluctuation mode (fast mode) represents collective diffusion and concentration or polydispersity fluctuations mode (slow mode) represents self diffusion.<sup>27</sup> In order to check criteria for hydrodynamic regime, first we calculate typical value of mean interdroplet spacing  $r_{\text{mean}}$  and droplet collision time  $\tau_1$  for these experiments. For  $\phi > 0.20$ , and  $R \sim 10$  nm (which is comparable with our measured value listed in Table 5.5), mean interdroplet spacing  $r_{\text{mean}} \sim \langle C \rangle^{-1/3} \leq 2.2 \times 10^{-6} \text{ cm}$  (where  $\langle C \rangle$  is the droplet number density) and maximum scattering vector  $\vec{q}$  attainable in a light scattering experiment is about  $3.16 \times 10^5 \text{ cm}^{-1}$ . The maximum value for the droplet collision time  $\tau_1$  can be taken as the time needed by the droplet to diffuse freely a distance equal to the interdroplet spacing, i.e.,  $\tau_1 < \langle C \rangle^{-2/3} / 6D_0 \sim 10^{-7} \text{ sec}$  (for free droplet diffusion coefficient  $D_0 = 42 \times 10^{-8} \text{ cm}^2/\text{sec}$ ). At  $|\vec{q}| = 3.16 \times 10^5 \text{ cm}^{-1}$  the characteristic decay time of the free diffusional decay of the light scattering correlation function is  $\tau_c = (D_0 q^2)^{-1} \sim 10^{-4} \text{ sec}$ . Thus for this example, where extreme values of  $\vec{q}$  and  $\tau_1$  have been considered, we certainly full fill the criteria  $q^{-1} > r_{\text{mean}}$  and  $\tau_c > \tau_1$  for the hydrodynamic regime. The slow and fast decay mode can thus be assigned to the relaxation by self-diffusion and collective diffusion. Figure 5.12 shows a corresponding plot of results

obtained by two-exponential fit and cumulant fit at 25°C. In Figure 5.12, large statistical error bar over the range  $0.20 < \phi < 0.30$ , represent the break down of assumption that number density and polydispersity fluctuations are completely uncoupled in this  $\phi$  range leading to Eq. (3.42)<sup>27</sup>. This explains why the value of  $D_c$  deviates from its expected value over the range  $0.20 < \phi < 0.30$ .

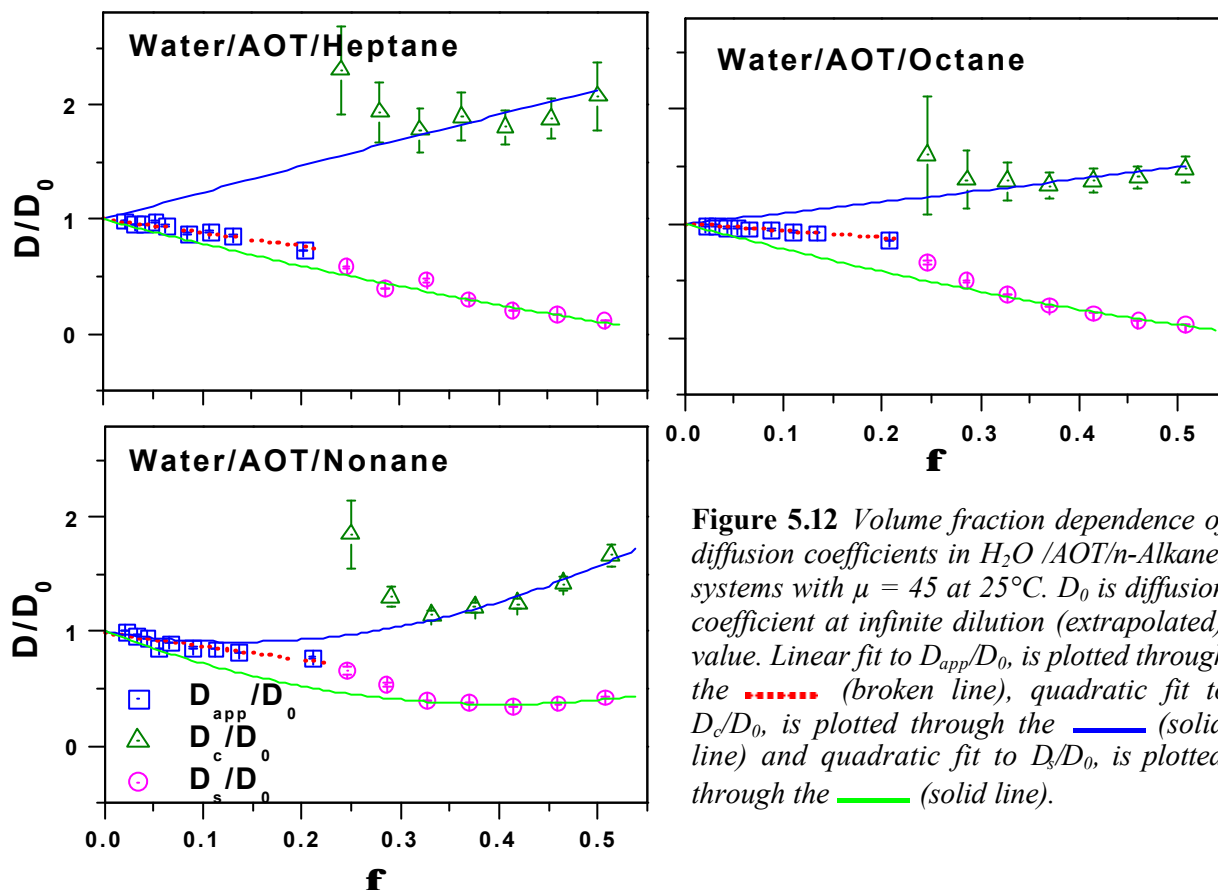


**Figure 5.12** Volume fraction dependence of diffusion coefficients in  $H_2O$  /AOT/ $n$ -Alkanes systems with  $\mu = 45$  at 25°C.  $D_0$  is diffusion coefficient at infinite dilution (extrapolated) value. Linear fit to  $D_{app}/D_0$ , is plotted through the  $\cdots$  (broken line), quadratic fit to  $D_c/D_0$ , is plotted through the  $\text{---}$  (solid line) and quadratic fit to  $D_s/D_0$ , is plotted through the  $\text{---}$  (solid line).

Each of three diffusion coefficients ( $D_c$  and  $D_s$  obtained from two exponential and  $D_{app}$  from cumulant fit represented in Figure 5.12) should fit to the same value,  $D_0$  as  $f \rightarrow 0$ , so the use of two methods of data analysis permits this point to be fixed quite accurately.  $D_0$  can be identified with  $D_{app}$  when  $f \rightarrow 0$ , which is used for the calculation of hydrodynamic radius. As shown in Figure 5.12, the diffusion coefficient  $D_s$  decreases in value with increasing volume fraction, whereas  $D_c$  for the short-time relaxation shows a increase. This is consistent with the interpretation that  $D_s$  describes polydispersity fluctuations by self diffusion and that  $D_c$  arises from mutual diffusion of ME droplets. Mutual diffusion can be regarded as being driven by osmotic pressure and retarded by interdroplet friction [see Eq.(3.36)].<sup>27</sup> By contrast, for self diffusion, the osmotic term is absent and dominant effect is the increasing value of friction coefficient with concentration, tending to reduce the diffusion coefficient [see Eq. (3.37)].<sup>27</sup> It should be noted that  $D_{app}$  is more close to extrapolated values of  $D_s$  for  $\phi < 0.2$  in case of water/AOT/ $n$ -heptane system in comparison to water/AOT/ $n$ -octane and water/AOT/ $n$ -nonane systems as expected from Eq. (3.48). According to the Eq. (3.48), far

from matching point  $D_{app}$  represents  $D_c$  and in the matching point  $D_{app}$  represents  $D_s$  [ $\mu = 45$  is more close to the optical matching point for water/AOT/*n*-heptane at  $\mu=35$  than optical matching point for water/AOT/*n*-octane at  $\mu=25$  and water/AOT/*n*-nonane at  $\mu = 20$  [see Table 5.3)].

We now consider in more detail the variation of  $D_c$  and  $D_s$  obtained from DLS with the volume fraction. The decrease in  $D_s$  and increase in  $D_c$  fits satisfactorily to a quadratic Eq. (3.47) over the range  $0.20 < \phi < 0.5$  with  $\mathbf{a}_1^{c,s}$  and  $\mathbf{a}_2^{c,s}$  listed in Table 5.5 (see Figure 5.12). If we assume that the droplet size does not vary significantly over concentration range then these results can be compared with theoretical predictions to the first order in the volume fraction. A proof of the constancy of droplet size can be found in Figure 5.8 and Figure 5.12 [same  $D_0$  obtained over measured range of concentration, which is related to the hydrodynamic radius according to Stokes-Einstein relation Eq. (3.44)]. To estimate the magnitude of the attraction and repulsion giving rise to  $\mathbf{a}_1^{c,s}$ , the measured value is generally compared to the  $\mathbf{a}_1^{c,s}$  for a hard sphere repulsion. Grenz et al<sup>120</sup> and Cichocki et al<sup>121</sup> obtained using theoretical approach that the difference of the self-diffusion of Brownian particles with hydrodynamic interaction from its hard sphere value  $\mathbf{d}\mathbf{a}_1^s = \mathbf{a}_1^s - (\mathbf{a}_1^s)^{HS}$  is negative for an attractive potential and positive for repulsive interaction (see Fig 5 in ref. 121 and Fig. 7 in ref. 120). Grenz et al<sup>120</sup> also predicted that attractive interaction becomes stronger as the negative value of  $\mathbf{d}\mathbf{a}_1^s$  is increased. For hard spheres,  $(\mathbf{a}_1^c)^{HS} = 1.56$  and  $(\mathbf{a}_1^s)^{HS} = 2.10$  (see Appendix A). For studied systems,  $\mathbf{d}\mathbf{a}_1^s$  (see Table 5.5) is negative as expected for droplets interacting via hard sphere interaction with perturbation of attractive potential.

The difference of the virial coefficient obtained from collective diffusion from its hard sphere value  $\mathbf{d}\mathbf{a}_1^c = \mathbf{a}_1^c - (\mathbf{a}_1^c)^{HS}$  is negative if there are supplementary attractive interactions and positive in the case of additional repulsive interactions.<sup>122,38</sup> For studied systems,  $\mathbf{d}\mathbf{a}_1^c$  (see Table 5.5) is negative (apart from  $\mathbf{a}_1^c$  for water/AOT/*n*-heptane, where  $\mathbf{d}\mathbf{a}_1^c$  is negative: the possible explanation for this is that large statistical error in the value  $\mathbf{a}_1^c$  and value of  $(\mathbf{a}_1^c)^{HS}$  for hard sphere is predicted in dilute regime may cause the slightly larger value) as expected for droplets interacting via hard sphere interaction with perturbation of attractive potential. The ME droplets in longer *n*- alkane chain length oil are more attractive (larger negative  $\mathbf{d}\mathbf{a}_1^{c,s}$  value, see Table 5.5) than those in smaller *n*- alkane chain length.

Now we now consider in more detail the variation of  $D_{app}$ , obtained from DLS with the volume fraction. The decrease in  $D_{app}$  fits satisfactorily to a linear Eq. (3.49) over the range  $0 < \phi < 0.20$  (see red dotted line in Figure 5.12), with  $k_{app}$  given in Table 5.5.

In W/O - ME, it has been already shown that our system represents the case where hard-sphere repulsive force operates with a narrow attractive potential energy well, i.e., the structure of AOT may be considered a repulsive core (charged head groups) with an attractive outer shell (i.e., the tails). Assume that interdroplet interaction has pair wise form so the pair

interaction potential can be written as Eq. (3.70). Hard sphere repulsive  $U_{HS}$  and van der Waals attractive potential give the dominant contribution to direct interaction  $U_{dir}$ . van der Waals attraction is frequently negligible and overall contribution to the  $U_{dir}$  is  $U_{HS}$ . Finally, indirect  $U_{ind}$  should involve the solvent degree of freedom. If two droplets approach each other, the ends of their surfactant tails may overlap while lowering the free energy of the system and giving rise to the attractive interaction.<sup>123</sup> Thus interdroplet interaction potential  $U(r)$  for our system can be described by simple model potential of a hard core  $U_{HS}(r)$  due to direct contribution plus a attractive square well  $U_{att}(r)$  with depth  $\epsilon k_B T$  and range  $x$  scaled by the droplet diameter due to indirect contribution (see Figure 5.13)

$$(5.12) \quad U(r) = U_{HS}(r) + U_{att}(r)$$

$$U(r) = \begin{cases} \infty & r \leq R_{core} \\ -\epsilon k_B T & 2R_{core} < r < 2R_{core}(1+x) = r_1 \\ 0 & r > 2R_{core}(1+x) = r_1 \end{cases}$$

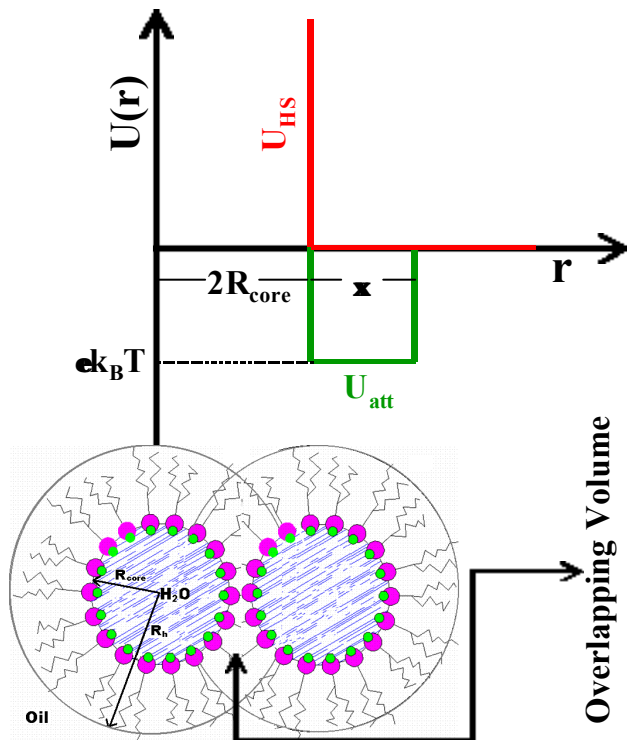


Figure 5.13 Schematic representation of a model potential  $U(r)$  of an attractive well added to the hard core repulsion.

We assumed  $x = h/2R_{core}$  to be constant ( $h = 3 \text{ \AA}$  is the range of interaction determined by SANS<sup>124</sup> and this is consistent with the interpenetration model).  $R_{core}$  is obtained from Eq. (5.7), for  $\mu = 45$ )

For such interacting system,  $k_{app}$  is as follows<sup>125,126</sup>

$$(5.13) \quad k_{app} = (k_{app})^{HS} + (k_{app})^{att}(\epsilon, x)$$



oriented to interact with the surfactant tails, while the surfactant tails between two MEs in the overlap region are always more or less parallel to each other. For the higher temperature, it is harder for the oil to pack in a favorable orientation to interact with the surfactant tails. And when the temperature is high enough, phase separation will occur due to the strong surfactant-surfactant interactions. Similarly, we can understand that at constant temperature, it would be harder for the longer *n*-alkane oil molecule to interact with the surfactant than for shorter oil molecule to interact, due to packing considerations. Thus a system containing longer *n*-alkane chain length are more attractive (more surfactant to surfactant attractive interaction) than those with smaller *n*-alkane chain length at constant temperature. This mechanism could also explain the shift of the region of ME stability to lower temperatures for higher chain length alkanes.<sup>127</sup>

W/O - ME Compositions	Size		Interaction		Polydispersity	
	$D_0$ [ $10^8$ cm <sup>2</sup> /sec]	$R_h$ [nm]	$\epsilon$ [k <sub>B</sub> T]	$P \frac{k_B T}{A^3}$	$s_s$	$s_o$
<i>n</i> -heptane	55.43	10.12	2.07	0.00146	0.17	0.45 ± 0.10
<i>n</i> -octane	41.75	10.30	2.27	0.00157	0.17	0.20 ± 0.05
<i>n</i> -nonane	29.28	11.21	2.54	0.00161	0.17	0.15 ± 0.05

**Table 5.5** The size, polydispersity and interaction energy and the related parameters of the ME droplets in *n*-heptane, *n*-octane and *n*-nonane at temperature 25°C (see text for details).

This attractive surfactant to surfactant interaction becomes stronger as the microemulsion droplets sizes (hence the penetrable volumes) are increased. This view is also consistent with the result that the micro emulsion droplets in longer *n*-alkane chain length oil are more attractive than those in smaller *n*-alkane chain length (since the ME droplet radius is slightly higher in larger *n*-alkane chain length oil for a given composition, see Figure 5.5 and Table 5.5). According to this mechanism,  $\epsilon$  is proportional to the maximum penetration volume  $v(R_h, h)$  of the two spherical shell<sup>128</sup>

$$(5.15) \quad \begin{aligned} \epsilon &\propto v(R_h, h) \\ &\approx P \frac{h^2 \left( 3R_h - \frac{h}{2} \right)}{6} \end{aligned}$$

where,  $h$  is maximum penetration and  $P$  is interaction energy density per droplet.

Assuming a macroscopic model mentioned above for the interaction of interpenetrating surfactant tails, interaction energy density  $P$  per droplet is estimated from  $\epsilon$  using Eq. (5.15). The values of  $P$  are listed in Table 5.5.

It has been shown that our system represents the case where hard-sphere repulsive force operates with a narrow attractive potential energy well. Attractive energy gives rise to “sticky” interactions due to surface adhesion upon collision. Such sticky encounters result in short lived clusters that may exchange solubilized material before dissociating into separate droplet causing distribution in size as well as refractive index (since water and AOT have different refractive index) of droplets. The size polydispersity  $\sigma_s$  measured for all our systems using second cumulant  $\Gamma_2$  suitably normalized by  $\Gamma_1$  is 0.25 with error  $\pm 10\%$ . It should be noted that this value lies on the higher side of our measured value from contrast variation experiments. As already pointed in contrast variation experiments that the second cumulant  $\Gamma_2$  (represents only small correction to the shape of the correlation function) overestimate the polydispersity of ME droplets. In the more concentrated systems, where polydispersity fluctuations become distinguishable, a value for  $\sigma_s$  and  $\sigma_o$  can be obtained from relative amplitude of the slow decay mode using coupled combination of optical and size polydispersities theoretical results,<sup>45,46,47</sup> which are valid for narrow size distribution. A reasonable theoretical fit for combined size and optical polydispersity:  $\sigma_s = 0.17$  with  $\sigma_o = 0.45 \pm 0.11$ ,  $0.20 \pm 0.05$  and  $0.15 \pm 0.050$  for water/AOT/*n*-heptane, water/AOT/*n*-octane and water/AOT/*n*-nonane, respectively, can be obtained (solid lines in Figure 5.15). In Figure 5.15, inadequate theoretical predictions for pure size polydispersity are also shown. These values for the optical polydispersities are consistent with the values estimated from the residual scattering of samples at matching point (0.063, 0.22 and 0.14 for water/AOT/*n*-heptane, water/AOT/*n*-octane and water/AOT/*n*-nonane). It is observed that optical polydispersity decreases with increasing oil chain length as it is expected from difference between refractive index of  $n_s$  and  $n_o$ , which decreases with increasing chain length.

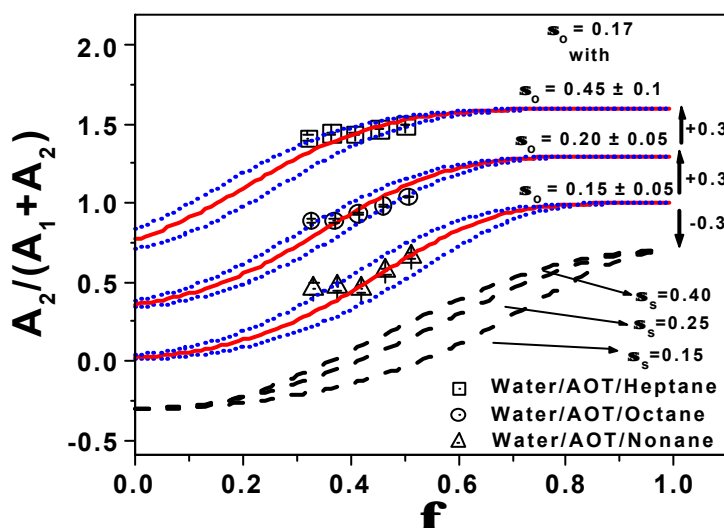


**Figure 5.15** Relative amplitude of slow relaxation (points) caused by polydispersity fluctuations plotted as a function of volume fraction for ME droplets in *n*-heptane, *n*-octane and *n*-nonane at temperature 25°C. The lines are the predictions for pure size and combined optical and size polydispersity (see Appendix B for details).

In interpreting the above results it is useful to estimate the time scale of the collision-induced polydispersity fluctuations  $\tau_p$ .  $\tau_p$  can be taken roughly as the lifetime of the nearest neighbor shell of droplets surrounding a given “test” droplet. If  $\tau_c \gg \tau_p$ , in this limit, DLS observes slow fluctuations of macroscopic spatial extent and, local effect would damp out the spatial polydispersity correlation and droplet self-diffusion would not be observed by DLS.<sup>129</sup> Since

the evidence discussed above strongly suggest that for  $\phi > 0.20$ , self diffusion is being measured. We conclude that  $\tau_p \gg \tau_c \sim 10^{-4}$  sec. At  $\phi > 0.20$ , the binary collision rate can be estimated<sup>130</sup> as  $\tau_1 \sim 10^{-7}$  sec. So the indications are that the polydispersity fluctuations are at least three orders of magnitude slower than the droplet collision frequency, which is in good agreement with previous estimates.<sup>118</sup>

As shown earlier that at high concentration, DLS data can be interpreted in terms of the sum of two independent modes due to collective diffusion and polydispersity fluctuation respectively. It has been shown that  $D_c$ ,  $D_s$  and interdroplet interaction are the function of solvent refractive index  $n_o$ . Investigation of the interdroplet interaction and polydispersity of ME should be tried with this theoretical prediction using contrast variation of solvent by mixing two solvent having different refractive index. Investigation of MEs having water, AOT and the mixture of *n*-heptane and *p*-xylene are in progress.

### 5.1.4 Shape Fluctuations of ME Droplets with Increasing Temperature

For all the MEs prepared for this section, water weight percentage  $\Theta$  was fixed at 5%. The molar ratio of water and AOT was either 50 or 60 for water/AOT/*n*-heptane, 45 or 55 for water/AOT/*n*-octane and 30 or 40 for water/AOT/*n*-nonane. The composition of the MEs used for investigations are summarized in Table 5.1 under heading “*temperature dependent*”. Due to small droplet size and the low polydispersity ( $\sigma_s \sim 0.17$ ) the scattering intensity near the matching point is very low, which leads unfavorable signal to noise ratio. Therefore  $\mu$  values are chosen far from matching point to get sufficient intensity. Figure 5.16A shows an example of relative scattered intensity  $I_s$  variation versus  $\mu$ . It can be seen from the Figure 5.16A that with the increase of temperature there is no significant shift in the depth and position of the optical matching point. This indicates that size polydispersity does not change significantly with increase of temperature, which is consistent with the result obtained by Arleth et al<sup>100</sup>. The temperature dependence of size polydispersity found by Kotlarchyk et al<sup>105</sup> may be attributed to the shape fluctuations of droplet. Therefore, W/O - MEs were investigated at temperatures in the range  $25^\circ\text{C} < \alpha < 37.5^\circ\text{C}$  in order to investigate the effect of temperature on shape of droplets.

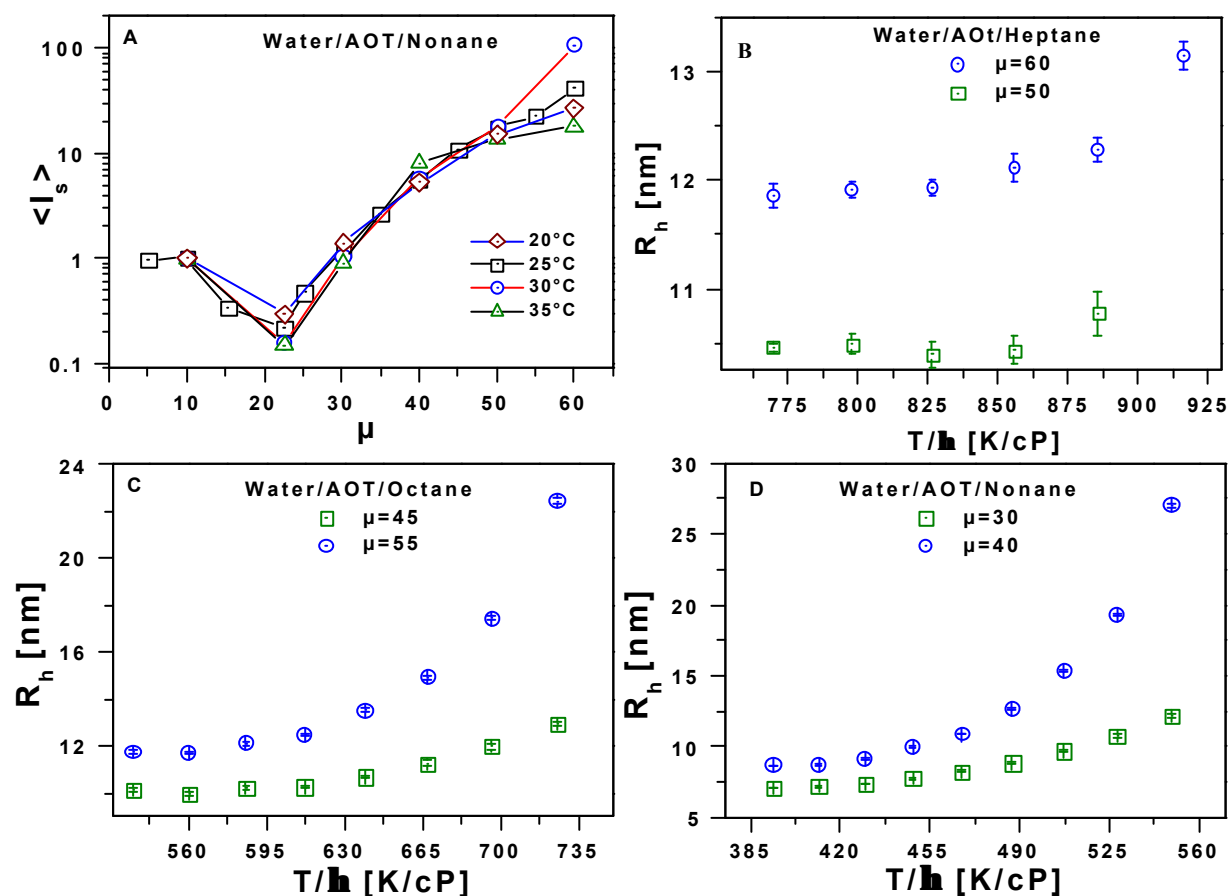


**Figure 5.16.** (A) Experimental data points for the relative scattered Intensity as a function of the molar ratio  $\mu$  at different are shown in figure A. Plots of the hydrodynamic radius  $R_h$  of the ME droplet obtained from DLS versus  $T/h$  are shown in figure B, C and D.

After correcting the temperature dependence of the viscosity of solvent. Hydrodynamic radius  $R_h$  is obtained from first cumulant as described in the Section 5.1.3 with increasing temperature. Hydrodynamic radius  $R_h$  versus normalized temperatures is plotted in Figure 5.16. In systems where no structural changes occur the radii should be independent of the temperature, as predicted by the Stokes-Einstein Eq. (3.44). As shown in Figure 5.16A, for MEs investigated, this is clearly not fulfilled. It is interesting that at temperatures up to 10°C above the lower solubilization temperatures  $T_1$  of AOT W/O - MEs in *n*-alkane oil ( $T_1 = 22.2$  for ME-Heptane,  $T_1 = 17.3$  for ME-Octane,  $T_1 = 14.5$  for ME-Nonane)<sup>99</sup> nearly no change in the radii occur. The results obtained for AOT-water- *n*-alkane system using time-resolved luminescence quenching technique<sup>47</sup> and for the  $C_{12}E_5$  – water- decane system using nuclear magnetic resonance (NMR) techniques.<sup>131,132</sup> and for AOT-water-isooctane system using small angle X-ray scattering<sup>133</sup> proved that a transition occurs from spherical droplets to ellipsoids<sup>131</sup> and cylindrical or rodlike<sup>132</sup> with increasing temperature. Their observation is consistent with our results that with increase of temperature aggregation take place in the direction of vanishing spontaneous curvature, leading to structural change from spherical droplet to ellipsoid. For such case, diffusion coefficient of the MEs at infinite dilution can be obtained by attaching a correction term concerning shape,  $F(\rho)$ , to the Stokes-Einstein and Perrin equations<sup>134</sup> of the form

$$(5.16) \quad D_{spheroid} = \frac{k_B T}{6\pi\eta b} F(\mathbf{r})$$

with  $b$  is the length of the short axis and  $\mathbf{r}$  is the axial ratio ( $\rho=a/b$ , where  $a$  is the length of the long axis).

Using the constant-area-to-enclosed-volume constraint, one can write expression for diffusion coefficient of the prolate MEs at infinite dilution as<sup>132</sup>

$$(5.17) \quad D_{prolate}^0 = \frac{k_B T}{6\pi\eta R} \frac{2 \ln(\mathbf{r} + \sqrt{\mathbf{r}^2 - 1})}{\sqrt{(\mathbf{r}^2 - 1)/\mathbf{r}^2} + \mathbf{r} \arccos(1/\mathbf{r})}$$

For oblate MEs

$$(5.18) \quad D_{oblate}^0 = \frac{k_B T}{6\pi\eta R} \frac{2 \arctan(\sqrt{\mathbf{r}^2 - 1})}{\sqrt{(\mathbf{r}^2 - 1)_+} \arccos h(\mathbf{r})/\mathbf{r}}$$

where  $R$  is the radius of the sphere.

The axial ratio of ellipsoids calculated from the diffusion coefficient obtained from cumulant fitting of DLS data of droplet using Eq. (5.17) and (5.18) assuming the MEs to grow from spheres at 25°C (In all cases up to  $T=25^\circ\text{C}$ , MEs do not change radii with in experimental accuracy i.e., no structural changes occur till temp  $T=25^\circ\text{C}$ ) to spheroids. Values of the axial ratio are given in Table 5.6. The small difference between the prolate and oblate models is not significant because of the applied approximations in evaluating the data. Figure 5.17 shows the obtained prolates axial ratio as a function of temperature for the systems water/AOT/*n*-heptane ( $\mu=60$ ), water/AOT/*n*-octane ( $\mu=45$ ) and water/AOT/*n*-nonane ( $\mu=30$ ). It has been

concluded that prior to the upper two-phase boundary  $T_u$  (haze point for water/AOT/*n*-heptane = 62.4°C, water/AOT/*n*-octane = 55.3°C and water/AOT/*n*-nonane = 47.3°C),<sup>99</sup> there is a growth of MEs limited to an axial ratio as shown in Table 5.6.

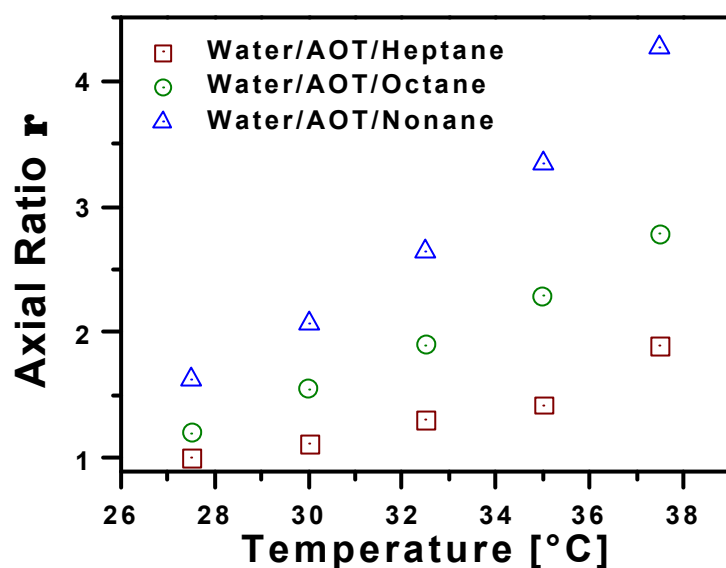


**Figure 5.17** Average axial ratios representing growth of ME droplet from spheres to spheroids as obtained from DLS.

Axial ratio increases with increase of temperature for temperature  $T > 27.5$  and longer the alkane chain the larger is the axial ratio. This temperature and alkane chain length dependence of the shape of the droplets can be explained by temperature and alkane chain length dependent of the spontaneous curvature of surfactant film resulting in preferred droplet shape at given temperature. Increasing the temperature above the lower solubilization temperature favors less negative spontaneous curvature (surfactant polar head groups on the interior of the aggregate and the apolar tails on the exterior surface, defined here as negative curvature) and often observed near the phase inversion temperature, ME has a bicontinuous structure with zero net surfactant film curvature. It is known that due to reduced solubility of the surfactant in longer-chain oils,<sup>135</sup> higher chain-length alkane oils shift solubilization temperature to lower temperatures (lower solubilization temperature for water/AOT/*n*-heptane, water/AOT/*n*-octane and water/AOT/*n*-nonane are 22.5°C, 17.3°C and 14.5°C respectively).<sup>99</sup> Therefore at constant temperature, longer the alkane chain the smaller will be the negative curvature hence larger the axial ratio.

axial ratios $r$	water/AOT/ <i>n</i> -heptane T(°C)					water/AOT/ <i>n</i> -octane T(°C)					water/AOT/ <i>n</i> -nonane T(°C)				
	27.5	30	32.5	35	37.5	27.5	30	32.5	35	37.5	27.5	30	32.5	35	37.5
<b>Prolates</b>	1	1.12	1.30	1.43	1.90	1.20	1.55	1.90	2.29	2.78	1.63	2.08	2.65	3.35	4.27
<b>Oblates</b>	1	1.12	1.30	1.41	1.83	1.20	1.53	1.84	2.29	2.78	1.60	1.99	2.65	3.35	4.27

**Table 5.6** Axial ratio obtained from diffusion data.

## 5.2 Characterization of Pharmaceutical MEs

The selection of the components for MEs suitable for pharmaceutical interest involves a consideration of their toxicity and, if the systems are to be used topically, their irritancy and sensitizing properties. There have been extensive studies done on MEs using cosurfactant in the last few decades. As discussed in introduction, the benefit of a cosurfactant such a short chain alcohol is not available. Therefore, particular interest of the present study is the formulation of MEs consisting of pharmaceutical acceptable components and hence are suitable as topical drug delivery vehicles, free of the irritancy effects normally associated with medium chain length alcohols. In detailed phase studies of these systems,<sup>136,137</sup> it has been shown that one of the mixture of two nonionic surfactants function as a cosurfactant in a similar manner to that of an alcohol in a traditional ME. Non-ionic surfactants are conveniently classified on an empirical scale known as hydrophilic-lipophilic balance (HLB) which runs from 1 to 20. Selecting a suitable ME system for drug delivery, it is important to know something about the physico-chemical properties of ME such as drug solubility, area of ME in the phase diagram and the resulting size of ME. Only few methods are available to investigate the physico-chemical properties of a ME, the most widely used are scattering techniques or nuclear magnetic resonance (NMR) self diffusion measurements. In this work, experimental approach has been based upon the use of scattering techniques and MEs are investigated in the so-called  $L_2$  phase corresponding to a ME of surfactant-coated spherical droplets of oil or water dispersed in a homogeneous medium of hydrophilic phase or oil phase. The droplet size and interdroplet interactions of ME droplets were estimated using the results obtained from model ternary AOT-MEs. The size and stability of ME is highly dependent on the concentration of each constituent solubilized. Therefore, MEs having different concentrations of their constituent were also investigated in this study.

### 5.2.1 Interdroplet Interaction and Droplet Size of O/W - MEs of Pharmaceutical Interest

DLS technique was used to describe the interdroplet interaction on the stability of MEs. As shown in the Section 5.1.3, scattering techniques collectively suffer from the disadvantage that in order to obtain a reliable estimate of droplet size, measurement should be made at a range of low-disperse-phase volume fractions and should be extrapolated to infinite dilution in order to avoid the problems encountered as a result of interdroplet interactions (see Section 5.1.3). In common to many MEs, MEs for dermal use studied in this work could not diluted to very low-disperse-phase volume fraction without phase separation. Consequently to allow meaningful calculation of droplet size at finite droplet concentration, conventional light scattering or neutron scattering or x-ray diffraction methods can not be used without making

assumptions about the nature of the interdroplet interaction. Nevertheless it appears that the dominant mechanism in determining droplet size is the tendency of the surfactants to form a “monolayer” around the droplets in such a way as to keep the area per surfactant molecule roughly constant. As discussed for model ternary AOT-MEs in the Section 5.1.3, dilution procedure were used (in the area of phase diagram where clear and transparent MEs were obtained) to determine the nature of interdroplet interactions. From the total interaction energy, it is possible to derive a criterion for the stability of MEs too.<sup>130</sup>

MEs investigated in this section consist pharmaceutical oils, a blend of a high and a low HLB surfactant, and a hydrophilic phase (propylene glycol/water). These MEs were developed in our research group using pharmaceutically acceptable components. The basic ME consists of a quaternary mixture of oil 5 wt%, Poloxamer 331/Tagat<sup>®</sup> O2 (3:2) 20 wt% and PG/H<sub>2</sub>O (2:1) 75 wt%. This basic ME was diluted with the continuous phase keeping constant the molar ratio of dispersed phase(oil) and surfactants (Poloxamer 331 and Tagat<sup>®</sup> O2) at  $\mu = 1.8$  to preserve a constant droplet radius.

### 5.2.1.1 DLS Results

For each sample, the diffusion coefficients have been deduced from bi- exponential fit from the normalized field autocorrelation function  $g(\tau)$  as described in the Section 4.1. Striking feature of these experiments was splitting of diffusion coefficient at range of volume fraction  $\phi \sim 0.10-0.35$  as observed in model ternary AOT-MEs at volume fraction  $\phi > 0.2$ . Because of phase separation at low and at high volume concentration of dispersed phase, it was not possible to freely vary the volume fraction of the dispersed phase as it was in the case of AOT-MEs. Stable MEs were observed in the range of volume fraction of dispersed phase,  $\phi \sim 0.10-0.35$ . Simple calculations, similar to those at the beginning of the Section 5.1.3, show that for the small-droplet radius  $\sim 10$  nm (as observed for our system),<sup>3,3</sup> these experiments performed well into the hydrodynamic regime  $q^{-1} > r_{\text{mean}}$  and  $\tau_c > \tau_l$ . In the hydrodynamic regime, one expects the correlation function to be the sum of two exponentials, the fast one representing collective diffusion and the slow one representing self diffusion for dense polydisperse and interacting systems. The most likely interpretation of these results seems to be polydispersity and interaction of the droplets, which would lead to the observation of coherent (number density fluctuation) and incoherent (Polydispersity fluctuation) scattering. As shown in Figure 5.18, the diffusion coefficient  $D_s$  due to concentration fluctuations decreases in value with increasing  $\phi$  in accordance with the expectation that the mobility of a single droplet will be severely hindered as the density of droplets increases, whereas  $D_c$  arises from mutual diffusion of ME droplets shows a small increase. This is consistent with the interpretation that found in MEs described in the Section 5.1.3 for model ternary AOT-MEs.

Both diffusion coefficients represented in Figure 5.18 should fit to the same value,  $D_0$ , a  $f \rightarrow 0$ , so the use of Bi- Exponential methods of data analysis permits to estimate the droplet size quite accurately.  $D_0$  can be identified with  $D_{c,s}$  when  $f \rightarrow 0$  (see Figure 5.18, with in experimental error  $\pm 5\%$ , both diffusion coefficients give same  $D_0$ ). Hydrodynamic radius  $R_h$ , which is supposed to consist of the oil core, a surfactant film and perhaps some solvent molecules too, was calculated using  $D_0$  from Eq. (3.44) and is listed in Table 5.7. It was observed that  $R_h$  is comparatively independent of kind of oil which is consistent with the result.<sup>3</sup>

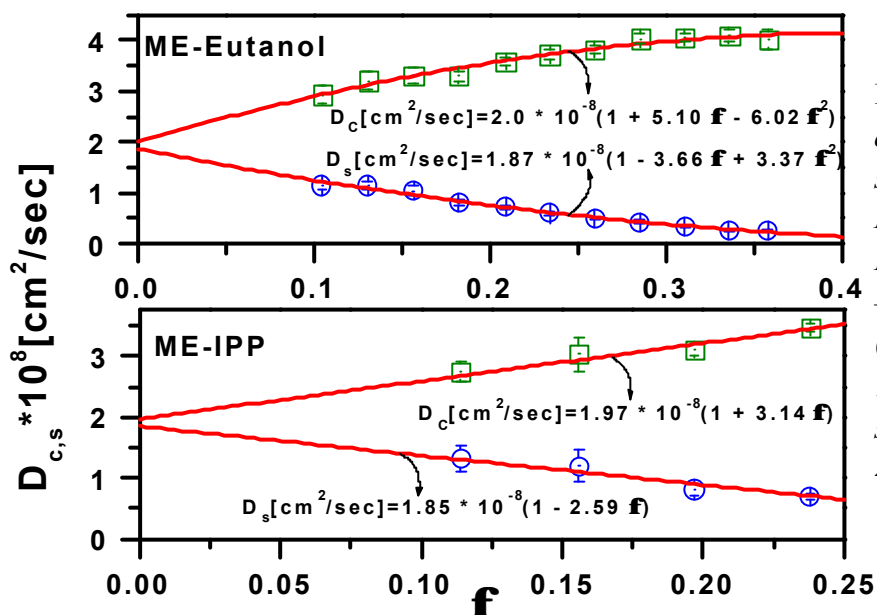


**Figure 5.18** Volume fraction dependence of diffusion ( $D_s$ -self and  $D_c$ -collective) in ME-Eutanol (Eutanol - Poloxamer 331 / Tagat<sup>®</sup> O2 - Water / PG) and ME-IPP (IPP - Poloxamer 331 / Tagat<sup>®</sup> O2 - Water / PG) systems with  $\mu = 1.5$  at 25°C.

We now consider in more detail the variation of  $D_c$  and  $D_s$  obtained from DLS with the volume fraction. The decrease in  $D_s$  fits satisfactorily to a quadratic Eq. (3.47) with  $a_1^s = -3.66$  and  $-2.59$  for ME-Eutanol, and ME-IPP respectively. The increase in  $D_c$  fits satisfactorily to a quadratic Eq. (3.47) with  $a_1^c = 5.1$  and  $3.14$  for ME-Eutanol, and ME-IPP respectively (see Figure 5.18 for quality of fit). If we assume that the droplet size does not vary significantly over the concentration range then these results can be compared with theoretical predictions to first order in the volume fraction. If one assumes that the suspended droplets are hard sphere, one then obtains  $(a_1^c)^{HS}$  &  $(a_1^s)^{HS} = 1.56$  and  $-2.01$  respectively.<sup>49</sup> This result is clearly not comparable with the experimental value. A possible explanation for the observed difference for  $a_1^c$  and  $a_1^s$  is to assume the presence of the effective interaction except hard sphere force between suspended droplets. For studied systems,  $\mathbf{d}a_1^{c,s} = a_1^{c,s} - (a_1^{c,s})^{HS}$  is positive that indicates that droplets interacting via hard sphere interaction with perturbation of repulsive potential (see Section 5.1.3.3 for the detail).

### 5.2.1.2 Effect of Proposed Interdroplet Interaction on the Stability of O/W – MEs of Pharmaceutical Interest

The origin of the observed interdroplet interactions is thought to be due to the steric and hydrational forces, which arise from the loss of entropy when adsorbed hydrated chains of nonionic polyether surfactants intermingle on close approach of two similar droplets.<sup>138,139,140,141</sup> Hydration force, which is essentially responsible for observed interactions, which originate from the increased structuring of the water molecules around the head group of the surfactant molecules. Assume that interdroplet interactions have pair wise form so the pair interaction potential between the droplets, immersed into the medium (continuous phase) can be written as Eq. (3.70).

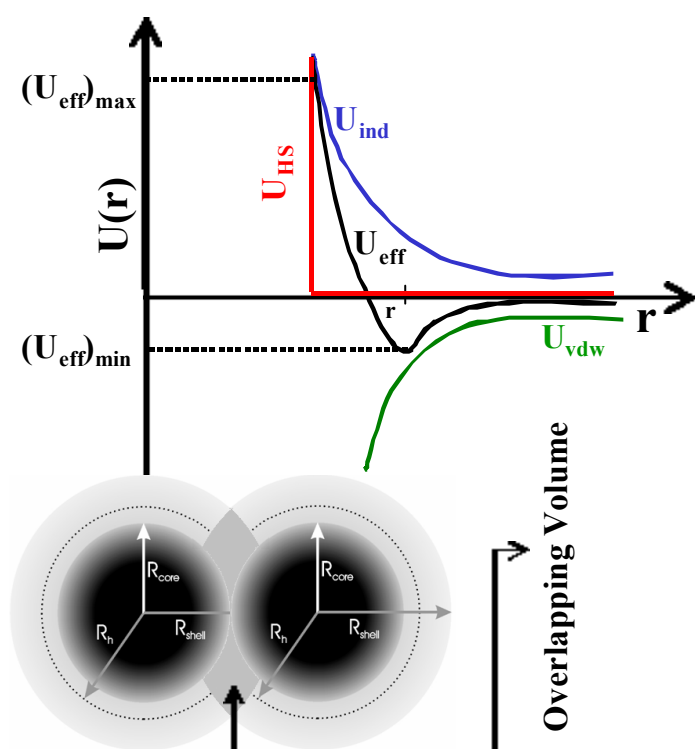


**Figure 5.19** Different contributions to the effective interaction potential. The meaning of the various radii and interaction potential is explained in the text.

The direct interaction  $U_{dir}$  between droplets that does not depend explicitly on bound solvent molecules which may migrate with droplet. Therefore, hard sphere  $U_{HS}$  and dispersion  $U_{dis}$  forces gives the dominant contribution to direct interaction  $U_{dir}$  in the case of non-ionic micelles.

For our present purpose, we do not believe that the specific form of  $U_{dis}(r)$  is essential. We assume simple van der Waals force that is given as<sup>138</sup>

$$(5.19) \quad U_{dir}(x) = -\frac{A}{12} \left\{ (x^2 + 2x)^{-1} + (x^2 + 2x + 1)^{-1} + 2 \ln \left[ \frac{x^2 + 2x}{x^2 + 2x + 1} \right] \right\}$$

where  $x = (r - 2R_{h,s})/2R_{h,s}$  is the surface to surface separation in units of  $2R$  and  $A$  is a Hamaker constant.

Finally, indirect  $U_{ind}$  should involve the solvent degree of freedom. This indirect interaction should correspond to repulsive force.<sup>130</sup>

$$(5.20) \quad U_{ind} = U_0 \exp\left[-\frac{(x/\Lambda)}{(1+x)}\right]$$

where  $\Lambda$ , which is a measure of the width of the shell of structured water, decreases with increasing temperature, so that attractive interaction becomes more effective and possibility of phase separation occurs at high temperature.  $U_0$  is the change in energy due to removal of  $H_2O$  (solvent) molecules from overlapping volume.  $U_0$  is estimated for our system is  $\sim 3.6 \times 10^4 k_B T$  (for detail procedure of calculation see Appendix C).

The effects of interdroplet interactions on observed droplet diffusivities have been investigated by Janich et al.<sup>122</sup> Using the generalized Stokes-Einstein-Equation with the hydrodynamic correction of Felderhof<sup>92</sup> and a pair potential from DLVO theory,<sup>130</sup> they obtained quantitative fits to their measurements of dihydroxy bile salt micelles. Basically, the same procedure is used in this work to estimate the parameters that characterize the interdroplet interactions. In this work proposed model effective potential shown in Figure 5.19 is used instead of pair potential using DLVO theory used by Janich et al.<sup>122</sup>

ME	$D_0 \times 10^8$ [cm <sup>2</sup> /sec]		$R_h$ [nm]	$U_0 \times 10^{-4}$ [k <sub>B</sub> T]	<b>L</b>	$U_{eff}$ [k <sub>B</sub> T]	$t_{f,U_{eff}=0}$ 10 <sup>5</sup> [sec]	<b>W</b>	<b>s<sub>s</sub></b>
	From <b>D<sub>c</sub></b>	From <b>D<sub>s</sub></b>							
<b>Eutanol</b>	2.00	1.87	~10	3.59	0.024	172	2.8	10 <sup>65</sup>	~0.22
<b>IPP</b>	1.97	1.85	~10	3.60	0.022	172	2.8	10 <sup>65</sup>	~0.20

**Table 5.7** The size, polydispersity index  $s_s$ , and interaction energy and the related parameters of the ME droplets at temperature 25°C (see text for details), errors are smaller than  $\pm 3\%$  for radii and  $\pm 10\%$  for polydispersity index  $s_s$ .

All the experimental data for  $D$  have been reproduced by means of the parameters which define the interaction potential, that is the Hamaker constant  $A$ , the width of the layer of structured water  $L$  and the change in energy due to removal of water molecules  $U_0$ . The change in energy  $U_0$  due to removal of water molecules from the overlapping volume is calculated and detailed method for calculation is given in Appendix C. These values are listed in Table 5.7. A complication arises in that the value of the Hamaker constant is not known

and cannot be easily estimated. Fortunately, the results are not strongly dependent on the value of the Hamaker constant since the repulsive part of the potential is dominant. So that in present fitting  $A = 25 \text{ k}_B T$  was used, which is a well chosen value for the stability of colloids.<sup>142</sup> Both integrals in  $K_I$  &  $K_H$  [see Esq. (A.7)] cannot be solved without a lower cut off  $x_L > 0$ , because the attractive part of potential diverges. The generally accepted value  $x_L = 0.04$ , which corresponds to the expected stern layer thickness, has been used.<sup>142, 122</sup> An additional complication arises in estimating the volume fraction,  $\phi$ , for the ME. Partition coefficients for surfactants are not known. It was assumed that the surfactant was completely incorporated into the droplet phase. For this assumption, the volume of the dispersed phase is just equal to the sum of the volumes of the surfactants and the added oil. Thus, all experimental data were fitted by means of only one free parameter which defines the interaction potential that is width of structured water  $\Lambda$ . The best fitted values are listed in Table 5.7.

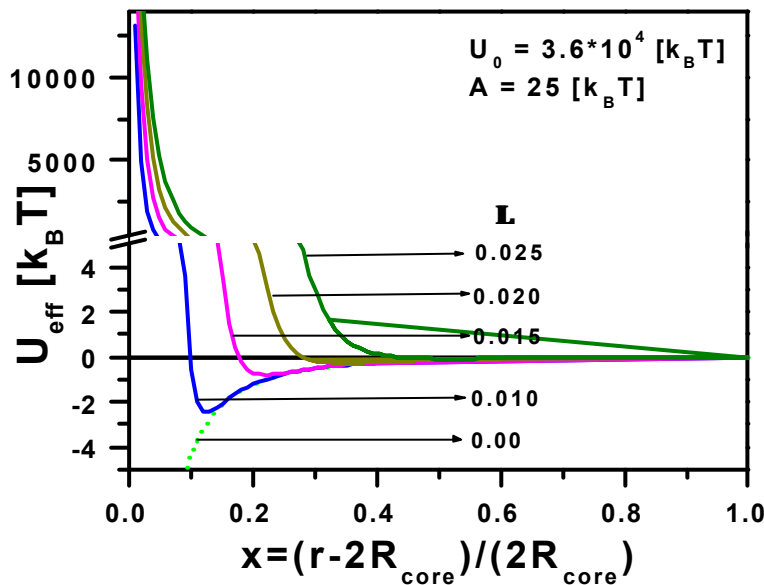


**Figure 5.20** Behavior of the interaction potential as a function of the width of the shell of structured water  $L$ .

Figure 5.20, presents the proposed interaction potential  $U_{\text{eff}}$  for five typical cases relevant to the understanding of ME stability. It was found that the shell of structured water is almost independent for kind of oil as it is expected for same set of surfactants and hydrophilic phase. The combination of repulsive forces and the attractive van der Waals interactions may produce a significant potential energy barrier between the primary maximum  $(U_{\text{eff}})_{\text{max}}$  at  $r = 2R_{\text{core}}$  and the shallow secondary minimum  $(U_{\text{eff}})_{\text{min}}$  at a separation distance  $r$  somewhat larger than the  $2R_{\text{core}}$  (see Figure 5.20). Let us review the situations relevant to our experiment in terms of the parameters that characterize the potential.

- I. *A large positive  $(U_{\text{eff}})_{\text{max}}$  and a small  $(U_{\text{eff}})_{\text{min}}$* : In this case the energy barrier prevents the droplets from coming close enough and the colloid is stable.
- II. *A significant and positive  $(U_{\text{eff}})_{\text{max}}$  and a deep secondary minimum  $(U_{\text{eff}})_{\text{min}}$* : In this case, when the droplets reach separations corresponding to separation minimum, the droplet stick together and flocculation occurs.

- III. *A low value of  $(U_{eff})_{max}$  and a deep secondary minimum  $(U_{eff})_{min}$* : This corresponds to an intermediate situation, when the system evolves towards an irreversible coagulation starting from droplets that colloid and stick together, i.e., individual droplets are added one at a time to a growing cluster.
- IV. *Finally in the absence of repulsion, every collision give rise to irreversible coagulation and phase separation will occur.*

We observed  $(U_{eff})_{max}$  practically infinite at  $r = 2R_{core}$  due to hard sphere potential (see Figure 5.20). As shown in Figure 5.20, repulsive part of  $(U_{eff})_{min}$  increases with increasing  $\Lambda$  value. For fitted value of  $\Lambda$  ( $\sim 0.02$ ),  $(U_{eff})_{min}$  is practically zero indicating that our systems follow case I.

Rapid coagulation time  $t_{f,U_{eff}=0}$  and ratio between rapid and slow coagulation time  $W$ , which is the measure of colloidal stability were also calculated using interaction potential (see Appendix C). It was found that observed effective potential diminishes the velocity of coagulation by a factor  $W \sim 10^{65}$ . Factor  $W$  also represents the ratio between rapid and slow coagulation will have to surpass  $10^5$  for diluted and  $10^9$  for concentrated colloids to give them a reasonable (week or month) stability. This stability results are consistent with observed infinite stability (more than three years) of our MEs.

A value of size polydispersity index  $\sigma_s$  can be obtained from relative amplitude of the slow decay mode using theoretical results,<sup>46</sup> which are valid for narrow size distribution. A reasonable theoretical fit for size polydispersity:  $\sigma_s = 0.22$  and  $0.20$  for ME-Eutanol and ME-IPP respectively were obtained, which are in the agreement with values expected theoretically<sup>108,109</sup> for stable MEs.

## 5.2.2 Behavior of each constituent solubilized in MEs of Pharmaceutical Interest

In pharmacy, MEs have been examined as good vehicles for transdermal application. The advantage of MEs as drug delivery vehicles is improvement of drug delivery of both lipophilic and hydrophilic drugs, compared to conventional vehicles, as well as the potential for enhanced absorption due to surfactant-induced permeability changes, depending on the constituents used for the ME vehicle.<sup>143,144,145,146,147,148,149,150</sup> Unfortunately, as most of the work reported in the literature has used pharmaceutical unacceptable ingredients to formulate the ME, there is a need for the development and study of systems suitable for pharmaceutical interest. In the present section, stable O/W and W/O - MEs of pharmaceutical interest were formulated consisting of an oil (IPP or Eutanol or oleic acid or IPM or MCT), a blend of a low (Poloxamer 331 or Span<sup>®</sup> 20) and a high (Tween<sup>®</sup> 80 or Tagat<sup>®</sup> O2) HLB, and an aqueous phase (PG/water or water/DMSO). The small size of the dispersed droplets of MEs, (typically less than 100 nm), necessitates the use of scattering techniques such as neutron scattering,

light scattering. In the present section, DLS and SANS measurements have been used to determine whether or not a ME is indeed produced. To allow meaningful calculation of droplet size, it is necessary to correct scattering results in high concentration regions for interdroplet interactions. An appropriate model is then used to correct the results for droplet-droplet interaction. We used model for interaction correction reported in our paper.<sup>3</sup>

### 5.2.2.1 O/W - MEs of Pharmaceutical Interest

O/W - ME		Oil	Polox. 331/ Tween <sup>®</sup> 80	Polox. 331/ Tagat <sup>®</sup> O2	Water/PG	Drug (Lidocaine)
Series 1 (Micelles with different ratios of water/PG)	1	-	20 (3:2)	-	80 (1:0)	-
	2	-	20 (3:2)	-	80 (4:1)	-
	3	-	20 (3:2)	-	80 (2:1)	-
	4	-	20 (3:2)	-	80 (1:2)	-
	5	-	20 (3:2)	-	80 (1:4)	-
Series 2 (ME with different amounts of inner phase)	1	0 (IPP)	20 (3:2)	-	80 (1:2)	-
	2	1 (IPP)	21 (3:2)	-	78 (1:2)	-
	3	2.5 (IPP)	20.5 (3:2)	-	77 (1:2)	-
	4	4 (IPP)	20 (3:2)	-	76 (1:2)	-
	5	6 (IPP)	19.8 (3:2)	-	74.2 (1:2)	-
	6	7.5 (IPP)	19.5 (3:2)	-	73	-
Series 3 (ME with drug)	1	5 (IPP)	20 (3:2)	-	80 (1:2)	0
	2	5 (IPP)	20 (3:2)	-	70 (1:2)	5
	3	5 (IPP)	20 (3:2)	-	65 (1:2)	10
Series 4 (ME with different kinds of oil)	1	5 (OA)	20 (3:2)		75 (1:1)	-
	2	5 (IPP)		20 (3:2)	75 (1:2)	-
	3	5 (EU)		20 (3:2)	75 (1:2)	-
	4	5 (IPM)	20 (3:2)		75 (1:2)	-
	5	5 (MCT)		20 (3:2)	75 (1:2)	-

**Table 5.8** The composition of the MEs studied (content in wt %).

Stable O/W - MEs, which are of pharmaceutical interest, were developed in our research group. The existence of the ME field was monitored by the corresponding phase diagram. The ME phase was identified as area in the phase diagram where clear and transparent formulations are obtained based on visual inspection of many samples. Detailed description of phase diagram is presented elsewhere.<sup>136,137</sup> For the investigations of developed O/W - MEs, four series were prepared. The composition of the MEs used to investigate are summarized in

Table 5.8. The ITCF of each sample was investigated at different scattering angles between 70 and 100°. Correlation functions corresponding one set of experimental parameters have been measured five times and the ITCF's used for fitting are averaged over these five measurements. The collective diffusion coefficient has been deduced from a bi-exponential fitting procedure from the normalized field auto correlation function  $g(\tau)$  and averaged over the angles (see Chapter 4). To get the free diffusion coefficient of droplets, measured diffusion coefficient was corrected assuming the presence of hard-sphere plus repulsive interactions arise due to structuring of water around the droplet as discussed in the Section 5.2.1. The hydrodynamic radius  $R_h$  was calculated from free diffusion coefficient using Eq. (3.44).  $R_h$  is the overall droplet radius including any associated solvent molecules which migrates with translating droplet.

### 5.2.2.1.1 Series 1: O/W - MEs with Different Ratios of Water/PG

In first series of ME, basic studies were carried out on micellar solution without oil, in order to access the influence of PG. Table 5.9, summarizes the DLS results obtained for micelles containing different weight ratio of water and PG. First noticeable thing about the results obtained is a definite decrease in aggregate size after small incorporation of PG in comparison to the parent micelle (Without PG). Further gradual increase in the amount of incorporation, shows no change in droplet size with in experimental error. Reduction in size due to small incorporation of PG suggests that PG penetrate into the interfacial film of the dispersed droplet, lowering the interfacial tension, causing a transformation of asymmetric parent micelle to spherical aggregate, resulting in smaller droplet.

O/W - ME	Series 1-1	Series 1-2	Series 1-3	Series 1-4	Series 1-5
$\eta$ [H <sub>2</sub> O/PG] (m Pas)	0.894	1.83	3.05	9.5	15.38
$R_h$ [nm]	9.14	7.51	7.16	6.98	7.34

**Table 5.9** DLS results for O/W - MEs series 1. Errors are smaller than  $\pm 5\%$  for radii.

### 5.2.2.1.2 Series 2: O/W - MEs with Different Amounts of Oil (Inner Phase)

In second series of MEs, effect of the different concentrations of inner phase (IPP oil) was investigated. Experimentally measured hydrodynamic radius  $R_h$  of these systems are shown in Figure 5.21. As expected, incorporation of oil causes an increase in droplet radius. The systems were able to solubilize up to 7.5% oil without phase separation.  $R_h$  varied as molar oil to surfactant ratio is shown in Figure 5.21. For a blend of high and low HLB surfactant stabilized oil droplets, it has been found, that there is a linear relationship between  $R_h$  and  $\mu$ ,

which is consistent with packing consideration results obtained from model AOT-MEs. Linear relationship of  $R_h$  and  $\mu$  can be expressed by empirical formula

$$R_h \text{ (nm)} = 7.25 + 2.39 \mu$$

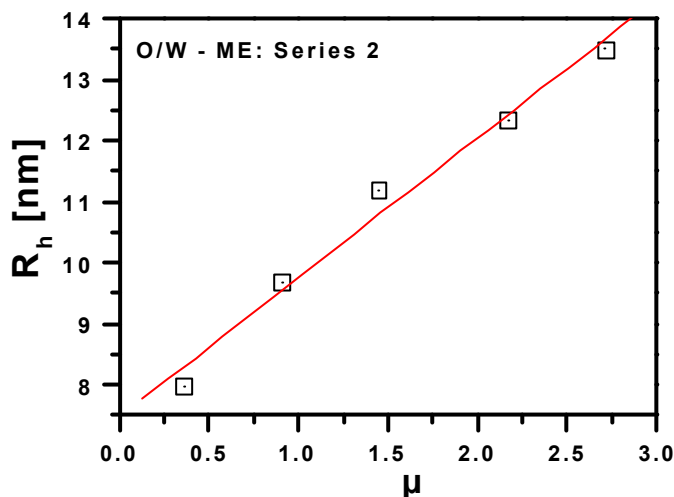


**Figure 5.21** Droplet size of MEs series 2 versus molar ratio of oil and surfactants  $\mu$ , errors are smaller than  $\pm 5\%$  for radii

### 5.2.2.1.3 Series 3: O/W - MEs with Drug Incorporated into the Inner Phase

In third series of ME, effect of drug incorporation on droplet size were investigated.

O/W - ME	Series 3-1	Series 3-2	Series 3-3
$f$	0.26	0.30	0.35
$R_h$ [nm]	7.19	13.82	17.11

**Table 5.10** DLS results for O/W - MEs series 3. Errors are smaller than  $\pm 5\%$  for radii.

Droplet size obtained from these systems were listed in Table 5.10. As expected, the incorporation of drug causes an increase in droplet radius.

### 5.2.2.1.4 Series 4: O/W - MEs with Different Kinds of Oils

In this section, the droplet size of these MEs was characterized by means of DLS as well as by SANS. Furthermore, different size parameters obtained by DLS and SANS experiments were compared and discussed.

#### 5.2.2.1.4.1 DLS Results

DLS yields hydrodynamic radius  $R_h$  which is supposed to consist of the oil core and a strongly bounded surfactant film perhaps containing some solvent molecules such as PG too.  $R_h$  calculated for each samples are listed in Table 5.11. Very small droplet sizes ( $\sim 10$  nm) were observed for our measured samples. With the exception of oleic acid (OA) no remarkable difference is found between Eutanol or IPP or IMP as oils of comparable molecular volume. Probably, the angular structure of oleic acid or the different PG/D<sub>2</sub>O ratio causes the greater radii. It can be easily seen that there is definite decrease in droplet size for MEs with larger molecular volume oil ( $V_o$ ) (MCT) when compared to the smaller molecular volume oils (IPP, IPM, OA). Reduction in size observed in the presence of the oils larger in molecular volume suggests that the larger volume oils tend to locate in the centre of the surfactant aggregate, and the smaller molecular volume oils, at least partially, locate in the interfacial surfactant region. This result is consistent with the results obtained from Warisnoicharoen et al.<sup>151</sup>

O/W - ME	Series 4-1	Series 4-2	Series 4-3	Series 4-4	Series 4-5
$V_o$ [Å]	510	563	578	510	890
$R_h$ [nm]	10.9	9.58	9.01	9.48	8.43
$s_s$	0.25	0.16	0.18	0.14	0.27

**Table 5.11** DLS results for O/W - MEs series 4. Errors are smaller than  $\pm 5$  % for radii.

### 5.2.2.1.4.2 SANS Results

To elucidate the droplet size as well as the thickness of the surfactant shell, SANS experiments were conducted on the MEs having either oleic acid or IPP or Eutanol as inner phase. The collected data were fitted with a model for polydisperse spherical droplets with a core shell model [see Eqs. (3.60), (3.63) and (3.69)] as well as with the Guinier approximation [see Eq. (3.64)]. Core shell model along with profile of scattering length density which describes the interaction of neutron beam with the material per unit volume is shown in Figure 5.22. Assuming that the droplet core only consists of oil, the shell only of surfactants and the surrounded medium only of PG/D<sub>2</sub>O, the SLD of core, shell and surrounded medium necessary for fitting the scattering data were calculated to  $\rho_{\text{Oleic Acid}} = 0.235 \cdot 10^{14} \text{ m}^{-2}$ ,  $\rho_{\text{IPP}} = -0.727 \cdot 10^{13} \text{ m}^{-2}$ ,  $\rho_{\text{Eutanol}} = -0.327 \cdot 10^{14} \text{ m}^{-2}$ ,  $\rho_{\text{PG/D}_2\text{O } 1:1} = 3.226 \cdot 10^{14} \text{ m}^{-2}$ ,  $\rho_{\text{PG/D}_2\text{O } 2:1} = 2.112 \cdot 10^{14} \text{ m}^{-2}$ ,  $\rho_{\text{Poloxamer/Tween}^{\text{®}} 80} = 0.5145 \cdot 10^{14} \text{ m}^{-2}$ ,  $\rho_{\text{Poloxamer/Tagat}^{\text{®}} \text{O}_2} = 0.468 \cdot 10^{14} \text{ m}^{-2}$ . An exchange of loosely bounded H and D atoms is incorporated.  $R_{\text{core}}$ ,  $R_{\text{shell}}$  and SLD of shell as well as  $\sigma_s$  are independent fitting parameters. SLD of shell obtained from fitting are slightly larger than that expected  $\rho_{\text{Poloxamer/Tween}^{\text{®}} 80}$  or  $\rho_{\text{Poloxamer/Tagat}^{\text{®}} \text{O}_2}$ , suggesting the some amount of D<sub>2</sub>O is penetrated inside the shell. Best fitting obtained using two methods of analyzing the data is shown in Figure 5.23.

O/W - ME	$R_{\text{core}}$ [nm]	$R_{\text{shell}}$ [nm]	$R_g$ [nm]	$s_s$	$R_g/R_h$
Series 4-1	9.87	13.11	7.90	0.23	0.72
Series 4-2	7.75	11.49	6.87	0.17	0.71
Series 4-3	7.98	10.81	6.65	0.21	0.74

**Table 5.12** SANS results for O/W - MEs series 2. Errors are smaller than  $\pm 5\%$  for radii.

Two values for the radius  $R_{\text{core}}$  and  $R_{\text{shell}}$  obtained from the fitting of SANS data with polydisperse core shell model yields are shown in Figure 5.22. The first corresponds to the size of oil droplet, the second to the distance between centre of droplet and a position in the surfactant film where the difference in SLD has its maximum. The results from the fit of SANS curves are summarized in Table 5.12. From SANS studies no remarkable difference is observed between investigated oil except oleic acid, too. As expected, the outer radius  $R_{\text{shell}}$  incorporates the loosely bounded surfactant molecules and is substantially bigger than  $R_h$ . The outer diameter determines the smallest possible distance between two droplets, because of its strong influence to the structure factor. The hydrophilic group of Tween<sup>®</sup> 80, Tagat<sup>®</sup> O2 and Poloxamer 331 is polyoxyethylene (see Figure D.10, Figure D.12 and Figure D.13). This is

formed by the polymerization of ethylene oxide (EO). The length of polyoxyethylene chain is  $1.8 \text{ \AA}$  per monomer at a degree of polymerization from 20 to 40 and  $3.5 \text{ \AA}$  per monomer at a degree of polymerization less than 20<sup>152</sup>. Tagat<sup>®</sup> O2, Tween<sup>®</sup> 80 and Poloxamer 331 have 20, 20 (maximum possible when  $w=20$  and  $x=y=z=0$ ) and 7 monomer per molecule in larger chain respectively. Thus length of hydrophilic chain is 3.6 nm, 3.6 nm and 2.45 nm for Tagat<sup>®</sup> O2, and Tween<sup>®</sup> 80 and Poloxamer 331 respectively. Shell thickness  $R_{\text{shell}} - R_{\text{core}}$  of loosely bound surfactant for our MEs were obtained 3.24 nm, 3.74 nm and 2.83 nm for O/W ME-series 4-1, series 4-2 and series 4-3. Observed shell thickness is in order of the hydrophilic chain length. Thus, it can be concluded that a monolayer of surfactant is surrounding the oil droplet. Difference between the values of monolayer thickness obtained for ME droplets in different oils can be explained as: one must consider the surfactant monolayer as being composed of a hydrophilic layer and a hydrophobic layer. It is reasonable to assume that oil with shorter alkane chain, will penetrate into the hydrophobic layer of the interfacial film to a greater extent. Oil penetration will be in hydrophobic layer only, causing oil core to increase, resulting smaller surfactant shell thickness in comparison to ME having same surfactant but different oil with larger alkane chain. The hydrophilic chain of non ionic surfactants (Tween<sup>®</sup> 80, Tagat<sup>®</sup> O2) is attached to hydrophobic part of molecule by a polymerization of ethylene oxide (EO), and the number of monomer units per molecule can not be controlled exactly. For Block copolymer (Poloxamer 331), there may be distribution in the hydrophobic domain also. This involves polymerization of propylene oxide (PO). The uncertainty in chain length of each surfactant molecule due to their polymerization may also cause different thickness of surfactant layer of ME having same surfactants.

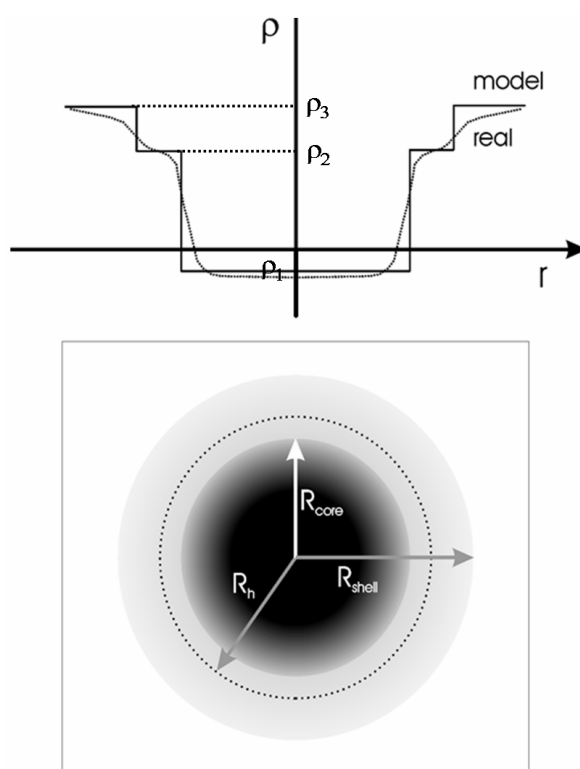


**Figure 5.22** Model of ME droplet defining size parameters for DLS ( $R_h$ ) and SANS ( $R_{\text{core}}$ ,  $R_{\text{shell}}$ ) calculations and profile of the scattering length density:  $r_1$ ,  $r_2$  and  $r_3$  represent SLD of oil, SLD of surfactant shell and SLD of continuous phase (water/PG) respectively.

Hydrophilic chain is shorter in Tween<sup>®</sup> 80 in comparison to Tagat<sup>®</sup> O2 may be reason that the shell thickness of ME droplets in oleic acid is smaller than ME droplets in IPP. IPP oil has larger alkane chain than the Eutanol and uncertainty in chain length of each surfactant molecule due to their synthesis may be reason that the shell thickness of ME droplets in Eutanol is smaller than ME droplets in IPP.

Noteworthy is the good agreement of the polydispersity indexes calculated from DLS and SANS, which are second order parameters. This is the hint that the chosen model for fitting is in the agreement. The SANS data are also fitted in Guinier approximation range (see Figure 5.23D) yielding the gyration radius  $R_g$ . This size parameter is connected with the moment of inertia of droplet. One can calculate the ratio between  $R_g$  and  $R_h$  and got the value 0.72 for ME 1, 0.70 for ME 2 and 0.74 for ME 3. These values are quite in agreement for the smallest possible value of 0.77 for hard spheres justifying our calculations, too, in which we used a solid sphere model for structure factor and hard-sphere including repulsive interaction potential (repulsive potential is perturbation on the hard sphere potential) correction for the diffusion coefficient.

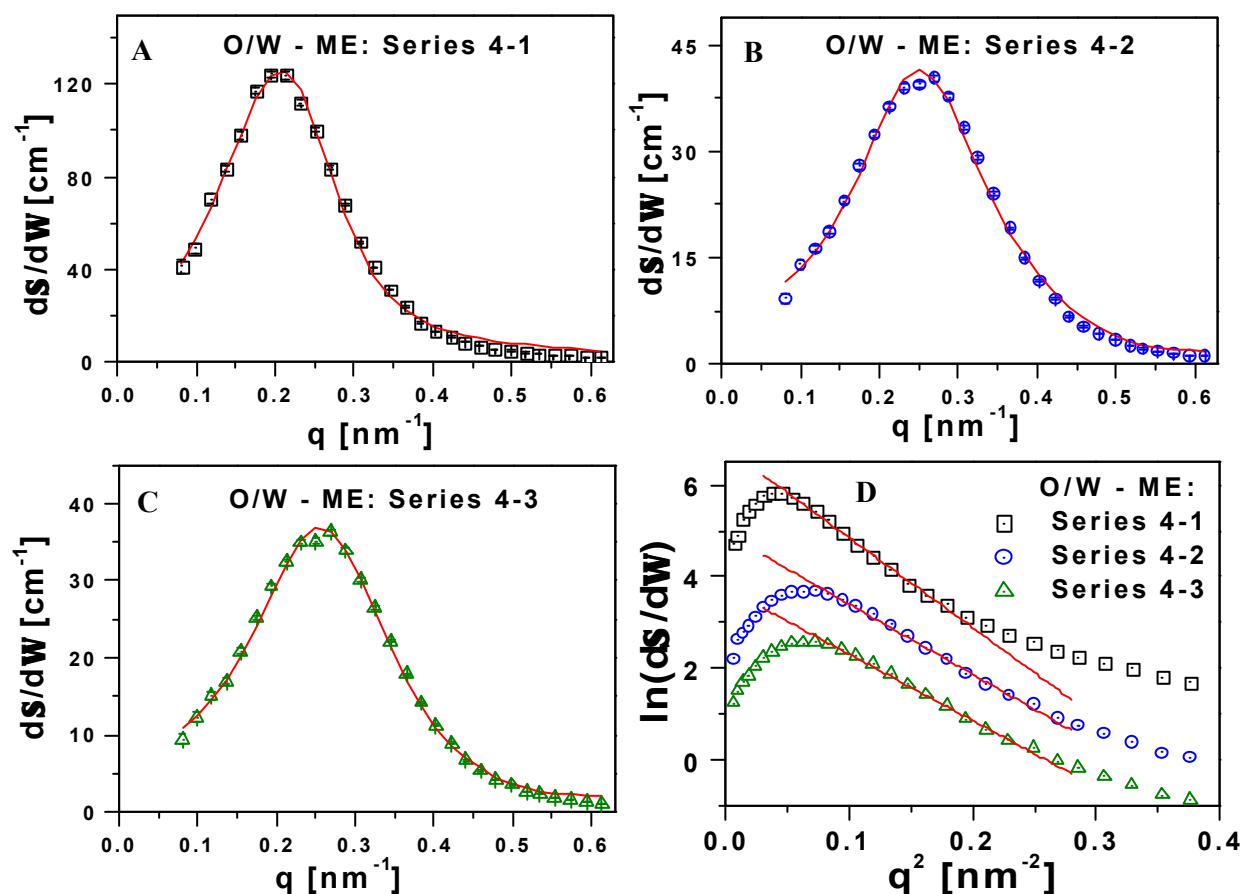


**Figure 5.23** SANS curves from different ME (points) and fitted curve (line) using core shell spherical model are shown in first three figures A, B and C. The logarithmic SANS curve from different ME and fitted curves using Guinier Approximation (line) are shown in figure D, upper curve is shifted by the value of +1 and lower curve by -1.

### 5.2.2.1.5 Effect of Temperature on Droplet Size of O/W - ME

In this section, effect of the temperature on the droplet size of ME having IPP as oil was investigated by means of DLS and SANS. The results from the fit of SANS curves and autocorrelation function obtained from DLS are summarized in Table 5.13.

Sample	DLS			SANS			
	T [°C]	R <sub>h</sub> [nm]	s <sub>s</sub>	T [°C]	R <sub>core</sub> [nm]	R <sub>shell</sub> [nm]	s <sub>s</sub>
Series 4-2	25	9.58	0.16	25	7.75	11.49	0.17
	32	9.258	0.17	35	7.61	11.29	0.20
	37.51	8.163	0.20	45	7.42	10.95	0.22

**Table 5.13** DLS and SANS results for O/W - MEs series 2. Errors are smaller than  $\pm 5\%$  for radii.

It can be easily seen from the Figure 5.24 that there is no significant change in system due to increase in temperature. So one can easily conclude from Figure 5.24 that our system is thermodynamically stable till temperature 45°C. Only slight decrease in droplet size is observed (see Table 5.13 and Figure 5.24 only slight difference in decay of correlation function with decay time) with increase in temperature. The possible explanation for the decrease in droplet size may be that when the temperature is raised, the directional hydrogen bonding between the surfactant and water molecules begin to break, which causes decrease in width of structured water around the droplet. As explained in the Section 5.2.1.2, with decrease in structured water, repulsive part of interaction between droplets decreases. This decrease in repulsive interaction will increase the diffusion of droplets. This increase in diffusion will cause decrease in hydrodynamic radius

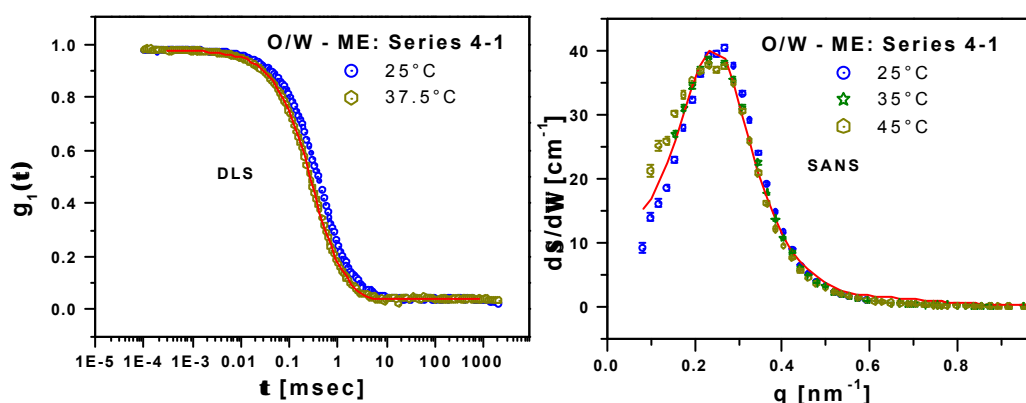


**Figure 5.24** DLS- Field autocorrelation function of ME at different temperature (points) fitted curve (line at temperature 25°C) versus  $t$ . SANS - spectrum from MEs (points) and fitted curve (line at temperature 25°C) versus  $q$ .

### 5.2.2.2 W/O - MEs of Pharmaceutical Interest

W/O - MEs, which are focused in this study, were developed in our research group. The existence of the ME field was monitored by the corresponding phase diagram. The ME phase was identified as area in the phase diagram where clear and transparent formulations are obtained based on visual inspection of many samples. Detailed description of phase diagram is presented elsewhere.<sup>136,153</sup> For the investigations of W/O - MEs, four series were prepared. The compositions of the MEs used are summarized in Table 5.14.

W/O - ME		Pharmaceutical Oil	Span <sup>®</sup> 20/ Tween <sup>®</sup> 80	Water/DMSO
<b>Series 1</b> (MEs with different ratios of surfactants)	1	8 (IPP)	2 (1:9)	0.22 (1:0)
	2	8 (IPP)	2 (3:7)	0.82 (1:0)
	3	8 (IPP)	2 (4:6)	1 (1:0)
	4	8 (IPP)	2 (5:5)	1.44 (1:0)
	5	8 (IPP)	2 (6:4)	1.3 (1:0)
	6	8 (IPP)	2 (7:3)	1 (1:0)
	7	8 (IPP)	2 (8:2)	0.4 (1:0)
	8	8 (IPP)	2 (9:1)	0.2 (1:0)
<b>Series 2</b> (MEs with different ratios of water/DMSO)	1	8 (IPP)	6.3 (0:1)	1 (0:6)
	2	8 (IPP)	4.5 (0:1)	1 (1:5)
	3	8 (IPP)	2.5 (0:1)	1 (2:4)
	4	8 (IPP)	3.6 (0:1)	1 (5:1)
<b>Series 3</b> (ME with different amounts of Surfactant)	1	8 (IPP)	2 (1:0)	2 (0:1)
	2	8 (IPP)	2.2 (1:0)	2 (0:1)
	3	8 (IPP)	2.4 (1:0)	2 (0:1)
	4	8 (IPP)	2.6 (1:0)	2 (0:1)
	5	8 (IPP)	2.8 (1:0)	2 (0:1)
<b>Series 4</b> (ME with different kinds of oil)	IPP	8 (IPP)	2 (3:2)	1 (1:0)
	MCT	8 (MCT)	2.5 (3:2)	1 (1:0)

**Table 5.14** The composition of the MEs studied (content in ml)

Two exponential correlation functions are not observed for these W/O - ME systems. While at equally high volume fraction, it was observed in O/W - ME (see Section 5.2.1). The possible explanations for absence of self diffusional mode are as follow: Firstly the observation of a

self-diffusion mode in the measured correlation function implies a significant degree of droplet interaction and polydispersity. It is possible that different systems show markedly different interaction and polydispersities. Secondly, in less viscous systems where  $D_s$  is expected to be larger, the self diffusional mode, even when present, will have a smaller effect on the form of the correlation function.<sup>49</sup> W/O - MEs listed in Table 5.14 (7.5 cP) are less viscous than O/W - ME systems (9.5 cP) for dermal use, my be that is the reason that two diffusion modes are not observed for these MEs. The apparent diffusion coefficient, hydrodynamic radius and polydispersity index have been then deduced using third order cumulant fitting procedure (see Section 4.3). From dilution procedure, it was observed that droplet interact via hard – sphere potential. This finding is not an unreasonable in the case of a W/O - ME made with non-ionic surfactants, there is only steric hindrance preventing coalescence of droplets. Hard sphere model is then used to correct the results for interdroplet interaction for MEs in further series.

### 5.2.2.2.1 Series 1: W/O - MEs with Different Ratios of Surfactants (Span<sup>®</sup> 20 and Tween<sup>®</sup> 80)

In the first series of W/O - MEs, effect on the solubilization of the inner phase and resulting droplet size was investigated using different ratio of the surfactants (Span<sup>®</sup> 20 and Tween<sup>®</sup> 80). First noticeable thing about the results obtained is that only either Tween<sup>®</sup> 80 or Span<sup>®</sup> 20 is not able to form the droplets having water as a colloidal phase (see Figure 5.25). It can be easily seen in the Figure 5.25 that big and unstable droplets were observed for systems having more than 70 % volume of either Tween<sup>®</sup> 80 or Span<sup>®</sup> 20 in mixture of Span<sup>®</sup> 20 and Tween<sup>®</sup> 80. There is definite decrease in aggregate size was observed after decreasing level of either Span<sup>®</sup> 20 or Tween<sup>®</sup> 80 from 70 % volume in the mixture of both (see Figure 5.25). These results suggest that it is not possible to achieve the required interfacial tension  $\gamma$  with the use of one single surfactant. Since an essential requirement for the formation and stability of ME is the attainment of very low interfacial tension.

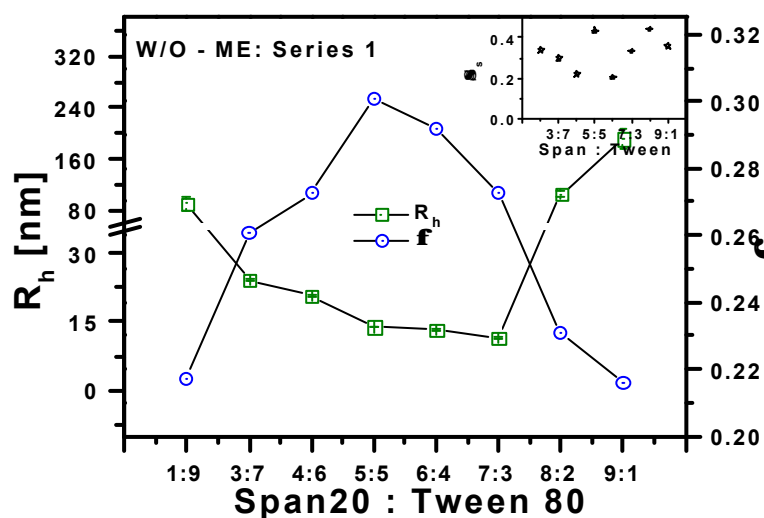


**Figure 5.25** DLS results (hydrodynamic radius  $R_h$  and polydispersity  $s_s$ , shown in the inset) and volume fraction for W/O - MEs series 1.

MEs have a very large interface between oil and water because of the small droplet size, they can only be thermodynamically stable if the interfacial tension is so low that the positive interfacial energy given by  $\gamma A$  (where  $A$  is interfacial area) can be compensated by the negative free energy of mixing  $\Delta G_m = -T\Delta S_m$ . The entropy of mixing is the order of the Boltzmann constant  $k_B$ ; hence the limiting value of  $\gamma$  required for stable ME droplet is

$$g = \frac{k_B T}{A}.$$

Thus for an equal composition (constant dispersed phase i.e., constant dispersed volume) interfacial area is larger for small droplets and small for large droplets. For droplet radius of about 10 nm, an interfacial tension of  $0.03 \text{ m N m}^{-1}$  would be required. The addition of the another surfactant (either Tween<sup>®</sup> 80 or Span<sup>®</sup> 20) in increasing amounts causes a gradual reduction of  $\gamma$  to a certain value. But further reduction from this certain value of interfacial tension does not occur, since oil/water interface is now saturated with surfactant (either Tween<sup>®</sup> 80 or Span<sup>®</sup> 20). Addition of  $> 30\%$  either Tween<sup>®</sup> 80 (in Span<sup>®</sup> 20-water-oil system) or Span<sup>®</sup> 20 (in Tween<sup>®</sup> 80-water-oil system), stable ME droplets were observed (see Figure 5.25). Reduction in size suggests that Span<sup>®</sup> 20 (in Tween<sup>®</sup> 80-water-oil system) or Tween<sup>®</sup> 80 (in Span<sup>®</sup> 20-water-oil system), penetrate into the interfacial film of the dispersed colloidal droplet, lowering the interfacial tension to achieve the required interfacial area for stable ME droplets. Droplet size was shown to increase as Tween<sup>®</sup> 80/Span<sup>®</sup> 20 increases (see Figure 5.25). It seems reasonable because, comparing a Span<sup>®</sup> 20 molecule with Tween<sup>®</sup> 80, one can see that the Span<sup>®</sup> 20 has much smaller head group relative to the size of the tail (Figure D.11). If a monolayer was to be made entirely of Span<sup>®</sup> 20, it would tend to curve towards the head group side (head group inside the droplet) while Tween<sup>®</sup> 80 would tend to curve towards the other way. At an oil/water interface, an excess of Span<sup>®</sup> 20 would cause a high interfacial curvature and thus small water-in-oil droplet. Adding Tween<sup>®</sup> 80 would tend to lower the curvature of the interface, resulting in larger droplet. The maximum solubilisation parameter  $\phi$  was found 0.30. This observed solubilisation parameter is consistent with the theoretical prediction for the small radius with large interface. The theoretical maximum ratio of dispersed phase to total volume  $\phi$  is 0.74. This is volume fraction assuming equal sized sphere packed in the face centered cubic or hexagonal close packing configurations. Several factors work to reduce this value. First, the thickness of the interface is not zero, but rather finite, and gains more relative importance as the radius of the droplets diminishes. For an interface 1% of the radius, the theoretical maximum parameter fall to 0.72 and for an interface 35% of the radius these parameter fall to 0.30.<sup>154</sup> Second, a distribution in the droplet size will also result in lower maximum parameters, as the ideal packing structure will be disrupted.

### 5.2.2.2.2 Series 2: W/O - MEs with Different Ratios of Water/DMSO

As concluded from the earlier section that either only Span<sup>®</sup> 20 or Tween<sup>®</sup> 80 can not achieve the required interfacial tension to form stable ME droplets having water as a dispersed phase (see Figure 5.25). But it was found that stable ME can be obtained by the blend of the both surfactants. In this section, formation and stability of ME having only single surfactant Tween<sup>®</sup> 80 was investigated by changing the hydrophilicity of the inner phase. Effect of the different volume ratio of water / DMSO (i. e., different hydrophilicity of the inner phase) on the droplet size having Tween<sup>®</sup> 80 as surfactant is shown in Figure 5.26. These results suggest that it is possible to achieve the required interfacial tension  $\gamma$  with the use of DMSO instead of using another surfactant. Stable MEs were observed at  $> 17\%$  of DMSO in the water and DMSO mixture. It indicates that incorporation of DMSO in increasing amounts causes a gradual reduction of  $\gamma$  (hence droplet size) to a required value for stable droplet formation (see Figure 5.26). Addition of DMSO  $> 66\%$  in the water and DMSO mixture caused increase in the hydrodynamic radius. This result suggested that *DMSO*, at least partially, locate in the interfacial surfactant region, behaving in much the same way as a *cosurfactant*.

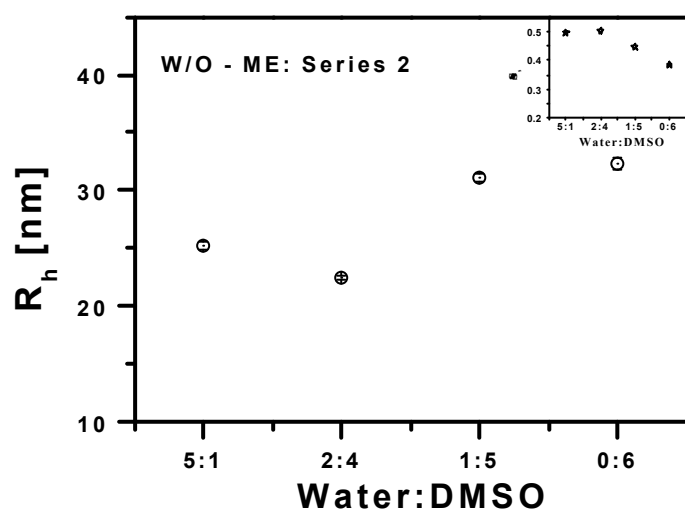


**Figure 5.26** DLS results (hydrodynamic radius  $R_h$  and polydispersity  $s_s$ , shown in in-set) for W/O - MEs series 2.

### 5.2.2.2.3 Series 3: W/O - MEs with Different Amounts of Surfactant

Effect of the increasing amount of surfactant on droplet size was shown in Figure 5.27. From earlier section, it was concluded that DMSO, at least partially, locate in the interfacial surfactant region. In this section, DMSO is used as cosurfactant as well as inner phase instead of water and effect of increasing amount of surfactant on formation and stability was investigated. Stable MEs were observed at the range of  $20.5 \text{ wt}\% < \text{Span}^{\text{®}} 20 \text{ amount} < 28 \text{ wt}\%$ . It also indicates that that incorporation of Span<sup>®</sup> 20 in increasing amounts causes a gradual reduction of  $\gamma$  to a required value for droplet formation. Addition of Span<sup>®</sup> 20 amount

in the range 20.5 wt% < Span<sup>®</sup> 20 amount < 24 wt% causes increase in the hydrodynamic radius.

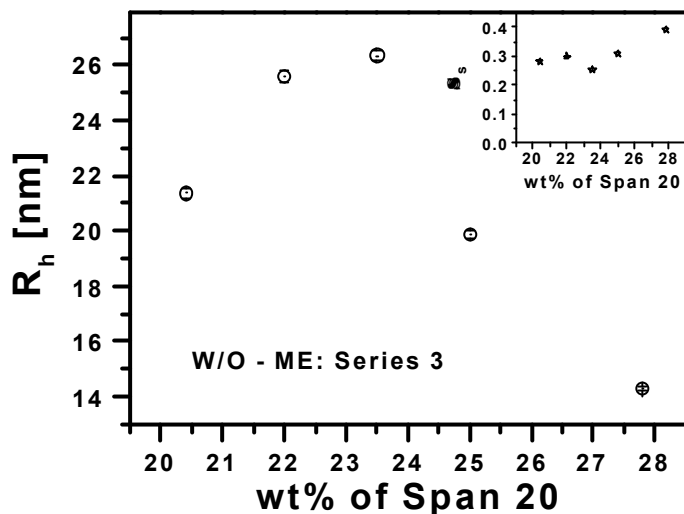


**Figure 5.27** DLS results (hydrodynamic radius  $R_h$  and polydispersity  $s_s$ , shown in in-set) for W/O - MEs series 2.

This result suggests that, incorporation of Span<sup>®</sup> 20 in this range does not cause further reduction of interfacial tension, since the oil/DMSO interface may be saturated with Span<sup>®</sup> 20 and DMSO and any Span<sup>®</sup> 20 added in excess of this limiting concentration accumulate at the droplet surface causing increase in droplet size. And further increase of Span<sup>®</sup> 20 amounts (> 24 wt%) provide sufficient interfacial surface to break the bigger droplets into smaller droplets in order to increase total surface area. And again addition of Span<sup>®</sup> 20 in increasing amounts till 28 wt% causes a gradual reduction of  $\gamma$  and so droplet size. Finally, system having more than 28 wt% of Span<sup>®</sup> 20 showed no tendency to accumulate either on interface or droplet surface, which leads to destroy the ME.

#### 5.2.2.2.4 Series 4: W/O - MEs with Different Kinds of Oils

It can be easily seen from Table 5.15 that there is definite increase in droplet size for MEs with larger molecular volume oil (MCT) when compared to the smaller molecular volume oil (IPP). Reduction in size observed in the presence of the oil small in molecular volume suggests that the smaller volume oil penetrates easily into the surfactant layers. Therefore, the spontaneous curvature of the layer will then be larger for MEs in smaller molecular volume oil than in longer molecular volume.

W/O - ME	Kind of oils	$D_{app} \cdot 10^8$ [cm <sup>2</sup> /sec]	$R_h$ [nm]	$s_s$
Series 4-1	IPP	3.187	13.31	0.21
Series 4-2	MCT	0.483	31.89	0.31

**Table 5.15** DLS results for W/O - MEs series 4. Errors are smaller than  $\pm 5$  % for radii.

### 5.2.2.2.5 Effect of Temperature on Droplet Size of W/O - ME

In this section, effect of the temperature on the droplet size of W/O - MEs having IPP as oil was investigated by means of DLS. The results from the fit of autocorrelation function obtained from DLS are summarized in Table 5.16. It can be easily seen from the Figure 5.28 that there is no significant change in system due to increase of temperature. So one can easily conclude from Figure 5.28 that our system is thermodynamically stable till 40°C. Only slight decrease in droplet size is observed (One can see in Figure 5.28 that only slight difference in decay of correlation functions at different temperature) with increase of temperature. The possible explanation for the decrease in droplet size may be that when the temperature is raised, it is hard for oil to pack in a favorable orientation to interact with the surfactant tails and so surfactant – surfactant interaction will increase. This attractive surfactant – surfactant interaction will increase the diffusion of droplets. This increase in diffusion will cause decrease in hydrodynamic radius. This mechanism could also explain the phase separation at very high temp. When temperature is high enough, phase separation will occur due to strong surfactant – surfactant interactions. It should be noted that polydispersities of our W/O - MEs lie in the range 25 - 50%, which are the upper end of what is expected, both theoretically and experimentally, for the polydispersity of stable ME droplets. The possible explanation for large polydispersity is due to the fact that the cumulant analysis (represents only small correction to the shape of the correlation function) overestimate the polydispersity of ME droplets which is consistent with our earlier finding for model ternary AOT-MEs.

Sample	DLS		
	T [°C]	$R_h$ [nm]	$s_s$
Series 4-1	25	13.31	0.21
	30	8.28	0.27
	35	7.37	0.26
	40	6.54	0.34

**Table 5.16** Hydrodynamic radius  $R_h$  and polydispersity  $s_s$  of W/O - MEs series 4 at different temperature. Errors are smaller than  $\pm 5\%$  and  $\pm 10\%$  for radii and polydispersity index, respectively.

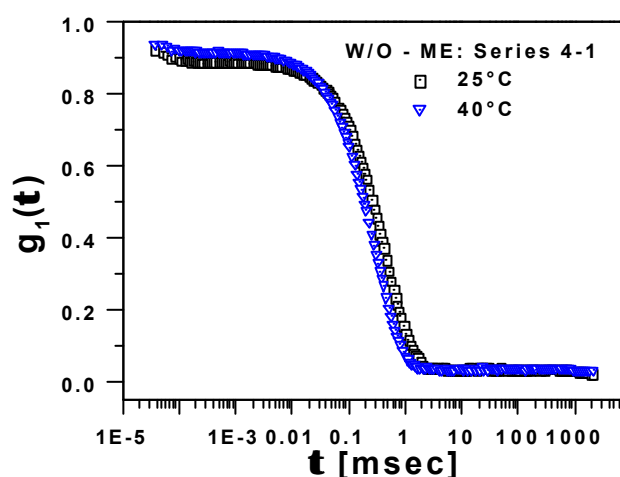


**Figure 5.28** DLS- Field autocorrelation function of MEs series 4 at different temperature (points).

### 5.3 Characterization of MEs based on an Eutectic Mixture of Lidocaine and Prilocaine as the Dispersed Phase

O/W - MEs were formulated using an eutectic mixture of lidocaine and prilocaine as lipophilic colloidal phase, a blend of a high (Tween<sup>®</sup> 80) and a low (Poloxamer 331) HLB non-ionic surfactant, and a hydrophilic phase (PG/water) which are of pharmaceutical interest. Lidocaine and prilocaine have been shown to form an eutectic mixture at room temperature,<sup>155</sup> the composition of which is approximately 1:1 by weight.<sup>156</sup> Hence is derived the name “eutectic mixture of local anaesthetics or EMLA. Although eutexia of lidocaine and prilocaine tends to reduce the aqueous solubility of each component, the effect on their combined solubility is small.<sup>17</sup> Furthermore, this solid-solid interaction yields a liquid which can be emulsified in water rather than suspended. These colloidal vehicle systems (MEs) offer very good conditions for the fast and deep penetration of biologically active substances such as local anaesthetics into skin layer.<sup>136</sup> Despite of plenty of publications regarding dermal local anesthetics, there are only very few investigations regarding pharmaceutical compositions comprising local anaesthetics as dispersed, colloidal phase.<sup>157,158,159</sup> Particular interest of the present study is the characterization of MEs consisting of drug (lidocaine and prilocaine) as a dispersed, oily colloidal phase. For preparing suitable MEs for dermal application, it is important to know the effectiveness of the different concentration of components used in the formulation of MEs. It is observed that without any oil, lidocaine/prilocaine mixture as lipophilic colloidal and water or buffer/PG as a hydrophilic phase formed thermodynamic stable MEs. These stable MEs can solubilize up to 20% eutectic mixture of local anaesthetics (lidocaine and prilocaine). For practical applications, effect of pH on MEs is also examined. Water is replaced by Sorensen Clark buffer and different concentrations of NaOH, in order to increase the pH of the ME.

ME	Series 1 (Constant $\mu$ )				Series 2 (Different $\mu$ )					Series 3 (Different pH)				
Lidocaine / Prilocaine (1:1)	5	10	15	20	2	5	10	15	20	5	5	5	5	5
Synperonic <sup>®</sup> PE L101 / Tween <sup>®</sup> 80 (3:2)	5	10	15	20	20	20	20	20	20	20	20	20	20	20
Water / PG (1:2)	90	80	70	60	78	75	70	65	60	75	75	75	75	75
NaOH	-				-					0N	Buff	0.01 N	0.1 N	1N

**Table 5.17** The composition of the MEs studied (content in wt %; except NaOH).

The composition of the MEs used for study is summarized in Table 5.17. The apparent diffusion coefficient and polydispersity index have been deduced using cumulant fitting procedure (see Chapter 4 for detail) from the normalized field auto correlation function  $g^1(\tau)$  averaged over the angles.

### 5.3.1 Series 1 – Interdroplet Interaction

It has been shown earlier that to get meaningful calculation of droplet size, it is necessary to correct scattering measurements for interdroplet interaction in high concentration regions. In first series of MEs, systems were diluted with continuous phase keeping constant molar ratio  $\mu = 9.5$  to get the information about the interdroplet interaction. The measured diffusion coefficient and hydrodynamic radius for this series are listed in Table 5.18. As shown in Table 5.18, apparent diffusion coefficient decreases with increase of concentration. This suggests that ME droplets interact via hard sphere interaction with supplementary attractive interaction. This result shows that attractive dispersion forces are dominant in comparison to the indirect repulsive interactions associated with a given configuration of the MEs. While system having pharmaceutical oil as colloidal phase, main contribution in the effective potential is observed due to indirect repulsive interactions, which arise due to increased structuring of water around each ME droplet. The possible explanation for this difference is that head group of lidocaine and prilocaine have large tendency to produce local partial charge fluctuations in comparison to pharmaceutical oil like IPP. Dispersion attractive forces arise from the fact that in any material thermal motion and quantum effects produce local charge fluctuations. The resulting transient electric field exerts an attractive force on surrounding material. Fluctuations in the flexible surface of surfactant film can produce steric (hard sphere) interaction that accomplishes the stability of MEs (Helfrich force). MEs with  $\phi > 0.4$  are not stable, which indicate that sticky attractive potential is high enough to start coagulation process for MEs of higher volume fraction  $\phi > 0.4$ .

	Series 1 (Constant $\mu$ )				Series 2 (Different $\mu$ )					Series 3 (Different pH)				
<b>f</b>	0.10	0.20	0.30	0.40	0.22	0.25	0.30	0.35	0.40	0.25	0.25	0.25	0.25	0.25
<b><math>\mu</math></b>	9.50	9.50	9.50	9.50	0.95	2.37	4.75	7.12	9.50	2.37	2.37	2.37	2.37	2.37
<b>pH</b>	9.50	9.50	9.50	9.50	9.50	9.50	9.50	9.50	9.50	9.50	9.80	9.90	10.4	12
<b><math>D_{app} \cdot 10^8</math> [cm<sup>2</sup>/sec]</b>	2.80	2.04	1.85	1.76	4.57	4.03	3.06	2.34	1.76	3.76	3.63	3.89	1.03	1.54
<b><math>(R_h)_{app}</math> [nm]</b>	8.20	11.3	12.4	13.1	5.03	5.72	7.51	9.81	13.1	6.11	6.32	5.91	22.2	14.9
<b><math>s_s</math></b>	0.25	0.25	0.33	0.42	0.46	0.49	0.49	0.47	0.42	0.47	0.43	0.45	0.41	0.43

**Table 5.18** DLS results of ME having local anaesthetics as dispersed phase. Errors are smaller than  $\pm 5\%$  and  $\pm 10\%$  for radii and polydispersity index respectively.

### 5.3.2 Series 2 - MEs with Constant Amount of Surfactant and Continuous phase and Different Amount of dispersed Phase

Hydrodynamic radius  $R_h$  of MEs having different amount of dispersed phase is listed in Table 5.18. As shown in Table 5.18 incorporation of lidocaine and prilocaine causes an increase in droplet radius. For a blend of high and low HLB surfactant stabilized colloidal oil droplets, it has been found, that there is a linear relationship between  $R_h$  and  $\mu$  [ $R_h(\text{nm}) = 3.6 + 0.64 \mu$ ], which is consistent with results obtained earlier for MEs.

### 5.3.3 Series 3 – Effect of pH

In third series of ME, effect of pH on droplet size was investigated. The pH value of the systems rises with increasing basicity of the hydrophilic phase. Diffusion coefficient and droplet size obtained from these systems were listed in Table 5.18. Droplet size of local anaesthetics in oil form depends on the pH of the composition is observed, which is consistent with the results obtained from MEs having local anaesthetics as dispersed phase<sup>157</sup>. It is observed that droplet size is almost the same for MEs with water, buffer and 0.01 N NaOH as hydrophilic phase but by ten fold increase of NaOH concentration (0.1 N NaOH), more than three times bigger droplets were formed. And further ten fold increase of NaOH concentration (1 N); unstable ME droplets were observed. This behavior can be explained with the help of interactions between the ME droplets. At the high concentration of surfactant (~ 20% surfactant) this occurs in our systems, at the water side the hydrated chain of adsorbed non ionic surfactant molecules repel one another and try to curve the surface around the oil side. This mutual repulsion of hydrated chain can be weakened by adding electrolyte (NaOH) to the aqueous phase and thus increase in NaOH concentration promotes the attractive part of interaction.<sup>122</sup> Probably for MEs of higher NaOH concentration (> 0.01 N NaOH), attractive potential is strong enough to start droplet coagulation process. Further increase of electrolyte (NaOH) or change in pH, have a devastating effect on ME stability by further lowering the repulsive energy barrier and allowing droplets to expel the colloidal phase. So that smaller droplets would be formed at the cost of low stability. For that reason our described interaction potential supports observed stability for low NaOH concentration region as well as droplet growth and stability losses for the high NaOH concentration region. Thus one can produce these MEs in pH range 9.5 - 10.4.

It should be noted that polydispersity of our system lies in the range 25-50%, which are the upper end of what is expected, both theoretically and experimentally, for the polydispersity of stable ME droplets. The possible explanation for large polydispersity is due to the fact that the cumulant analysis (represents only small correction to the shape of the correlation function) overestimate the polydispersity of ME droplets.

## 6 Summary and Conclusions

The following section summarizes the key contributions of the research presented in this thesis, in the areas of ME characterization, ME formulation and ME stability. This thesis extends the knowledge of the microstructure and interdroplet interaction of model ternary water/AOT/*n*-alkane systems and the results obtained from this system are directly applied to examine the physical basis of the interdroplet interaction and behavior of each constituent solubilize in MEs of pharmaceutical interest. The experimental approach has been based upon the use of three different scattering techniques, SLS, DLS and SANS. The combination of these scattering techniques is found an excellent one for the characterization of MEs.

### 6.1 Model Ternary Water/AOT/*n*-alkanes MEs

- The ability to predict structural properties of ME from packing consideration and the optical properties of each constituent of ME alone can be a powerful tool, both for prediction of stability of MEs not yet formulated, and for tailoring molecules to achieve MEs with certain properties. Excellent results were achieved for the prediction of size, size polydispersity and interdroplet interaction for three different *n*-alkane ( $n = 7, 8$  and  $9$ ) types using packing and optical consideration of each constituent of ME.
- For interpretation of scattering results, the ME droplet is considered as a dynamic entity, a tiny spherical droplet surrounded by a monolayer of surfactant, which undergo Brownian motion in the usual fashion and sometimes combining with its neighbors during collision, and subsequently breaking apart (penetrable layered sphere model).
- ME droplets in a short chain alkane oil have slightly smaller droplets in comparison to droplets in larger chain alkane oil. The possible explanation for this result is due to the fact that oil penetration into the surfactant tail region is larger for shorter chain, which causes increase in spontaneous curvature of the surfactant layer in comparison to larger chain, which is consistent with the penetrable layered sphere model.
- The size polydispersity  $\sigma_s$  of the ME droplets was determined by contrast variation experiments with very high precision because polydispersity influences the characteristic features of scattering data as well as the hydrodynamic radius with the  $[\text{H}_2\text{O}]/[\text{AOT}]$  molar ratio  $\mu$ . For MEs droplets in *n*-heptane, *n*-octane and *n*-nonane, we found  $\sigma_s \sim 0.17$  and independent of alkane type, which is expected theoretically for the stable ME droplets.

- Shape changes of ME droplets with increase of temperature were determined and compared in three different *n*-alkane types. The ME diffusion data were analyzed at different temperature following Leaver et al.<sup>132</sup> The parameter (Axial ratio  $\rho$ ) describing structural change was evaluated. It was observed that at temperatures up to 10°C above the lower solubilization temperatures  $T_1$  of AOT W/O - MEs in *n*-alkanes oil nearly no change in the shape of the radius occur. The parameters describing the polydispersity and shape change are in agreement with parameters determined earlier for MEs stabilized by AOT using SAXS,<sup>133</sup> NMR,<sup>131</sup> combination of SANS and NSE<sup>160</sup>.
- In order to extract information about the concentration dependence of diffusion coefficient, dilution procedure was used to vary the droplet concentration over wide range ( $\phi \sim 0.02-0.50$ ) with reasonable expectation that its radius will be roughly constant. At higher droplet concentrations ( $0.20 < \phi < 0.5$ ), splitting in diffusion coefficient was observed. This shows that at higher concentration, diffusion dynamics involve two processes- one is due to collective diffusion of the droplets (total droplet number density fluctuation), where as the other is due to the self diffusion of the droplets (concentration fluctuations of species in the droplet).
- ME droplets do not behave like hard sphere and that supplementary attractive interactions must be taken into account. This finding is consistent with dynamic model for ME droplets, which undergo Brownian motion in the usual fashion and the attractive energy give rise to “sticky” interactions due to surface adhesion upon collision. Such sticky encounters result in short living clusters that may exchange solubilized material before dissociating into separate droplet causing collective and self diffusion of droplets. Assuming a microscopic model for the interaction of interpenetrating surfactant tails, interaction energy density per droplet was estimated.
- It was found that attractive interaction energy slightly increases with increase of the length of alkane chain. This is consistent with the penetrable layered sphere model that attractive surfactant to surfactant interaction becomes stronger as the ME droplet sizes (hence the penetrable volumes) are increased and at constant temperature, it would be harder for the longer *n*-alkane oil molecule to interact with the surfactant than for shorter oil molecule to interact, due to packing considerations. This mechanism could also explain the shift of the region of ME stability to lower temperatures for higher chain length alkanes.
- The polydispersity in ME systems is dynamic in origin, characterized by a local fluctuation time  $\tau_p > 10^{-4}$  sec. Results indicate that the time scale for local polydispersity fluctuations is at least three orders of magnitude longer than the estimated time between droplet collisions.
- In the concentrated systems, where polydispersity fluctuations become distinguishable, a value for size ( $\sigma_s$ ) and optical ( $\sigma_o$ ) polydispersities were obtained from relative amplitude of the slow decay mode using coupled combination of optical and size polydispersities.

These values for the optical polydispersity are consistent with the values estimated from the residual scattering of samples at matching point. It was observed that optical polydispersity decreases with increasing oil chain length as it is expected from difference between refractive index of  $n_s$  and  $n_o$ , which decreases with increasing chain length.

## 6.2 MEs of Pharmaceutical Interest

- Scattering techniques are used to characterize the physico-chemical properties of MEs consisting of pharmaceuticals oils, surfactant or a blend of a high and a low HLB surfactant, and a hydrophilic phase either (propylene glycol/water) or water or DMSO.
- Using the results obtained from model ternary systems, information about droplet size, interdroplet interaction and polydispersity from experimental data for these systems were extracted using dilution procedure.
- An effective repulsive force between the O/W - ME droplets were observed. The origin of this net repulsive interaction is thought to be the breaking of hydrogen bonds due to removal of water molecules from the hydrated chain of nonionic polyether surfactant on close approach of two similar droplets. Change in energy  $U_b$  due to removal of water molecules and the width of the layer of structured water  $\Lambda$  are estimated for our systems, which is consistent with the value necessary for stable ME. As expected this repulsive part of interaction increases with  $\Lambda$ .
- The observed droplet- droplet interactions for MEs increase the coagulation time by the factor  $W \sim 10^{65}$  in comparison to rapid coagulation, when there is no interaction between the droplets, except a very steep attraction when droplets touch each other. This is consistent with observed stability of our systems.
- Hydrodynamic radius used for the characterization of these systems has been corrected for interdroplet interaction using suitable interaction model proposed for our systems. In the absence of such a correction, the value of droplet size obtained is taken as indicative only for the presence of ME droplets.
- Cumulant analysis may considerably overestimate the polydispersity at higher concentration where high correlation between the second cumulant and base line is expected.
- W/O - ME droplets interact via hard – sphere potential. This finding is not an unreasonable in the case of a W/O - ME system made with non-ionic surfactants, there is only steric hindrance preventing coalescence of droplets. Hard sphere model is then used to correct the results for interdroplet interaction for O/W - MEs.

- 
- A small amount of PG or DMSO penetrates into the interfacial film of the dispersed droplet, behaving in much the same way as a cosurfactant.
  - It was shown that the mixtures of high HLB surfactant Tween<sup>®</sup> 80 or Tagat<sup>®</sup> O2 and low HLB Span<sup>®</sup> 20 or Poloxamers increase the stability and solubility of the dispersed phase.
  - Droplet size was shown to increase when the Tween<sup>®</sup> 80/Span<sup>®</sup> 20 ratio increases.
  - Different kind of oils have been used in this study, which show that the size of ME droplets is independent of kind of oils comparable in molecular volume.
  - With the incorporation of drug and more oil in O/W - ME causes increase in the droplet size. Our MEs for dermal use were thermodynamically stable till 40°C.
  - MEs having local anesthetics drug (lidocaine and prilocaine) as a dispersed, oily colloidal phase were characterized.

## 6 Zusammenfassung und Schlussfolgerungen

Der folgende Abschnitt fasst die wesentlichen Forschungsbeiträge dieser Arbeit auf den Gebieten der ME-Charakterisierung und –formulierung sowie der mizellaren Stabilität zusammen. Diese Arbeit erweitert das Wissen über die Mikrostruktur und die Wechselwirkung inverser Mizellen in ternären Wasser/AOT/*n*-Alkan-Systemen. Die erzielten Ergebnissen werden direkt genutzt für eine Betrachtung der physikalischen Grundlagen der mizellaren Wechselwirkung und des Verhaltens jeder einzelnen Komponente in pharmazeutisch relevanten ME. Auf experimenteller Seite werden drei verschiedene Streutechniken verwendet, SLS, DLS und SANS. Die Kombination dieser drei Techniken hat sich als hervorragendes Werkzeug für die Beantwortung der gestellten Fragen ergeben.

### 6.1 Modell: Ternäre Wasser/AOT/*n*-Alkan ME

- Die Möglichkeit, strukturelle Eigenschaften von ME-Tropfen allein aus Packungsüberlegungen und den optischen Eigenschaften der einzelnen Komponenten abzuleiten, ist ein mächtiges Werkzeug, sowohl für die Betrachtung der Stabilität von ME als auch zur Ermittlung von Substanzen, deren Mischung ME mit bestimmten Eigenschaften ergeben. In dieser Arbeit wurde damit hervorragende Ergebnisse hinsichtlich der Betrachtung der Größe, der Polydispersität und der Wechselwirkung von inversen Mizellen in drei verschiedenen *n*-Alkan-ME ( $n = 7, 8$  and  $9$ ) erzielt.
- Für die Interpretation der Streudaten wurden die ME-Tropfen als dynamische Entität angenommen, als kleine sphärische Tropfen, jeweils umgeben von einer Monolage Tensidmoleküle. Sie unterliegen der Brownschen Bewegung und Kollisionen untereinander können zu einer Verschmelzung der Tropfen führen mit anschließendem Wiederauseinanderbrechen („penetrable layered sphere model“).
- ME-Tropfen in kürzerkettigen Alkanölen sind etwas kleiner als die in längerkettigen. Eine mögliche Erklärung für dieses Verhalten liefert die Tatsache, dass kürzerkettige Alkane leichter in die Tensidschwänze penetrieren können, was zu einer Zunahme der spontanen Krümmung der Tensidhülle im Vergleich zu langkettigen Ölen führt (konsistent mit dem „penetrable layered sphere model“).
- Die Größenpolydispersität  $\sigma_s$  der ME-Tropfen wurde durch Kontrast-Variations-Experimente mit sehr hoher Genauigkeit bestimmt. Die Polydispersität bestimmt nicht nur die charakteristischen Merkmale der Streudaten, sie hat auch Einfluss auf den Verlauf der Abhängigkeit der hydrodynamischen Radien vom Wasser-zu-AOT-Teilchenzahlverhältnis  $\mu=[\text{H}_2\text{O}]/[\text{AOT}]$ . Für inverse Mizellen in Heptan, Octan und

Nonan ergab sich  $\sigma_s \sim 0,17$ , unabhängig vom Alkantyp. Dies wurde für stabile inverse Mizellen auch theoretisch erwartet.

- Formveränderungen der ME-Tropfen mit steigender Temperatur wurden bestimmt und für die drei verschiedenen Alkane verglichen. Dabei wurden die Daten gemäß Leaver et al.<sup>136</sup> analysiert. Der die strukturelle Veränderung beschreibende Parameter  $\rho$  (Achsenverhältnis) wurde ermittelt. Bis zu Temperaturerhöhungen von 10°C oberhalb der unteren Löslichkeitsgrenze  $T_1$  wurde nahezu keine Veränderung der Form der Tropfen beobachtet. Die ermittelten Parameter, welche die Polydispersität und die Formveränderungen beschreiben, sind in Übereinstimmung mit Literaturdaten aus SAXS-Fehler! Textmarke nicht definiert., NMR-Fehler! Textmarke nicht definiert. und kombinierten SANS- und NSE-Fehler! Textmarke nicht definiert.Messungen.
- Um Informationen über den Einfluss der Konzentration auf die Diffusionskoeffizienten zu erhalten, wurden die ME über einen weiten Konzentrationsbereich verdünnt ( $\phi \sim 0,02 - 0,50$ ), unter der begründeten Annahme, dass die Tropfenradien nahezu konstant bleiben. Bei hohen Tropfenkonzentrationen ( $0,20 < \phi < 0,50$ ) wurde ein Aufspalten der Diffusionskoeffizienten beobachtet. Dies zeigt, dass, bei hohen Konzentrationen zwei Prozesse zur Diffusionsdynamik beitragen, einer ist die kollektive Diffusion der Tropfen (Schwankung der gesamten Tropfenzahldichte), der andere die Selbstdiffusion (Konzentrationschwankungen).
- ME-Tropfen verhalten sich nicht wie harte Kugeln, attraktive Wechselwirkungen müssen berücksichtigt werden. Dieses Ergebnis ist konsistent mit einem dynamischen Modell für die ME-Tropfen; die Brownsche Bewegung der Tropfen ermöglicht Zusammenstöße, die Oberflächenadhäsion entspricht einer attraktiven Wechselwirkung („sticky interactions“). Diese Wechselwirkung führt zur Ausbildung kurzlebiger Cluster, was zum Austausch gelöster Stoffe zwischen den Tropfen führen kann bevor diese wieder separieren. Unter der Zuhilfenahme eines mikroskopischen Modells für die Wechselwirkung von sich gegenseitig penetrierenden Tensidschwanzgruppen wurde die Wechselwirkungsenergiedichte pro Tropfen abgeschätzt.
- Es ergab sich, dass die Wechselwirkungsenergie leicht zunimmt mit zunehmender Alkankettenlänge. Das ist konsistent mit dem „penetrable layered sphere model“, in welchem Tensid-Tensid-Wechselwirkungen stärker werden mit zunehmender Tropfengröße (mit zunehmendem penetrierbarem Volumen). Bei konstanter Temperatur ist es für länger-kettige Alkane schwerer, mit den Tensidmolekülen wechselzuwirken als für kürzer-kettige aufgrund von Packungsüberlegungen. Dieser Mechanismus könnte ebenfalls die Verschiebung des Stabilitätsbereichs von ME hin zu niedrigeren Temperaturen bei Verwendung von länger-kettigen Alkanölen erklären.
- Die Polydispersität von ME-Systemen ist in ihrem Ursprung dynamisch, charakterisiert durch eine lokale Fluktuationszeit von  $\tau_p > 10^{-4}$  s. Die Ergebnisse weisen darauf hin, dass

die Zeitskala lokaler Polydispersitätsfluktuationen mindestens drei Größenordnungen über der der Tropfenkollisionen liegt.

- In höherkonzentrierten Systemen, in welchen Schwankungen der Polydispersität messbar waren, wurden Werte sowohl für die Größenpolydispersität  $\sigma_s$  als auch die optische Polydispersität  $\sigma_o$  ermittelt (Auswertung der relativen Amplituden des langsamen Abfalls). Die Werte für die optischen Polydispersitäten sind in Übereinstimmung mit den Werten, welche aus der Reststreuung der untersuchten Systeme am „matching point“ ermittelt wurden. Es wurde beobachtet, dass die optischen Polydispersitäten zunehmen mit zunehmender Kettenlänge der Alkane. Dies wurde auch anhand einer Betrachtung der Differenz der Brechungsindizes  $n_s$  und  $n_o$  so erwartet; die Differenz nimmt mit zunehmender Kettenlänge ab.

## 6.2 Mikroemulsionen mit pharmazeutischer Relevanz

- Die Streutechniken wurden benutzt, um die physiko-chemischen Eigenschaften von ME von pharmazeutischem Interesse aufzuklären. Die untersuchten Systeme bestanden aus pharmazeutischen Ölen und Tensiden bzw. einer Mischung aus Tensiden mit hoher und niedriger HLB sowie einer hydrophilen Phase (Propylenglykol/Wasser, Wasser, DMSO).
- Unter Zuhilfenahme der an den untersuchten modellhaften ternären Systemen gewonnenen Erkenntnissen wurden auch hier Informationen über die Tropfengröße, die Polydispersität sowie die Tropfen-Wechselwirkung gewonnen.
- Zwischen den Tropfen wurde effektiv eine abstoßende Wechselwirkung beobachtet. Ursächlich dafür sollte ein Brechen von Wasserstoffbrückenbindungen der Wassermoleküle sein, wenn diese sich bei Annäherung zweier gleicher Tropfen aus den hydratisierten Ketten nichtionischer Polyäther-Tenside herauslösen. Die damit verbundene Energieänderung  $U_0$  und die Dicke der Schicht strukturierten Wassers  $\Lambda$  wurden abgeschätzt. Diese entsprachen den erwarteten Werten für die Bildung stabiler ME. Die abstoßende Wechselwirkungskraft nahm mit  $\Lambda$  zu.
- Die beobachtete Tropfen-Tropfen-Wechselwirkung vergrößert die Koagulationszeit um einen Faktor von  $W \sim 10^{65}$  im Vergleich zur schnellen Koagulation von Tropfen, die lediglich bei gegenseitigem Berühren anziehend wechselwirken.
- Mit einem geeigneten Wechselwirkungsmodell wurde die ermittelten hydrodynamischen Radien der Tropfen entsprechend korrigiert. Ohne diese Korrektur konnten die Werte für die Tropfengröße lediglich als Indikator für die Existenz von ME-Tropfen verwendet werden.

- Bei hochkonzentrierten Systemen führt die Kumulanten-Analyse zu einer erheblichen Überschätzung der Polydispersität, da hier eine hohe Korrelation des zweiten Kumulanten und der Basislinie zu erwarten ist.
- Kleine Mengen an PG und DMSO penetrieren in die Oberfläche der dispergierten Tropfen und verhalten sich dabei nahezu wie ein Kotsid.
- Es konnte gezeigt werden, dass Mischungen aus Tensiden mit hoher HLB (Tween 80, Tagat O2) und niedriger HLB (Span 20, Poloxamere) die Stabilität und Löslichkeit der dispergierten Phase erhöhen.
- Bei einer Erhöhung des Tween 80/Span 20-Verhältnisses vergrößern sich die Tropfenradien.
- Verschieden Öle wurden verwendet, wobei sich zeigte, dass die Tropfengröße unabhängig von der Art des verwendeten Öles (mit vergleichbaren Molekülvolumen) ist.
- Das Einbringen eines pharmazeutischen Wirkstoffs in O/W-ME vergrößert die Tropfen. Die hier untersuchten Systeme mit dermatologischer Relevanz waren bis 40°C thermodynamisch stabil.
- ME mit anästhetischen Wirkstoffen (Lidokain, Prilokain) als dispergierte, ölartige Phase wurden charakterisiert.

---

## Suggestions for Future Studies

The following research ideas are possible future projects that are a direct continuation of the work performed in this thesis.

- At high concentration, DLS data can be interpreted in terms of the sum of two independent modes due to interdroplet interaction and polydispersity fluctuation. It has been shown that relative amplitude of the polydispersity fluctuation and interdroplet interaction is the function of solvent refractive index  $n_o$ . The polydispersity and interdroplet interaction of ME should be tried with this theoretical prediction using contrast variation of solvent by mixing to solvent having different refractive index.
- Another sophisticated and technologically very promising area is the formation of inorganic – organic nanoparticles from the suspensions of dispersed materials in the MEs followed by evaporation – polymerization process. The interest in these organic nanoparticles lies in their pharmaceutical application. First, the MEs used to synthesize the nanoparticles are potential systems for drug delivery. Second, the solid organic substances could be injected directly into the vena in the form of nanoparticles. As these substances are often insoluble in water, a classical method of drug delivery using aqueous solutions is not applicable. However, if nanoparticles could be prepared in the the suspension in water, they could be directly injected. The size of the particles is very important, because bigger particles could lead to embolism. However, there are some restrictions in their compositions: the components have to be biocompatible. Toxic solvents and surfactants must be avoided. Synthesis of inorganic – organic nanoparticle should try with ME characterized in this thesis, which have very small droplet size ~ 10 nm and formulated with biocompatible components.
- Several interesting ME formulation problems exist, that remain unsolved. MEs formed with lecithin as a surfactant are of interest, also with pharmaceutical applications. There is still many opportunities for projects on ME stability exist. Additional work on the relationship between interdroplet interaction and temperature for ME droplet stabilized by nonionic and ionic needs to be done to address the differences between these relationships for anionic and nonionic surfactants.

## Appendix A: Collective $D_c$ and Self $D_s$ Diffusion Coefficients

### A.1 Collective Diffusion $D_c$

$D_c$  shown in Eq. (3.36) can be regarded as being driven by the gradient of osmotic pressure associated with the concentration gradient and retarded by solvent and interdroplet friction. Thermodynamic driving force,  $\frac{\partial \Pi}{\partial \mathbf{r}}$  is determined by direct interdroplet interactions and can be described microscopically through the compressibility theorem in terms of the pair distribution function  $g(r)$  of the particles<sup>161</sup>

$$(A.1) \quad \left( \frac{\partial \Pi}{\partial \mathbf{r}} \right)_T = k_B T \left\{ 1 + 4\phi \int dr \, r^2 [g(r) - 1] \right\}^{-1}$$

A microscopic expression can also be given for the collective friction coefficient  $f_c$ <sup>27</sup>

$$(A.2) \quad f_c = k_B T \left\{ \frac{1}{N} \sum_{i=1}^N \sum_{j=1}^N \langle \hat{q} \cdot \bar{D}_{ij}(\bar{r}_k) \cdot \bar{q} \rangle \right\}^{-1}$$

where  $N$  is the (large) number of particles in dispersion,  $\hat{q}$  is a unit vector and the angular brackets  $\langle \dots \rangle$  imply an ensemble average over all possible positions of the particles in the dispersion.  $\bar{D}_{ij}(\bar{r}_k)/k_B T$  is a mobility tensor which connects the drift velocity of particle  $i$  induced through hydrodynamic interactions by a force on particle  $j$  (and vice versa). In the lower concentration limit,  $\phi \rightarrow 0$ ,  $\bar{D}_{ij} \rightarrow D_0 \mathbf{d}_{ij}$ , Eq. (A.1) and (A.2) becomes

$$(A.3) \quad \left( \frac{\partial \Pi}{\partial \mathbf{r}} \right)_T = \phi k_B T \quad \text{and} \quad f_c = 6\phi \eta R_h$$

and substitution of Eq. (A.3) into Eq. (3.36) gives immediately

$$(A.4) \quad \lim_{\phi \rightarrow 0} D_c = D_0$$

as expected.

With the use of Eqs. (A.1) and (A.2), it should be possible, in principle, to calculate the collective diffusion coefficient  $D_c$  given only the form of the potential of mean force  $U(r)$  between the particles. So far as the thermodynamic term [Eq. (A.1)], considerable progress

made in this direction; although  $g(r)$  can not be calculated exactly from  $U(r)$ , many approximate but accurate routes exist, e.g. the Percus-Yevick approximation,<sup>30</sup> HNC approximation, the mean spherical approximation,<sup>57</sup> perturbation approaches and computer simulation.<sup>58</sup> However, for the hydrodynamic friction term  $f_c$  the situation is more complicated because the hydrodynamic interaction between two particles  $i$  and  $j$ , described by  $\bar{D}_{ij}(\vec{r}_k)$ , depends, in the general case, on the positions of many other particles. In relatively dilute dispersion, these effects can be taken into account by expanding thermodynamic term Eq. (A.1) and hydrodynamic term Eq. (A.2) in powers series of volume fraction  $\phi$ .<sup>49,33</sup> So collective diffusion coefficient can be represented as an expansion in powers of volume fraction  $\phi$  as<sup>49,33</sup>

$$(A.5) \quad D_c = D_0 \frac{(1 + K_H \mathbf{f} + \dots)}{(1 - K_I \mathbf{f} + \dots)} \equiv D_0 [1 + \mathbf{a}_1^c \mathbf{f} + \mathbf{a}_2^c \mathbf{f}^2 + \dots]$$

with,

$$(A.6) \quad \mathbf{a}_1^c = K_I + K_H$$

Perturbation coefficients  $K_I$  and  $K_H$  are due to thermodynamic and hydrodynamic effects respectively. Coefficient  $K_I$  is proportional to the well known second osmotic virial coefficient.<sup>162</sup>  $K_H$ , due to hydrodynamic perturbations of the friction factor in the generalized Smoluchowski equation, was evaluated independently by Batchelor<sup>93</sup> and Felderhof<sup>92</sup> and Goldstein and Zimm.<sup>94</sup> These coefficients can be related to the interaction potential of the particles  $U(r)$ . It is convenient to separate explicitly the contributions due to hard sphere repulsion  $U_{hs}$  and from all other possible terms in the pair interaction potential energy  $U(x)$  [ $U_{\text{eff}}(x) = U_{hs}(x) + U(x)$ ], where  $x = (r - 2R_h)/2R_h$  and  $R_h$  and  $r$  are the hydrodynamic radius of particle and the distance between the center of the two particles.

$$K_{I,H} = K_{I,H}^{hs} + \int_0^\infty dx G_{I,H}(x) [1 - g(x)]$$

Where

$$K_I^{hs} = 8$$

$$G_I(x) = 24(1+x)^2$$

$$K_H^{hs} = -6.44$$

(Felderhof)

$$(A.7) \quad G_H(x) = -12(1+x) + \frac{15}{8}(1+x)^{-2} - \frac{27}{64}(1+x)^{-4} - \frac{75}{64}(1+x)^{-5} \quad (\text{Felderhof})$$

$$K_H^{hs} = -6.55$$

(Batchelor)

$$G_H(x) = -11.89(1+x) - 0.706 + 1.69(1+x)^{-1}$$

(Batchelor)

$$K_H^{hs} = -7.16$$

(Goldsrein & Zimm)

$$G_H(x) = -12(1+x) + \frac{15}{8}(1+x)^{-2} - \frac{3}{4}(1+x)^{-4} - \frac{15}{128}(1+x)^{-6} \quad (\text{Goldsrein & Zimm})$$

## A.2 Self diffusion $D_s$

Contrary to collective diffusion, which involves the transport of many particles simultaneously, induced by density gradients, self diffusion is related to the dynamics of a single particle in a system with homogeneous density. The single particle under consideration is commonly referred to as the *tracer particle*, while the remaining Brownian particles are referred to as host particles. The simplest quantity that characterizes the motion of a single Brownian particle is its mean squared displacement, defined as

$$(A.8) \quad \langle \Delta r^2(\mathbf{t}) \rangle = 6D_s(\mathbf{t})\mathbf{t}$$

Self-diffusion coefficient ( $D_s$ ) characterizes the stochastic motion of tracer particles which may be observed in a modern light scattering technique.<sup>27</sup> In light scattering experiments, the incoherent self dynamic structure factor  $F_s(q, \tau)$ , [Eq. (3.34)] which is relevant to the problem of self diffusion can be measured. Interaction of the tracer particle with surrounding Brownian particles clearly affects the time dependence of the mean square displacement. For typical Brownian particles the time scale seen in a light-scattering experiment is far longer than the momentum relaxation time  $\tau_B$ .

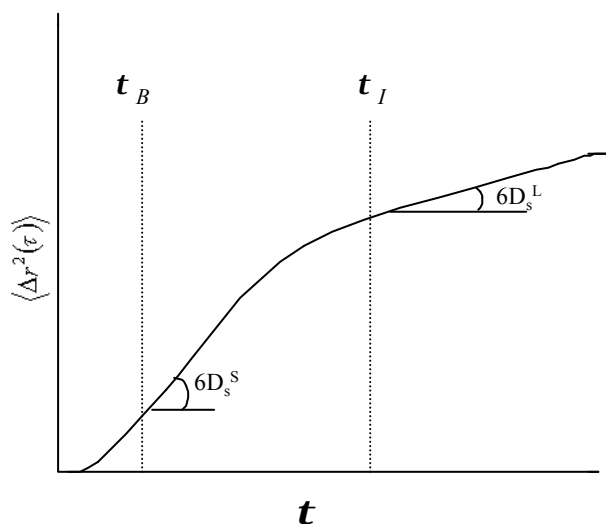


**Figure A.1** The mean square displacement  $\langle \Delta r^2(\mathbf{t}) \rangle$  as a function of time (see text for detail).

For typical Brownian particles the time scale seen in a light-scattering experiment is far longer than the momentum relaxation time  $t_B$ . The latter is of order  $m/\zeta$ , where  $m$  is the mass of a particle. Time scale separation in self diffusion coefficients occur roughly at the time  $t_I$  between particle collision (see Figure A.1).<sup>163</sup> The time scale  $t_I$  is of order  $R^2/D_0$ , where  $R$  is the radius of a particle. The short time self diffusion coefficient  $D_s^S$  and the long – time self diffusion coefficient  $D_s^L$  are defined by the behavior at short and long times<sup>164</sup>

$$(A.9) \quad D_s(\mathbf{t}) \approx \begin{cases} D_s^S & \text{for } \mathbf{t}_B \ll \mathbf{t} \ll \mathbf{t}_I \\ D_s^L & \text{for } \mathbf{t} \gg \mathbf{t}_I \end{cases}$$

where short time  $\mathbf{t}_B \ll \mathbf{t} \ll \mathbf{t}_I$  means times over which relative position of the particles hardly change. Long time  $\mathbf{t} \gg \mathbf{t}_I$  means times over which particle moves, on average, a distance equal to many typical interdroplet spacing. For purely repulsive interaction potentials, one may imagine that the tracer particle is hindered in its motion as time proceeds. For those cases, the long – time self diffusion coefficient is smaller than short-time self diffusion coefficient. The mean square displacement as a function of time thus bends over to attain a smaller slope at long times, this is sketched in Figure A.1. For non-interacting particles there is no difference between long- and short-time self diffusion. Both the long-and short-time self diffusion coefficients are then equal to the free droplet diffusion coefficient  $D_0$ . It should be emphasized that no time scale separation is expected in collective diffusion.<sup>165</sup>

The long-time self-diffusion coefficient is obtained as the product of the thermodynamic driving force  $k_B T$  and the appropriate mobility i.e., inverse of steady state friction coefficient  $1/\zeta_s$  [Eq. (3.37)].

Since the short time self diffusion coefficient describes motion in which the particle positions hardly change, it is given theoretically by a simple ensemble average<sup>166</sup>

$$(A.10) \quad D_s = \langle \hat{q} \cdot D_{ii}(r_k) \cdot \hat{q} \rangle$$

Self diffusion coefficient can be represented as an expansion in powers of volume fraction as  $\phi$ <sup>166</sup>

$$(A.11) \quad D_s = D_0(1 + \alpha_1^s \phi + \alpha_2^s \phi^2 + \dots)$$

where  $\alpha^s$  depends on direct and hydrodynamic pair interaction<sup>121,167</sup>.

First order in volume fraction coefficient  $\alpha_1^s$  for short time self diffusion coefficient  $D_s^S$  is given by

$$(A.12) \quad \alpha_1^s = \mathbf{I}_A = 8 \int_0^\infty g(x) [A_{11} + 2B_{11}] x^2 dx$$

where  $A_{11}$  and  $B_{11}$  are the hydrodynamic interaction functions and can be expressed in terms of the dimensionless distance  $x = \frac{r}{2R_h} - 1$  as<sup>168</sup>

$$(A.13) \quad A_{11}(x) = -\frac{15}{64(1+x)^4} + \frac{13}{256(1+x)^6} + O(x^{-8})$$

$$(A.14) \quad B_{11} = -\frac{17}{1028(1+x)^6} + O(x^{-8})$$

First order in volume fraction coefficient  $\alpha_1^s$  for long time self diffusion coefficient  $D_s^L$  is given by

$$(A.15) \quad \mathbf{a}_1^s = \mathbf{I}_A + \mathbf{a}_s$$

The calculation of the coefficient  $\alpha_s$  requires the solution of the two-body Smoluchowski equation. It has been shown<sup>121</sup> that the coefficient may be expressed as

$$\mathbf{a}_s = \mathbf{a}_s^{HS} + 6Y - 4 \int_1^{\infty} (g-1)(G+2H)x^2 dx,$$

where  $\mathbf{a}_s^{HS} = -0.2657$  is the hard sphere value,  $Y$  is a coefficient related to the electric polarizability in a corresponding dielectric problem, and  $G(x)$  and  $H(x)$  are the hydrodynamic interaction functions.

The ‘‘first order in volume fraction coefficient’’ for the short-time self diffusion coefficient depends on the form of the pair-interaction potential through the pair-distribution function. It is convenient to separate explicitly the contributions due to hard sphere repulsion  $U_{hs}$  and from all other possible terms in the pair interaction potential energy  $U(x)$  [ $U_{eff}(x) = U_{hs}(x) + U(x)$ ]. To the leading order in concentration, the pair-correlation function  $g(x)$  simply the Boltzmann exponential of the pair interaction potential  $U_{eff}(x)$ , that is,

$$(A.16) \quad g(x) = e^{-\frac{U_{eff}(x)}{k_B T}} = e^{-\frac{U_{hs}(x)}{k_B T}} + e^{-\frac{U(x)}{k_B T}} \\ = g_{hs}(x) + g_1(x)$$

$$(A.17) \quad \mathbf{I}_A = 8 \int_0^{\infty} g_{hs}(x)[A_{11} + 2B_{11}]x^2 dx + 8 \int_0^{\infty} g_1(x)[A_{11} + 2B_{11}]x^2 dx$$

The hard sphere value has been calculated as<sup>168</sup>

$$(A.18) \quad \mathbf{I}_A^{HS} = 8 \int_0^{\infty} g_{hs}(x)[A_{11} + 2B_{11}]x^2 dx = -1.8315$$

Thus hard sphere value of coefficient  $\alpha_1^s$  for long time self diffusion coefficient  $D_s^L$  is - 2.0972. Our measurements satisfied so called hydrodynamic regime  $t \gg t_l$  (described in detail in the Section 5.1.3.3), so we measured long time self diffusion coefficient  $D_s^L$ . In result and discussion for simplicity we drop the superscript L.

## Appendix B: Optical and Size Polydispersities

### B.1 Optical Polydispersity

A system of particles identical in terms of size and interactions, but differ in the refractive index; can be characterized by standard deviation in refractive index  $\sigma_o$ . So scattering amplitude

$$(B.1) \quad (\overline{f^2} - \bar{f}^2) \propto (\overline{n^2} - \bar{n}^2)$$

and

$$(B.2) \quad \bar{f} \propto (\bar{n} - n_o)$$

For a system of particles uniform in size and polydisperse in refractive index,  $S^I(\tau)$  we take

$$(B.3) \quad S^I(0) = \frac{(1 - \mathbf{f})^4}{(1 + 2\mathbf{f})^2}$$

the result of the Percus-Yevick approximation for monodisperse hard spheres at volume fraction  $\phi$ .

In Figure 3.3A, we plot the relative amplitude  $\frac{A_2}{A_1 + A_2} = \frac{x}{[x + (1-x)S^I(0)]}$  as a function of volume fraction  $\phi$  for various values of standard deviation for optical polydispersity  $\sigma_o$ .

### B.2 Size Polydispersity

A system of particles polydisperse in size and uniform in refractive index, can be characterized by standard deviation in size  $\sigma_s$  given by

$$(B.4) \quad \mathbf{s}_s^2 = \frac{\langle R^2 \rangle - \langle R \rangle^2}{\langle R \rangle^2}$$

The scattering amplitudes  $f_i \propto R_i^3$

Expression for both  $S^M(0)$  and  $A_1$  have been obtained for polydisperse systems in the Percus-Yevick approximation<sup>43</sup> as

$$(B.5) \quad A_1 = \frac{(1-f)^4}{(1+2f)^2} \left\{ \frac{m_3^2}{\left[ m_6 \left( 1 - \frac{6f(1-f)}{(1+2f)^2} \left[ 1 - \frac{m_2}{m_3} \right] - \frac{9f^2}{(1+2f)^2} \left[ 1 - \frac{m_2^3}{m_3^2} \right] \right) \right]} \right\}$$

$$(B.6) \quad S^M(0) = \frac{(1-f)^4}{(1+2f)^2} \left\{ 1 + \frac{6f(1+2f)}{(1-f)^2} \left[ 1 - \frac{m_4 m_5}{m_3 m_6} \right] - \frac{9f^2}{(1-f)^2} \left[ 1 - \frac{m_4^3}{m_3^2 m_6} \right] \right\}$$

In Figure 3.3B, relative amplitude of slow decay mode as a function of volume fraction  $\phi$  for various values of the standard deviation  $\sigma_s$  is plotted.

### B.3 Combined Optical and Size Polydispersity

Particles are not usually all of the same size and the distribution of scattering powers arises from a distribution in particle size as well as from a distribution in refractive index. For such case, explicit expression for the relative amplitude of the slow mode,<sup>46</sup>

$$(B.7) \quad \frac{A_2}{A_1 + A_2} = 1 - \frac{(1-x)A_1(\mathbf{s}_s, x=0)}{(1-x)S^M(0|\mathbf{s}_s, x=0) + x}$$

In Figure 3.3C, relative amplitude of slow decay mode as a function of volume fraction  $\phi$  for a size polydispersity  $\sigma_s = 0.15$  combined with various values of the standard deviation  $\sigma_b$  is plotted.

### B.4 Particle Size Distribution Functions

It is obvious that the relative mode amplitude calculation requires the pre-assumption of a particle size distribution function, from which the normalized radius moments  $m_u$  can then be derived. As examples we consider two types of particle size distributions, which are positively skewed in particle radius.

#### The logarithmic-normal distribution

Moments for logarithmic-normal (log-normal) distribution is expressed as<sup>43</sup>

$$(B.8) \quad m_u = (1 + \mathbf{s}_s^2)^{u(u-1)/2}$$

#### The Schulz or generalized exponential distribution:

Moments for Schulz distribution is expressed as<sup>43</sup>

$$(B.9) \quad m_u = [1 + (\mathbf{u}-1)\mathbf{s}_s^2][1 + (\mathbf{u}-2)\mathbf{s}_s^2] \dots [1 + \mathbf{s}_s^2]$$

## Appendix C: Change in Energy due to Removal of Water Molecule and Effect of Interaction on Stability of Colloids

### C.1 Change in Energy due to Removal of Water Molecule from Surfactant Layer U<sub>0</sub>

Different contributions to effective interaction are shown in Figure 3.8, where  $R_h$ ,  $R_{hs}$ ,  $R_i$  are the hydrodynamic radius, hard sphere radius and oil core radius, respectively. DLS yields hydrodynamic radius  $R_h$ , which is supposed to consist the oil core and surfactant film containing some solvent molecules too. Length of surfactant film is  $R_h - R_i$ . For all our samples,  $m = \frac{[Oil]}{[Surfactant]}$  molar ratio remains constant ( $1/4$ ) that means

$$(C.1) \quad \frac{R_i^3}{R_h^3 - R_i^3} \approx \frac{1}{4} \Rightarrow \frac{R_h}{R_i} \approx \sqrt[3]{5}$$

A model of penetrable droplet is shown in Figure C.1, where  $2r^*$  is the nearest possible distance between two droplets of radius  $R_h$ . One can get  $r^*$  using assumption of homogeneous dispersion of droplet

$$(C.2) \quad r^* = R_i + \frac{R_h - R_i}{2} = \frac{R_h + R_i}{2}$$

Substituting value of  $R_i$  from Eq.(C.1) to Eq. (C.2). One can get

$$(C.3) \quad r^* = 0.7924R_h$$

If two droplets of radius  $R_h$  are separated by a distance  $r$  ( $r < 2R_h$ ), the volume of overlapping is

$$(C.4) \quad V_{overlapping} = \frac{\pi}{6} (2R_h - r)^2 \left( 2R_h + \frac{r}{2} \right)$$

where,  $r = 2r^*$  in our case.

If we assume that each surfactant molecule tends to arrange itself in such a way that it subtends a constant volume, then the number of surfactant molecules coating each droplet is given by

$$(C.5) \quad n_s = \frac{f_s}{v_s} / n$$

with

$n = \frac{f_i + f_s}{\frac{4}{3}\rho R_h^3}$  is the total number of droplets, where  $\phi_i$  is the volume occupied by oil,  $\phi_s$  is the

volume occupied by surfactant and

$v_s = \frac{M_s}{N_a d_s}$  is the volume of a surfactant molecule, where  $M_s$ ,  $N_a$  and  $d_s$  are the molar mass of surfactant, Avogadro number and density of surfactant, respectively.

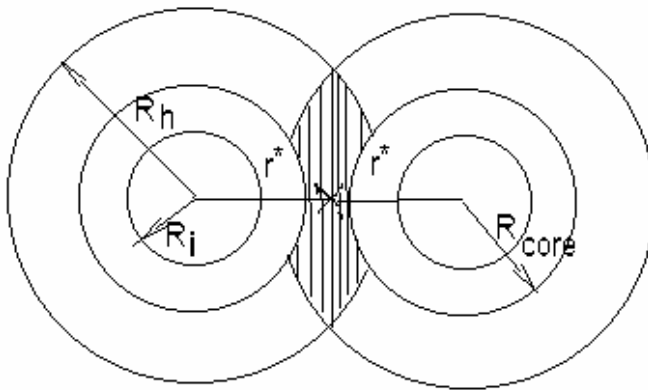


**Figure C.1** Schematic representation of two overlapping droplets. The overlapped volume corresponds to the dashed region. The meaning of the various radii is explained in the text.

The number of water molecules bound per ethylene oxide (EO) group is 2 and the average association energy per water molecule is 22 kJ/mol.<sup>169</sup>

The total number of EO groups associated with each droplet  $n_{EO} = n_s *$  number of EO groups associated with each surfactant molecule.

The total number of water molecules bound to each droplet  $n_w = 2 * n_{EO}$ .

The volume of surfactant shell incorporated in each droplet  $v_l = \frac{4}{3}\rho \{R_h^3 - (r^*)^3\}$

Number of water molecules in overlapping volume  $n_{overlapping} = \frac{n_w * v_{overlapping}}{v_l}$

Change in energy due to removal of water molecules in overlapping region  $U_0$

$$(C.6) \quad U_0 = \frac{22}{N_a} \times n_{overlapping} \text{ kJ}$$

## C.2 Effect of interaction on stability of colloids

The coagulation velocity when  $U_{\text{eff}} = 0$ , i.e., when there is no interaction between the droplets, except a very steep attraction when droplets touch each other is equal to<sup>130</sup>

$$(C.7) \quad G_{U_{\text{eff}}} = 8\rho R D_{\text{app}} n$$

where  $R$ ,  $D_{\text{app}}$  and  $n$  are the droplet radius, diffusion coefficient and total number of droplet per unit volume, respectively.

One can get time of coagulation,<sup>130</sup> when  $U_{\text{eff}} = 0$  from Eq. (3.7) using Stokes-Einstein relation

$$(C.8) \quad t_{f,U_{\text{eff}}=0} = \frac{3\eta}{4kTn}$$

where  $\eta$  is the viscosity of the continuous phase.

The interaction  $U_{\text{eff}}$  diminishes the velocity of coagulation by a factor i.e. the coagulation time increases by a factor,

$$(C.9) \quad W = \int_2^{\infty} \frac{e^{U_{\text{eff}}/kT}}{s^2} ds$$

where droplet completely lost its velocity after traveling over a distance. To get the magnitude of  $U_{\text{eff}}$ ,  $U_{\text{eff}}$  is integrated from  $x_L$  to infinity.

The time of coagulation in presence of interaction potential

$$(C.10) \quad t_f = t_{f,U_{\text{eff}}=0} \times W$$

Colloid may be termed stable when it does not flocculate, say, in a week or a month, which means that time of flocculation should be longer than  $10^6$  sec. Consequently the ratio  $W$  between rapid and slow coagulation will have to surpass  $10^5$  for diluted and  $10^9$  for very concentrated colloids, to give them a reasonable stability.

## Appendix D: Chemical Structure of each constituent used in the formation of MEs

### D.1 Hydrophilic Phase

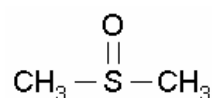


**Figure D.1** DMSO (Dimethyl sulfoxide, MW = 78.1 g/mol)

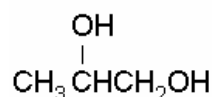


**Figure D.2** PG (Propylene glycol, MW = 76.1 g/mol)



**Figure D.3** Water (MW = 18.02 g/mol)

### D.2 Hydrophobic Phase

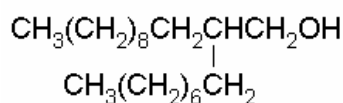


**Figure D.4** Eutanol (2-Octyl-1-dodecanol, MW = 298.6 g/mol)

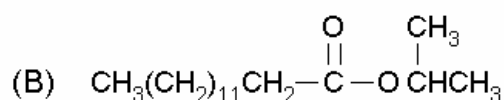
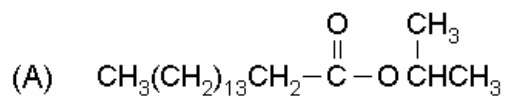


**Figure D.5** (A) IPP (Isopropyl palmitate, MW = 298.5 g/mol) (B) IPM (Isopropyl myristate, MW = 270.5 g/mol)

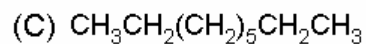
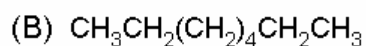
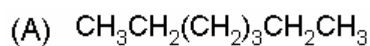


**Figure D.6** (A) *n*-Heptane,  $MW = 100.2 \text{ g/mol}$ , (B) *n*-Octane,  $MW = 114.2 \text{ g/mol}$ , (C) *n*-Nonane,  $MW = 128.3 \text{ g/mol}$ ,

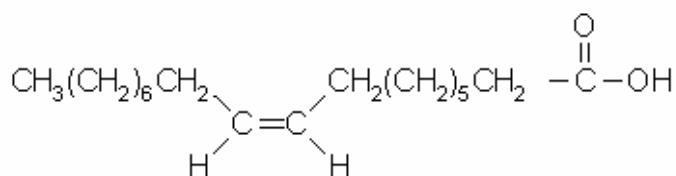


**Figure D.7** OA (*Oleic acid*,  $MW = 282.5 \text{ g/mol}$ )

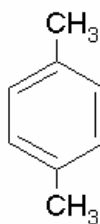


**Figure D.8** *p*-Xylene- (*1,4*-Dimethylbenzene,  $MW = 106.2 \text{ g/mol}$ )

### D.3 Surfactants

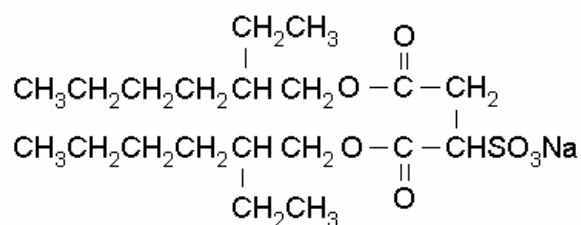
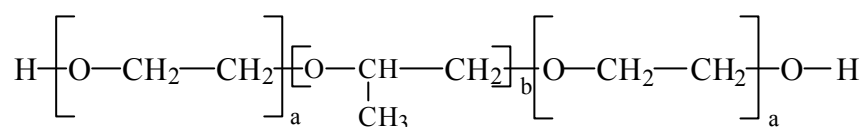


**Figure D.9** AOT (*Sodium bis*(2-ethylhexyl) sulfosuccinate,  $MW \sim 444.6 \text{ g/mol}$ ,  $HLB = n/a$ )



a = 7; b = 54 Poloxamer 331

a = 6; b = 69 Poloxamer 401

**Figure D.10** Poloxamer 331, which also has the name Synperonic<sup>®</sup> PE/L 101, (Polyoxyethylene – Polyoxypropylene – Block copolymer, MW ~3800 g/mol, HLB = 1)

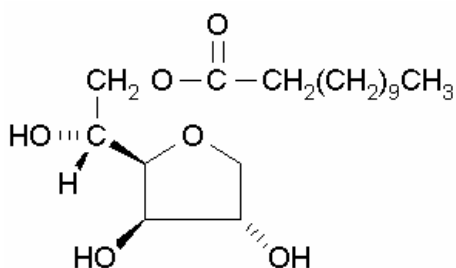


**Figure D.11** Span<sup>®</sup> 20 (Sorbitan monolaurate, MW ~ 346 g/mol, HLB = 8.6)

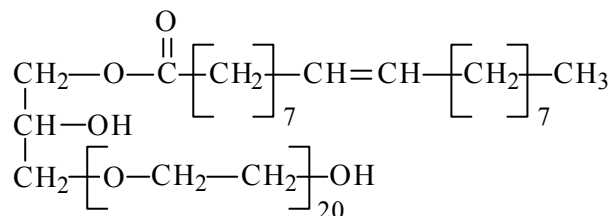


**Figure D.12** Tagat<sup>®</sup> O2 (Polyoxyethylene glycerol monooleate, MW ~1235 g/mol, HLB = 15)

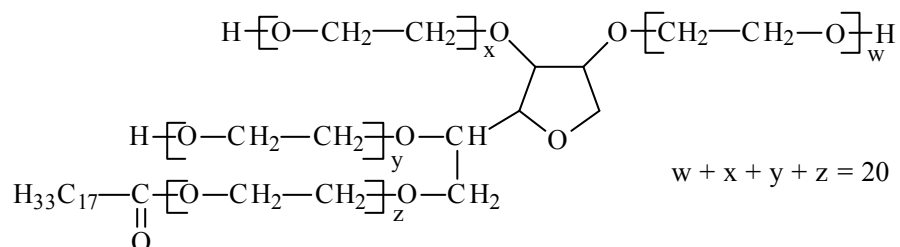


**Figure D.13** Tween<sup>®</sup> 80 (Polyoxyethylene sorbitan mono-oleate, C<sub>64</sub>H<sub>124</sub>O<sub>6</sub>, MW ~ 1309 g/mol, HLB = 15)

## D.4 Drugs

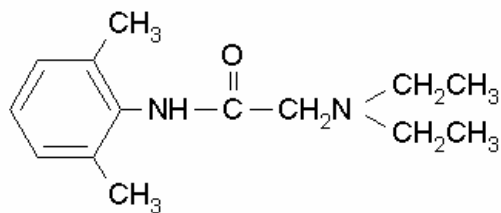


**Figure D.14** Lidocaine (2-diethylamino-N-2,6-dimethylphenyl,  $MG=234.3$  g/mol)

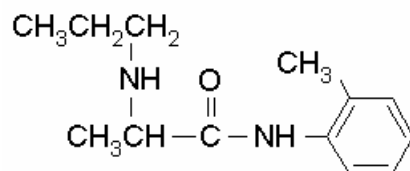


**Figure D.15** Prilocaine (N-2-methylphenyl-2-propylamino,  $MG=220.3$  g/mol)

## References

- 1 Attwood, D.; 1994. In Colloidal Drug Delivery Systems, Kreuter, J.; (Ed.), New York: Marcel Dekker.
- 2 Engström, S.; Lipid Technol. 1990, **2**: 42.
- 3 Shukla, A.; Janich, M.; Jahn, K.; Neubert, R. H. H.; J. Pharm. Sci. 2003, **92**: 730.
- 4 Shukla, A.; Janich, M.; Jahn, K.; Krause, A.; Kiselev, M. A.; Neubert, R. H. H.; Pharms. Res. 2002, **19**: 881.
- 5 Shukla, A.; Jahn, K.; Neubert, R. H. H.; Drugs of the future 2002, **27**: Supp. A, 449.
- 6 Shukla, A.; Annett, K.; Neubert, R. H. H.; J. Pharm. Pharmacology (accepted for publication).
- 7 Shukla, A.; Janich, M.; Jahn, K.; Graener, H.; Neubert, R. H. H.; J. Phys. Chem. (to be Submitted).
- 8 Shukla, A.; Janich, M.; Jahn, K.; Graener, H.; Neubert, R. H. H.; J. Phys. Chem. (to be submitted).
- 9 Hoar, T. P.; Schulman, J. H.; Nature 1943, **152**: 102.
- 10 Mrestani, Y.; El-Mokdad, N.; Rüttinger, H. H.; Neubert, R. H. H.; Electrophoresis 1998, **19**: 2895.
- 11 Mrestani, Y.; Neubert, R. H. H.; J. Pharm. Biomed. Anal. 2001, **24**: 637.
- 12 Johnson, K. A.; Shah, D. O.; J. Colloid Interface Sci. 1985, **107**: 269.
- 13 Osborne, D. W., Ward, A. J. I.; O'Neill, K. J.; 1990. In Drugs and the Pharmaceutical Sciences, Osborne, D. W.; Aman, H.; (Eds.), Vol. 42, New York: Marcel Dekker.
- 14 Nelson, B. K.; Brightwell, W. S.; Khan, A.; Burg, J. R.; Goad, P. T.; Fundam. Appl. Toxicol. 1989, **12**: 469.
- 15 Zecchino, J. R.; Krishnaswamy, N.; Clement, P. A.; Vargas, A.; 1991. Oil-in-Water Emulsions Containing Polyethylene, American Patent US5008100.
- 16 Myers, D.; 1988. Surfactant Science and Technology, Weinheim Germany: VCH Publishers. Inc.
- 17 Danielson, I.; Lindaman, B.; Colloids Surfaces 1981, **3**: 392.
- 18 Israelachvili, J. N.; 1992. Intermolecular & Surface Forces, New York: Academic Press.

- 
- 19 Dörfler, H. D.; 1999. In Handbook of ME Science and Technology, Kumar, P.; Mittal, K. L.; (Eds.), New York: Marcel Dekker, Inc.
  - 20 Entgström S.; Larsson, K.; 1999. In Handbook of ME Science and Technology, Kumar, P.; Mittal, K. L.; (Eds.), New York: Marcel Dekker, Inc.
  - 21 Aikens, P. A.; Friberg, S. E.; 1999. In Handbook of ME Science and Technology, Kumar, P.; Mittal, K. L.; (Eds.), New York: Marcel Dekker, Inc.
  - 22 Malmsten M. 1999.; In Handbook of ME Science and Technology, Kumar, P.; Mittal, K. L.; (Eds.), New York: Marcel Dekker, Inc.
  - 23 Pillai, V.; Kanicky, J. R.; Shah, D. O.; 1999. In Handbook of ME Science and Technology, Kumar, P.; Mittal, K. L.; (Eds.), New York: Marcel Dekker, Inc.
  - 24 Holmberg, K.; 1999. In Handbook of ME Science and Technology, Kumar, P.; Mittal, K. L.; (Eds.), New York: Marcel Dekker, Inc.
  - 25 Cazabat, M. A.; 1985. In Physics of Amphiphiles: Micelles, Vesicles and MEs, Degiorgio, V.; Corti, M.; (Eds.), Amsterdam: North-Holland Physics Publishing.
  - 26 Chen, S. H.; Ann. Rev. Phys. Chem. 1986, **37**: 351.
  - 27 Pusey, P. N.; Tough, R. J. A.; 1985. In Dynamic Light Scattering: Applications of Photon Correlation Spectroscopy, Pecora, R.; (Eds.), New York: Plenum Press.
  - 28 Corti, M.; 1985. In Physics of Amphiphiles: Micelles, Vesicles and MEs, Degiorgio, V.; Corti, M.; (Eds.), Amsterdam: North-Holland Physics Publishing.
  - 29 Guinier, A.; Fournet. G.; 1955. Small Angle Scattering of X-Rays., New York: Wiley, .
  - 30 Percus, J. K.; Yevick. G. J.; Phys. Rev. 1958, **110**: 1.
  - 31 Tanford, C.; 1961. Physical Chemistry of Macromolecules. New York: Academic Press.
  - 32 Rayleigh, L.; 1871. On the Light from the Sky, its Polarisation and Color, Phil. Mag., XLI, 4th series, p. 107.
  - 33 Janich, M.; 1998. Light- and Neutron Scattering Experiments on Bile Salt Micelles. Ph. D. Thesis, Martin-Luther University Halle-Wittenberg, Germany.
  - 34 Berne, B. J.; Pecora, R.; 1976. The Dynamic Light Scattering: With Applications to Chemistry, Biology, and Physics, New York: John Wiley & Sons, Inc.
  - 35 Cazabat, A. M.; Langevin , D.; J. Chem. Phys. 1981, **74**: 3148.
  - 36 Agterof. W. G. M.; van Zomeren, J. A. J.; Vrij, A.; Chem. Phys. Lett. 1976, **43**: 363.

- 
- 37 Gan, L. M.; Ng, S. C.; Ong, S. P.; Chew, C. H.; Koh, L. L.; *Colloid Polym. Sci.* 1989, **267**: 1087.
- 38 Langevin, D.; Rough, J.; 1999. In *Handbook of ME Science and Technology*, Kumar, P.; Mittal, K. L.; (Eds.), New York: Marcel Dekker, Inc.
- 39 Kotlarchyk, M.; Stephens, R. B.; Huang, J. S.; *J. Phys. Chem.* 1988, **92**, 1533.
- 40 Flickinger, G. L.; Dairanieh, I. S.; Zukoski, C. F.; *J. Non-Newtonian Fluid Mech.* 1999, **87**: 283.
- 41 Onsager, L.; *Phys. Rev.* 1931, **37**: 405.
- 42 Weissman, M.; *J. Chem. Phys.* 1980, **72**: 231.
- 43 Pusey, P. N.; Fijnaut, H.M.; Vrij, A.; *J. Chem. Phys.* 1982, **77**: 4270.
- 44 Kirkwood, J. K.; Goldberg, R. J.; *J. Chem. Phys.* 1950, **18**: 54.
- 45 Yan, Y. D.; Clarke, J. H. R.; *J. Chem. Phys.* 1990, **93**: 4501.
- 46 van Veluwen, A.; Lekkerkerker, H. N. W.; de Kruif, C. G.; Vrij, A.; *J. Chem. Phys.* 1988, **89**: 2810.
- 47 Kops-Workhoven, M. M.; Fijnaut, R.; *J. Chem. Phys.* 1982, **77**: 2242.
- 48 Einstein, A.; *Ann. Phys.* 1905, **17**: 549.
- 49 Pusey, P. N.; 1985. In *Physics of Amphiphiles: Micelles, Vesicles and MEs*, Degiorgio, V.; Corti, M.; (Eds.), Amsterdam: North-Holland Physics Publishing.
- 50 Berr, S. S.; Caponetti, E.; Johnson, J. S.; Jones, R. R. M.; Magid, L. J.; *J. Phys. Chem.* 1986, **90**: 5766.
- 51 Kotlarchyk, M.; Chen, S. H.; Husang, J. S.; Kim, M. W.; *Phys. Rev. A* 1984, **29**: 2054.
- 52 Kotlarchyk, M.; Chen, S. H.; *J. Chem. Phys.* 1983, **79**: 2461.
- 53 Hayter, J. B.; 1995. In *Physics of Amphiphiles: Micelles, Vesicles and MEs*, Degiorgio, V.; Corti, M.; (Eds.), Amsterdam: North-Holland Physics Publishing.
- 54 Hansen, J. P.; McDonald, I. R.; 1976. *Theory of Simple Liquids*, London: Academic Press.
- 55 Cannell, D. S.; 1985. In *Physics of Amphiphiles: Micelles, Vesicles and MEs*, Degiorgio, V.; Corti, M.; (Eds.), Amsterdam: North-Holland Physics Publishing.
- 56 Neal, D. G.; Purich, D.; Cannell, D. S.; *J. Chem. Phys.* 1984, **80**: 3469.
- 57 Hayter, J. B.; Penfold, J.; *J. Mol. Phys.* 1981, **42**: 109.

- 
- 58 Gaylor, K.; Snook, I.; Megen, W. V.; J. Chem. Phys. 1981, **75**: 1682.
- 59 Chu, B.; 1990. Laser Light Scattering, New York: Academic Press.
- 60 Schätzel, K.; Appl. Phys. B 1987, **42**: 193.
- 61 Schätzel, K.; Drewel, M.; Stimac, S.; J. Modern Opt. 1988, **35**: 711.
- 62 Schätzel, K.; Peters, R.; Photon Corr. Spectrosc. 1991, **109**: 1430.
- 63 Trachimow, C.; Maeyer, L. De.; Kaatze, U.; J. Phys. Chem. B 1998, **102**: 4483.
- 64 Zimm, B. H. ; J. Chem. Phys. 1948, **16**: 1099.
- 65 Pusey, P. N.; 1977. In Photon Correlation Spectroscopy and Velocimetry, Cummins, H. Z.; Pike, E. R.; (Eds.), New York: Plenum Press.
- 66 Pusey, P. N.; 1977. In Laser Light Scattering in Liquids and Macromolecular Solutions, Degiorgio, V.; Corti, M.; Giglio, M.; (Eds.), New York: Plenum Press.
- 67 Pusey, P. N.; van Megen, W.; Physica A 1989, **157**: 705.
- 68 Gardner, D. C.; Gardner, J. C.; Meinke, W. W.; J. Chem. Phys. 1959, **31**: 978.
- 69 Chu, B.; Gulari, Er.; Gulari, Es.; Phys. Scripta 1979, **19**: 476.
- 70 Vaidya, R. A.; Mettille, M. J.; Hester, R. D.; 1987. In Particle Size Distribution: Assessment and Characterization, Provder, T.; (Ed.), vol. 32, ACS Symp. Ser.
- 71 Ostrowsky, N.; Sornette, D.; Parker, P.; Pike, E. R.; Opt. Acta 1981, **28**: 1059.
- 72 Gulari, Es.; Gulari, Er.; Tsunashima, Y.; Chu, B.; J. Chem. Phys. 1979, **70**: 3965.
- 73 Morrison, I. D.; Grabowski, E. F.; Herb, C. A. A.; Langmuir 1985, **1**: 496.
- 74 Grabowski, E. F.; Morrison, I. D.; 1983. In Measurement of Suspended Particles by Quasi-Elastic Light Scattering, Dahneke, B. E.; (Ed.) New York: Wiley.
- 75 Dalgleish, D. G.; Hallett, F. R.; Food Res. Int. 1995, **28**: 181.
- 76 Provencher, S. W.; Comput. Phys. Commun. 1982, **27**: 229.
- 77 Skilling, J.; Gull, S. F. 1985. In Maximum-Entropy and Bayesian Methods in Inverse Problems, Smith, C. R.; Grandy, W.; (Eds.), Dordrecht: Reidel Press.
- 78 Stock, R. S.; Ray, W. H.; J. Polym. Sci. Polym. Phys. 1985, **23**: 1393.
- 79 Koppel, D. E.; J. Chem. Phys. 1972, **57**: 4814.
- 80 Thomas, J. C.; J. Colloid Interface Sci. 1986, **117**: 187.

- 
- 81 Ostanevich, Yu. M.; *Macromol. Chem. Macromol. Symp.* 1988, **15**: 91.
- 82 Leodidis, E. B.; Hatton, T. A.; 1989. In *Structure and Reactivity of Reverse Micelles*; Pileni, M. P., (Ed.), vol. 65, Amsterdam: Elsevier Science.
- 83 Luisi, P. L.; Magid, L.; *J. CRC Crit. Biochem.* 1986, **20**: 409.
- 84 Christ, S.; Schurtenberger, P.; *J. Phys. Chem.* 1994, **98**: 12708.
- 85 Lossia, S. A.; Flore, S. G.; Nimmala, S.; Li, H.; Schlick, S. J.; *J. Phys. Chem.* 1992, **96**: 6071.
- 86 Nazario, L. M. M.; Hatton, T. A.; Crespo, J.P .S. G.; *Langmuir* 1996,**12**: 6326.
- 87 Gruen, D. W. R.; Haydon, D. A.; *Pure Appl. Chem.* 1980, **52**: 1229.
- 88 Singleterry, C. R.; *J. Amer. Oil. Chem. Soc.* 1955, **32**: 446.
- 89 Tanford, C.; *J. Phys. Chem.* 1972, **76**: 3020.
- 90 Huang, J. S.; Kotlarchyk, M.; Chen, S. H.; 1990. In *Micellar Solutions and MEs: Structure, Dynamics, and Statistical Thermodynamics*, Chen, S. H.; Rajagopalan, R.; (Eds.), New York: Springer.
- 91 Ricka, J.; Borkovec, M.; Hofmeier, U.; *J. Chem. Phys.* 1991, **94**: 8503.
- 92 Felderhof, B. U.; *J. Phys. A: Math. Gen.* 1978, **11**: 929.
- 93 Batchelor, G. K.; *J. Fluid Mech.* 1976, **74**: 1.
- 94 Goldstein, B.; Zimm, B. H.; *J. Chem. Phys.* 1971, **54**: 4408.
- 95 Scriven, L. E.; *Nature* 1978, **263**: 123.
- 96 Lindaman, B; Kamenka, N.; *J. Phys. Chem.* 1980, **84**: 2485.
- 97 D'Aprano, A.; D'Arrigo, G.; Paparelli, A.; Goffredi, M.; Liveri, V. T.; *J. Phys. Chem.* 1993, **97**: 3614.
- 98 Rouch, J.; Safouane, A.; Tartaglia, P.; Chen, S. H.; *J. Chem. Phys.* 1989, **90**: 3756.
- 99 Mays, H.; Ilgenfritz, G.; *J. Chem. Soc., Faraday Trans.* 1996, **92**: 3145.
- 100 Arleth, L.; Pedersen, J. S.; *Phys. Rev. E* 2001, **63**: 061406-1.
- 101 Charlton, I. D.; Doherty, A. P.; *J. Phys. Chem.* 2000, **104**: 8061.
- 102 Visser, A. J. W. G.; Vos, K.; van Hoek, A.; Santema, J. S.; *J. Phys. Chem.* 1988, **92**: 759.

- 
- 103 Eastoe, J.; Robinson, B. H.; Visser, A. J. W. G.; Steytler, D. C.; *J. Chem. Soc., Faraday Trans.* 1991, **87**: 1899.
- 104 Kotlarchyk, M.; Stephens, R. B.; Huang, J. S.; *J. Phys. Chem.* 1988, **92**: 1533.
- 105 Kotlarchyk, M.; Chen, S. H.; Huang, J. S.; *J. Phys. Chem.* 1982, **86**: 3273.
- 106 Nicholson, J. D.; Clarke, J. H. R.; 1984. In *Surfactants in Solution*, Mittal, K.; Lindman, B.; (Eds.), vol 3, New York: Plenum Press.
- 107 Lang, J.; Jada, A.; Malliaris, A.; *J. Phys. Chem.* 1988, **92**: 1946.
- 108 Eriksson, J. C.; Ljunggren, S.; *Prog. Colloid Polym. Sci.* 1990, **81**: 41.
- 109 Eriksson, J. C.; Ljunggren, S.; *Langmuir* 1995, **11**: 1145.
- 110 Gradzielski, M.; Langevin, D.; Farago, B.; *Phys. Rev. E* 1996, **53**: 3900.
- 111 Hellweg, T.; Langevin, D.; *Physica A* 1999, **264**: 370.
- 112 Eastoe, J.; Sharpe, D.; Heenan, R. K.; Egelhaaf, S.; *J. Phys. Chem. B* 1997, **101**: 904.
- 113 Gan, L. M.; Ng, S. C.; Ong, S. P.; Chew, C. H.; Koh, L. L.; *Colloid Polym. Sci.* 1989, **267**: 1087.
- 114 D' Angelo, M.; Fioretto, D.; Onori, G.; Santucci, A.; *J. Mol. Structt.* 1996, **383**: 157.
- 115 Jain, T. K.; Cassin, G.; Badiali, J. P.; Pineni, M. P.; *Langmuir* 1996, **12**: 2408.
- 116 Pusey, P. N.; *J. Phys. A* 1978, **11**: 119.
- 117 Ottewill, R. H.; *Langmuir* 1989, **5**: 4.
- 118 Clarke, H. R.; Nicholson, J. D.; Regan, K. N.; *J. Chem. Soc., Faraday Trans. I* 1985, **81**: 1173.
- 119 Maisano, G.; Mallamace, F.; Micali, N.; *Phys. Rev. A* 1989, **39**: 4103.
- 120 Grenz, U.; Dhont, J. K. J.; Klein, R.; *J. Chem. Phys.* 1987, **87**: 2990.
- 121 Cichocki, B.; Felderhof, B. U.; *Phys. Rev. A* 1990, **42**: 6024.
- 122 Janich, M.; Lange, J.; Graener, H.; Neubert, R.; *J. Phys. Chem.* 1998, **102**: 5957.
- 123 Brunetti, S.; Roux, D.; Bellocq, A. M.; Fourche, G.; Bothorel, P. J. *Phys. Chem.* 1983, **87**: 1028.
- 124 Huang, J. S.; Safran, S. A.; Kim, M. W.; Grest, G. S.; Kotlarchyk, M.; Quirke, N.; *Phys. Rev. Lett.* 1984, **57**: 592.

- 
- 125 Finsy, R.; Devrise, A.; Lekkerkerker, H.; J. Chem. Soc. Faraday Trans. II 1980, **76**: 767.
- 126 Kim, M.W.; Dozier, W. D.; Klein, R.; J. Chem. Phys. 1986, **84**: 5919.
- 127 Huang, J. S.; J. Chem. Phys. 1985, **82**: 480.
- 128 Dozier, W. D.; Kim, M.W.; Klein, R.; J. Chem. Phys. 1987, **87**: 1455.
- 129 Pusey, P. N.; Tough, R. J. A.; Advance Colloid Interface Sci. 1982, 16, 143.
- 130 Verwey, E. J. W.; Overbeek, J. TH. G.; 1948. Theory of the Stability of Lyophobic Colloids, New York: Elsevier Publishing Company, Inc.
- 131 Leaver, M. S.; Olsson, U.; Wennerström, H.; Strey, R.; J. Phys. II, 1994, **4**: 515.
- 132 Leaver, M. S.; Furo, I.; Olsson, U.; Langmuir 1995, **11**: 1524.
- 133 Svergun, D. I.; Konarev, P. V.; Volkov, V. V.; Koch, M. H.; Sager, W. F. C.; Smeets, J.; Blokhuis, E. M.; J. Chem. Phys. 2000, **113**: 1651.
- 134 Heimenz, P. C.; 1986. Principles of Colloid and Surface Chemistry, New York: Marcel Dekker Inc.
- 135 Kahlweit, M.; Strey, R.; Busse, G.; J. Phys. Chem. 1990, **94**: 3881.
- 136 Krause, A.; 2001. Entwicklung und Charakterisierung von Mikroemulsionen zur dermalen Applikation von Arzneistoffen. Ph. D. Thesis, Martin-Luther University Halle-Wittenberg, Germany.
- 137 Jahn K.; 2002. Moderne galenische Zubereitungen zur dermalen Anwendung von Ciclosporin A und Mycophenolatmofetil. Ph. D Thesis, Martin-Luther University Halle-Wittenberg, Germany.
- 138 Reatto L, Tau M. 1985. In Physics of Amphiphiles: Micelles, Vesicles and MEs, Degiorgio, V.; Corti, M.; (Eds.), Amsterdam: North-Holland Physics Publishing.
- 139 Zulauf, M; Rosenbusch, J. P.; J. Phys. Chem. 1983, **87**: 856.
- 140 Hayter, J. B.; Zulaf, M.; Colloid Polym. Sci. 1982, **260**: 1023.
- 141 Kjellander, R.; J. Chem. Soc., Faraday Trans. II 1982, **78**: 2025.
- 142 Dorshow, R.; Briggs, J.; Bunton, C. A.; Nicoli, D. F.; J. Phys. Chem. 1982, **86**: 2388.
- 143 Boltri, L.; Morel, S.; Trotta, M.; Gasco, M. R.; J. Pharm. Belg. 1994, **49**: 315.
- 144 Kriwet, K.; Müller-Goymann, C. C.; Int. J. Pharm. 1995, **125**: 231.

- 
- 145 Trotta, M.; Morel, S.; Gasco, M. R.; *Pharmazie* 1997, **52**: 50.
- 146 Delgado-Charro, M. B.; Iglesias-Vilas, G.; Blanco-Mendez, J.; Lopez-Quintela, M. A.; Guy, R. H.; *Eur. J. Pharm. Biopharm.* 1997, **43**: 37.
- 147 Dreher, F.; Walde, P.; Walther, P.; Wehrli, E.; *J. Control. Release* 1997, **45**: 131.
- 148 Trotta, M.; Gasco, M. R.; Caputto, O.; Sancin, P.; *Pharma. Sci.* 1994, **4**: 150.
- 149 Ritschel, W. A.; *Method Find. Exp. Clin.* 1991, **13**: 205.
- 150 Sarciaux, J. M.; Acar, L.; Sado, P. A.; *Int. J. Phar.* 1995, **120**: 127.
- 151 Warisnoicharoen, W.; Lansley, A. B.; Lawrence, M.; *J. AAPS Pharmsci.* 2000, **2**:1.
- 152 Degiorgio, V.; 1985. In *Physics of Amphiphiles: Micelles, Vesicles and MEs*, Degiorgio, V.; Corti, M.; (Eds.), Amsterdam: North-Holland Physics Publishing.
- 153 Jamal, A. A.; Ph. D. Thesis, In preparation.
- 154 Huibers, P. D. T.; 1996. *Surfactant Self- Assembly, Kinetics and Thermodynamics of Micellar and ME Systems*. Ph. D. Thesis, University of florida, USA.
- 155 Broberg, F.; Evers, H. 1985. *Local Anesthetic Mixture for Topical Application and Method for Obtaining Local Anesthesia.*, American Patent US4529601.
- 156 Brodin, A.; Nyquist-Mayer, A.; Wadsten, T.; Forslund, B.; Broberg, F.; *J. Pharm. Sci.* 1994, **73**: 481.
- 157 Raymond, F.; Nyquist-Mayer, A.; Brodin, A.; Heijl, L.; Scherlund. M.; 2000. *Pharmaceutical Composition with Anaesthetic Effect.*, American Patent US6031007.
- 158 Changez, M.; Varshney, M.; *Drug. Dev. Ind. Pharm.* 2000, **26**: 507.
- 159 Zabka, M.; Benkova, M.; *Pharmacie* 1995, **50**: 703.
- 160 Hellweg, T.; Langevin, D.; *Phys. Rev. E* 1998, **57**: 6825.
- 161 Vrij, A.; Nieuwenhuis, E. A.; Fijnaut, H. M.; Agterof, W. G. M.; *Faraday Discuss. Chem. Soc.* 1978, **65**: 101.
- 162 Hill, T. L.; 1960. *An Introductin to Statistical Thermodynamics*; Reading. MA: Addison-Wesley.
- 163 Pusey, P. N.; *J. Phys. A*, 1975 **8**: 1433.
- 164 Cichocki, B.; Felderhof, B. U.; *Phys. Rev. A* 1990, **42**: 6024.
- 165 Pusey, P. N.; Tough, R. J.; *J. Phys. A* 1982, **15**: 1291.

- 166 Dhont, J. K. G.; 1996. An Introduction to Dynamics of Colloids.; New York: Elsevier Science.
- 167 Cichocki, B.; Felderhof, B. U.; J. Chem. Phys. 1991, **94**: 556.
- 168 Cichocki, B.; Felderhof, B. U.; J. Chem. Phys. 1988, **89**: 1049.
- 169 Hergeth, W. D; Alig, I.; Lange, J.; Lochmann, J. R.; Scherzer, T.; Wartwig, S.; Makromol. Chem. Macromol. Symp. 1991, **52**: 289.

## Acknowledgments

I would like to sincerely thank all people who made the work on this Dissertation possible as well as enjoyable. First of all I express my deep gratitude to Prof. Dr. Heinrich Graener and Prof. Dr. Reinhard Neubert for suggesting the interesting problem and their constant guidance, encouragement and assistance throughout this work. Their expert knowledge, ideas and suggestions were very helpful for me. I benefited a lot from them. Without their permanent guidance and confidence in my work, none of my scientific achievements would have been possible.

I am grateful to Dr. Martin Janich for his patience in unveiling me his vast experience in colloidal Science and for his sharing with me the experimental tricks making everything possible. I am also very grateful to Prof. Dr. Siegfried Wartewig and Dr. Mikhail A. Kiselev for the numerous and fruitful discussions we have had.

I am thankful to Dr. Toraf Patzlaff, Dr. Jens Lange, Dr. Gerhard Seifert, Dr. Y. Mrestani and Mr. Marko Bartel for their helping hands and useful hints.

I will always be deeply indebted to Dr. Poonam Tondan and Prof. Dr. V. D. Gupta for the permanent support they offered to me.

I am also grateful to Dr. Annett Krause, Dr. Konstanze Jahn and Mr. Jamal A. Alkrad from Department of Pharmacy, for preparation of microemulsions of pharmaceutical interest.

I thank all the other colleagues from department of physics and department of pharmacy. They offered me a very nice environment which allowed me to work with high efficiency and great pleasure.

I want to thank my wife, Anjali Shukla for continuous help over these years, for being on my side at the times of special effort in writing this thesis as well as for love and moral support. Special thanks are given to my parents, other family members and Mrs. H. Nigam (Aunti ji) for their love, support and encouragement through the years of my studies. I can not imagine what my life would be without their love. If there is any success of mine, it belongs to them.

I wish to thank all the friends in Halle, German friends, Indian friends and all my friends from the other countries. The financial support from the Deutsche Forschungsgemeinschaft "Graduiertenkolleg 134" is gratefully acknowledged.

# Lebenslauf

## Angaben zur Person

Name: Shukla  
Vornamen: Anuj  
Geburtsdatum: 10.03.1973  
Geburtsort: Sitapur (Indien)  
Nationalität: indisch  
Familienstand: verheiratet  
Adresse: Brandbergweg 23  
Haus B / Zimmer Nr. 507  
06120 Halle/Saale

## Schulischer Bildungsgang

1978 – 1986 Allgemeinbildende Schule  
1986 – 1990 Gymnasium  
1990 Abitur

## Universitärer Bildungsgang

1990 – 1993 Bachelor of Science (B.Sc.) Kurs in Physik, Chemie and  
Mathematik an der Lucknow Universität Indien  
1994 – 1996 Master of Science (M.Sc.) Kurs in Physik an der Lucknow  
Universität Indien  
1996 – 1999 Arbeit im Projekt "Vibrational dynamics of Poly-  
Peptides" bei Prof. V. D. Gupta / Dr. Poonam Tandon.  
Seit 1999 Stipendiat im Rahmen des Graduiertkollegs "Transport von  
Wirkstoffen in biologischen Systemen" an der Martin-Luther-  
Universität Halle-Wittenberg. Promotion in Physik unter  
Betreuung von Prof. H. Graener / Prof. R. H. H. Neubert.

Hiermit erkläre ich, dass die vorliegende Arbeit von mir selbständig und nur unter Verwendung der angegebenen Literaturquellen und Hilfsmittel verfasst wurde. Diese Dissertationsschrift habe ich an keiner anderen Universität oder Hochschule vorgelegt und mich zu keinem früheren Zeitpunkt um den Doktorgrad beworben.

Halle/Saale, den 10.02.2003

---

Anuj Shukla